Proton Resonance Spectroscopy In ^{26}Al

Kara Jayne Keeter

Triangle Universities Nuclear Laboratory
Department of Physics
Duke University
1990

PROTON RESONANCE SPECTROSCOPY IN ^{26}Al

by

Kara Jayne Keeter

Department of Physics

Duke University

Date:_____

Approved:

_____

E. G. Bilpuch, Supervisor

_____

_____

_____

_____

A dissertation submitted in partial fulfillment of the requirements
for the degree of Doctor of Philosophy in the
Department of Physics in the Graduate
School of Duke University

1990

ABSTRACT

(Physics-Nuclear)

PROTON RESONANCE SPECTROSCOPY IN ^{26}Al

by

Kara Jayne Keeter

Department of Physics

Duke University

Date:_____

Approved:

_____

E. G. Bilpuch, Supervisor

_____

_____

_____

_____

An abstract of a dissertation submitted in partial fulfillment of
the requirements for the degree of Doctor of Philosophy
in the Department of Physics in the Graduate
School of Duke University

1990

ABSTRACT

Excitation functions for proton elastic and inelastic scattering on ^{25}Mg were measured with the KN Van de Graaff accelerator and associated high resolution system at Triangle Universities Nuclear Laboratory. Differential cross sections for ^{25}Mg(p,p_0) through (p,p_3) were obtained for the energy range of E_p = 1.94 to 3.43 MeV. The data were measured at laboratory angles θ = 90°, 108°, 135°, 150°, and 165°, with an overall energy resolution of ~400 eV.

Resonance spins, parities, partial widths, and channel spin and orbital angular momentum mixing ratios were extracted with a multilevel, multichannel *R*-matrix based computer program. Resonance parameters were extracted for approximately 64 levels between the excitation energies of 8.23 MeV and 9.61 MeV in the compound nucleus ^{26}Al.

The present results complement our earlier data on states in the compound nucleus ^{26}Al at excitation energies from 6.98 to 8.23 MeV. These previous data were reanalyzed, and several resonance parameter assignments were changed. Results from that reanalysis are presented along with the results of the current measurement. A weak 6^- stretched state was identified at E_p = 1.27 MeV, in agreement with a 6^- $T = 0$ state observed in proton transfer reactions.

The primary motivation for this measurement was to study the proposed $l = 3$, $J^\pi = 6^-$ stretched state at E_x = 9.26 MeV and to determine whether this state is fragmented. The present results confirm the existence of a 6^- state at E_p = 3.08 MeV (E_x = 9.27 MeV). There is no evidence for additional fragmentation of this stretched state.

ACKNOWLEDGMENTS

I would like to thank my advisor, Professor E. G. Bilpuch, for his consistent support throughout my graduate career. Professor G. E. Mitchell has also provided much guidance and advice during my years at TUNL, and has been most helpful in the preparation of this thesis. The combined counsel of these two professors has contributed significantly to my education. In addition, I have profited from the advice of Professors Henry Weller and William Thompson. I owe them a great debt of gratitude for the encouragement and assistance they have extended to me.

Many thanks go to Dr. W. K. Brooks, Dr. J. S. Bull, Dr. D. Fang, Dr. J. F. Shriner, Dr. B. W. Smith, Dr. J. R. Vanhoy, and Dr. B. J. Warthen for helpful discussions and assistance in performing this experiment. I also wish to thank Dr. L. H. James, Dr. J. Li, Dr. P. K. Ramakrishnan, S. Frankle, C. Fowler, C. Frankle, and C. Jackson for their help in various stages of this experiment.

This experiment would not have been possible without the assistance of C. R. Westerfeldt. His dedication to TUNL and his work with the High Resolution Group is highly commendable. His efforts to teach the art of working in parallel to the HiRes students are sincerely appreciated and may not have been entirely in vain. The assistance of S. E. Edwards, R. Rummel, P. Carter, and P. Mulkey in the maintenance of the electronics and accelerator systems is gratefully acknowledged. The excellent work of the machine shop, headed by A. W. Lovette, is appreciated. I also thank Betty Gooch, Doris Albright, and Pam Sneed for their patience and help in navigating the red tape.

There is not room enough here to mention each of the many close friends who have encouraged me over the past six years, but that does not lessen the appreciation I feel for each and every one. Without their support I would have given up long ago. I am especially grateful for the encouragement and motivation of Steve, Kim, and David, and for my mother, who always believes in me even when I doubt myself. This thesis is dedicated to the memory of my father, Albert McKinley Keeter.

This work was supported in part by the United States Department of Energy.

TABLE OF CONTENTS

ABSTRACT iii

ACKNOWLEDGMENTS iv

LIST OF FIGURES viii

LIST OF TABLES xii

I. INTRODUCTION 1

II. THEORY 5

A. Introduction 5
1. Resonance Reactions and Nuclear Spectroscopy 5
2. Compound-Nuclear Resonances 6
3. Wave Theory 10
4. Configuration Space 12
B. *R*-Matrix Theory 13
1. Exterior Region 17
2. Interior Region 19
3. Boundary Condition 22
4. Application to Resonance Analysis 25
C. High Spin States 27
1. Importance of High Spin States 27
2. Current Experimental Status 31
3. Current Experiment 33

III. EXPERIMENTAL EQUIPMENT AND PROCEDURES 34

A. Introduction 34
B. RF Ion Source and Van de Graaff Accelerator 34

C. Energy Feedback System 37
1. Analyzing Magnet 37
2. Electrostatic Analyzer 38
3. Corona Feedback System 39
4. Target Rod Voltage 39
D. Steering Magnets and Focusing Slits 40
E. Scattering Chamber, Detectors, and Target Rod 40
F. Data Acquisition System 43
1. Electronics 43
2. Computer 47
3. Data Acquisition Software 48
G. Targets 48
H. Experimental Resolution 56
I. Experimental Procedure 59

IV. DATA REDUCTION AND RESONANCE ANALYSIS 62

A. Preparation of Data 62
1. Data Handling Programs 62
2. Stripping Procedure 63
B. Offline Analysis of Data 63
1. MULTI6 63
2. Resolution Width Determination 65
3. Energy Calibration 65
C. Fitting Procedure 65
D. Catalog of States and Interference Effects 67
1. Allowed Channels 67
2. Penetrabilities 69
3. Proton Resonance Catalog 69
4. Channel Spin Mixing 91
5. Orbital Angular Momentum Mixing 100
6. Interference Effects 107

V. EXPERIMENTAL RESULTS 108

A. Excitation Functions 108
B. Resonance Parameters for E_p = 0.7 - 2.0 MeV 119
C. Resonance Parameters for E_p = 2.0 - 3.4 MeV 133

VI. ANALYSIS OF RESULTS 143

A. Comparison With Previous Results 143
B. Spectroscopic Factors 152
C. Resonance Strengths 154
D. Conclusions 161

VII. SUMMARY 169

BIBLIOGRAPHY 171

BIOGRAPHY 176

LIST OF FIGURES

2.1 Allowed Channels for Proton-Induced Reactions for the Compound Nucleus ^{26}Al..... 9

2.2 Angular Momentum Coupling Scheme in the Channel Spin Representation..... 15

2.3 A Description of Stretched States in Both the *j-j* and the *L-S* Coupling Schemes..... 30

3.1 Schematic of the High Resolution KN Van de Graaff Single-Ended Horizontal Accelerator, Beam Line, and Energy Feedback System..... 36

3.2 Top View of the Charged Particle Scattering Chamber and Detector Setup..... 42

3.3 Block Diagram of the Data Acquisition System used with the High Resolution Laboratory Van de Graaff Accelerator and VAX 11/750 Computer..... 45

3.4 Diagram of the Bell Jar and Evaporation Deposition Setup used to Produce Thin-Film Carbon-Backed Magnesium Targets..... 51

3.5 Typical Charged Particle Spectrum from the 165° Detector..... 58

4.1 Coulomb Penetrabilities versus Energy for the ^{25}Mg(p,p_0) and ^{25}Mg(p,p_1) Reactions..... 71

4.2 Coulomb Penetrabilities versus Energy for the ^{25}Mg(p,p_2) and ^{25}Mg(p,p_3) Reactions..... 73

4.3 Variation in Resonance Shape as a Function of Detector Angle and Orbital Angular Momentum Value 75

4.4 Variation in Resonance Shape as a Function of Detector Angle and Orbital Angular Momentum Value 77

4.5 Variation in s-wave Resonance Shape as a Function of J for $J^{\pi} = 2^{+}, 3^{+}$ at Five Angles 79

4.6 Variation in s-wave Resonance Shape as a Function of J for $J^{\pi} = 2^{+}, 3^{+}$ at 90° and 165° 81

4.7 Variation in p-wave Resonance Shape as a Function of J for $s = 3$, $J^{\pi} = 2^{-}, 3^{-}$ and 4^{-} at Five Angles 84

4.8 Variation in p-wave Resonance Shape as a Function of J for $s = 3$, $J^{\pi} = 2^{-}, 3^{-}$ and 4^{-} at 90° and 165° 86

4.9 Variation in d-wave Resonance Shape as a Function of J for $s = 3$, $J^{\pi} = 1^{+}, 2^{+}, 3^{+}, 4^{+}$ and 5^{+} at Five Angles 88

4.10 Variation in d-wave Resonance Shape as a Function of J for $s = 3$, $J^{\pi} = 1^{+}, 2^{+}, 3^{+}, 4^{+}$ and 5^{+} at 90° and 165° 90

4.11 Variation of Resonance Shape with Channel Spin Admixture for a $J^{\pi} = 2^{-}$ p-wave Resonance at Five Angles 93

4.12 Variation of Resonance Shape with Channel Spin Admixture for a $J^{\pi} = 2^{-}$ p-wave Resonance at 90° and 165° 94

4.13 Variation of Resonance Shape with Channel Spin Admixture for a $J^{\pi} = 3^{+}$ d-wave Resonance at Five Angles 97

4.14 Variation of Resonance Shape with Channel Spin Admixture for $J^{\pi} = 3^{+}$ d-wave Resonance at 90° and 165° 99

4.15 Variation of Resonance Shape with Orbital Angular Momentum Admixture for $J^{\pi} = 3^{+}$, $s = 2$ at Five Angles..... 102

4.16 Variation of Resonance Shape with Orbital Angular Momentum Admixture for $J^{\pi} = 3^{+}$, $s = 3$ at 90° and 165°..... 104

4.17 Variation of Resonance Shape with Orbital Angular Momentum Admixture for $J^{\pi} = 3^{-}$, $s = 2$ at Five Angles..... 106

5.1 Differential Cross Sections for the $^{25}Mg(p,p_0)^{25}$ Reaction at 165°, 135°, 108° and 90° from E_p = 1.946 to 3.000 MeV..... 110

5.2 Differential Cross Sections for the $^{25}Mg(p,p_0)^{25}$ Reaction at 165°, 135°, 108° and 90° from E_p = 2.00 to 2.33 MeV..... 112

5.3 Differential Cross Sections for the $^{25}Mg(p,p_0)^{25}$ Reaction at 165°, 135°, 108° and 90° from E_p = 2.33 to 2.67 MeV..... 114

5.4 Differential Cross Sections for the $^{25}Mg(p,p_0)^{25}$ Reaction at 165°, 135°, 108° and 90° from E_p = 2.67 to 3.00 MeV..... 116

5.5 Differential Cross Sections for the $^{25}Mg(p,p_0)^{25}$ Reaction at 165°, 135°, 108° and 90° from E_p = 3.00 to 3.43 MeV..... 118

5.6 Differential Cross Sections for the $^{25}Mg(p,p_0)^{25}$ Reaction at 165°, 135°, 108° and 90° from E_p = 0.70 to 2.00 MeV..... 126

5.7 Differential Cross Sections for the $^{25}Mg(p,p_0)^{25}$ Reaction at 165°, 135°, 108° and 90° from E_p = 0.70 to 1.13 MeV..... 128

5.8 Differential Cross Sections for the $^{25}Mg(p,p_0)^{25}$ Reaction at 165°, 135°, 108° and 90° from E_p = 1.13 to 1.57 MeV..... 130

5.9 Differential Cross Sections for the $^{25}Mg(p,p_0)^{25}$ Reaction at 165°, 135°, 108° and 90° from E_p = 1.57 to 2.00 MeV..... 132

6.1 Differential Cross Sections for the $^{25}Mg(p,p_0)^{25}$ Reaction at 165° from E_p = 1.21 to 1.33 MeV 145

6.2 A Comparison of Fits with Varying Spins and Widths for the State at E_p = 1.273 MeV 147

6.3 Differential Cross Sections for the $^{25}Mg(p,p_0)^{25}$ Reaction at 165° and 90° from E_p = 3.05 to 3.15 MeV 151

6.4 Proton Reduced Widths versus Energy for $J^\pi = 2^-$ p-wave Resonances, 2^+ s-wave Resonances, and 2^+ d-wave Resonances 156

6.5 Proton Reduced Widths versus Energy for $J^\pi = 3^-$ p-wave Resonances, 3^+ s-wave Resonances, and 3^+ d-wave Resonances 158

6.6 Proton Reduced Widths versus Energy for $J^\pi = 4^-$ p-wave Resonances, 4^+ d-wave Resonances, and 6^- f-wave Resonances 160

6.7 Porter-Thomas Distributions for $J^\pi = 1^-$ p-wave Resonances, 1^+ d-wave Resonances, and 2^- p-wave Resonances 163

6.8 Porter-Thomas Distributions for $J^\pi = 2^+$ s-wave Resonances, 3^- p-wave Resonances, and 3^+ s-wave Resonances 165

6.9 Porter-Thomas Distributions for $J^\pi = 3^+$ d-wave Resonances, 4^- p-wave Resonances, and 4^+ d-wave Resonances 167

LIST OF TABLES

4.1 Allowed Entrance and Exit Channels for Resonances in ^{26}Al..... 68

5.1 The ^{25}Mg(p,p$_0$)^{25} Resonance Parameters for E_p = 0.7 - 2.0 MeV... 120

5.2 The ^{25}Mg(p,p$_0$)^{25} Resonance Parameters for E_p = 2.0 - 3.4 MeV.. 134

5.3 The ^{25}Mg(p,p$_1$)^{25} Resonance Parameters for E_p = 0.7 - 3.4 MeV... 140

5.4 The ^{25}Mg(p,p$_2$)^{25} Resonance Parameters for E_p = 0.7 - 3.4 MeV... 141

6.1 Comparison of Present Resonance Parameters with Previous Results for E_p = 0.7 - 2.0 MeV..... 149

6.2 Comparison of Spectroscopic Factprs for Stretched States in the Region E_p = 2.0 - 3.4 MeV..... 153

PROTON RESONANCE SPECTROSCOPY IN ^{26}Al

CHAPTER I

INTRODUCTION

Nuclear physics describes matter at a level deeper than that of the electronic structure of atoms, molecules, and solids, but stops short of describing the internal structure of protons and neutrons. The study of nuclear physics originated with experiments in 1896 by Becquerel and in 1911 by Rutherford. In 1920 the existence of the neutron was first proposed by Rutherford. Chadwick confirmed the existence of the neutron in 1932 by interpreting experiments of Curie-Joliot and Joliot and verifying them with his own experiments. Nuclear reactions have since been used to study both nuclear forces and nuclear structure.

Cockcroft and Walton measured the first nuclear reaction that utilized accelerated protons in 1932. Since then, much of our knowledge of nuclear structure and reactions has been established by accelerator experiments. For general nuclear structure research at low energies, the most versatile accelerator remains the electrostatic generator developed by Van de Graaff in 1931.

From early reaction studies it was known that compound nuclei are most likely to be formed when the incident particle has certain energies. At such energies the system is said to be in resonance. The study of the energies, spins, parities, and other static properties of these resonances is a part of nuclear spectroscopy. This area has been an important subfield of nuclear physics since the observation of neutron resonances first led to the compound nuclear theory. In the 1960's, experimental interest shifted from neutron studies to charged particle reactions. The local emphasis

was investigation of the fine structure of isobaric analog resonances.

The High Resolution Group at Triangle Universities Nuclear Laboratory (TUNL) has specialized in low energy nuclear spectroscopy experiments utilizing the KN Van de Graaff accelerator and associated high resolution feedback system. The energy resolution afforded by the feedback system has enabled this laboratory to play a leading role in proton resonance spectroscopy. Early studies provided the first measurement of the fine structure of isobaric analog resonances (Keyworth, 1968; Bilpuch, 1976). More recently, experiments have emphasized statistical properties of the resonances.

The properties of the resonances depend on the detailed characteristics of the compound nucleus. The energy distributions of these resonances and various other properties have been used to examine statistical assumptions about the compound nucleus. Most recently, the High Resolution Laboratory has conducted an extensive series of measurements to verify the Porter-Thomas distribution.

Early work involved even-even target nuclei exclusively. In recent years odd-mass target nuclei in the 2s-1d shell have been investigated. Earlier measurements in this series include ^{29}Si (ground state $J^{\pi}=1/2^{+}$), ^{27}Al ($5/2^{+}$), ^{23}Na ($3/2^{+}$), ^{39}K ($3/2^{+}$), ^{35}Cl ($3/2^{+}$), and ^{31}P ($1/2^{+}$). The resonance analysis for these targets is much more complicated than for zero-spin targets, because of the possibility of channel spin mixing and orbital angular momentum mixing in both the entrance and the exit channels. In the present experiment, ^{26}Al is studied by proton scattering from the target nucleus ^{25}Mg ($5/2^{+}$). This is only the second target in this series of measurements with such a large ground state spin. In addition, the existence of several low-energy states in ^{25}Mg enable several inelastic scattering channels to be energetically allowed. This experiment thus has more open channels than previous

experiments in this series. Complicating the analysis even further is the lack of an open (p,α) channel, which is often useful in ruling out unnatural parity states. Differential cross sections were obtained for the region E_p = 1.94 to 3.43 MeV and resonance parameters were extracted. These data and parameters are presented in this dissertation. A total of 64 resonances were found in this region, of which nearly all were previously unobserved. In addition, data from an earlier experiment measuring energy levels in ^{26}Al below E_p = 2.0 MeV were re-examined, and an updated set of resonance parameters for this region is reported herein.

Spectroscopic information on ^{26}Al obtained via several reactions is available in the literature. In particular, the reactions ^{25}Mg(p,γ)^{26}Al and ^{25}Mg(p,p′)^{25}Mg have been used to study resonances in the E_p = 0.31 - 1.84 MeV region (Endt *et al.*, 1986; Endt *et al.*, 1988a). Shell model calculations for spins, parities, and isospins of levels in ^{26}Al are also reported by Endt *et al.* (1988b). The resonance parameters obtained in the present study of ^{26}Al are compared with the results of these other studies.

The information obtained from this experiment is useful for studies of stretched states in addition to comparisons with nuclear structure calculations. A stretched state is simplistically defined as a state in which the spins of the target nucleus and the projectile and their relative orbital angular momentum are aligned, so that the total spin has the maximum value possible. The $J^\pi = 6^-$ stretched state in ^{26}Al can be understood as a simple particle-hole shell model state of $(f_{7/2}d_{5/1}^{-1})$. These states have been studied by Peterson *et al.* (1988a, 1988b) using various probes. Stretched states in the isobaric analog nucleus ^{26}Mg have also been studied by electron scattering (Clausen *et al.*, 1988) and pion scattering (Clausen *et al.*, 1990). These measurements were used to extract information about the nuclear interaction (Lindgren, 1984). One motivation for the present experiment is to corroborate these studies.

In this dissertation, a brief outline of the relevant theory is given in Chapter II. The main part of this chapter describes *R*-matrix theory, which is used to extract resonance parameters from the data. A brief discussion of the importance of stretched states to the study of nuclear interactions is also included in this chapter, along with a discussion of the importance of the current experiment to the investigation of stretched states in ^{26}Al. The experimental and data acquisition systems of the High Resolution Laboratory are described in Chapter III. This chapter also describes the process of producing quality thin-film ^{25}Mg targets. The details of the preliminary data preparation and analysis are presented in Chapter IV. Chapter V presents tables of the resonance parameters and plots of the data and fits. A comparison of these results with those of previous experiments and with the Porter-Thomas distribution is contained in Chapter VI. A brief summary is given in Chapter VII.

CHAPTER II

THEORY

A. Introduction

1. Resonance Reactions and Nuclear Spectroscopy

Detailed theories to explain resonance phenomena and other nuclear reactions have been patterned after two apparently contradictory models of nuclear structure. In single-particle theories based on the shell model (Bethe, 1940; Fernbach, Serber and Taylor, 1949; Feshback, Porter and Weisskopf, 1954) it is assumed that the shell-model potential can be used to describe the interaction of the incident nucleon and the target nucleus. In this case, processes called direct reactions occur which have lifetimes comparable to the time it would take the incident nucleon to traverse the target nucleus. Single-particle theories treat the reaction as a single nucleon interacting with some mean field which results from the interactions of all of the nucleons in the nucleus, plus an interaction which connects the initial and final states.

In the liquid-drop model (Bohr, 1936), it is assumed that a nuclear projectile incident on a nucleus interacts strongly with all the nucleons in the nucleus and quickly shares its energy with them. The projectile and target nucleus are said to have formed a "compound nucleus". Relative to direct processes, the intermediate state of the compound nucleus is rather long-lived (on the order of 10^{-15} s, as opposed to 10^{-21} s for direct reactions). Compound-nuclear reactions are the most common types of

reactions at low incident beam energies, while direct reactions dominate the cross sections at higher beam energies. This discussion will be limited to treatments of compound-nuclear reactions. Specifically, one approach will be developed, called the *R*-matrix approach.

2. Compound-Nuclear Resonances

After formation, the compound nucleus is in an excited state. The compound nucleus then "forgets" how it is formed, and decays in a manner independent of its means of formation; in other words, the exit channel of the compound nucleus depends only on the energy, angular momentum, and parity of the compound nucleus, and not on the specific entrance channel. Each of the many ways in which the compound nuclear state may be produced or may decay is called a channel. For example, a compound nucleus in an excited state, represented by C^*, may be formed by the capture of a bombarding particle, represented by a, on a suitable initial target nucleus, represented by X. This reaction is expressed as:

$$X + a \rightarrow C^*$$

and would correspond to the entrance channel α_a. The lifetime of the compound state is $\tau \sim \hbar/\Gamma$ where Γ is the width of the resonance. The compound nucleus can then decay in a number of different ways, such as the emission of a photon or nucleon, represented by b. The process is then expressed as:

$$C^* \rightarrow C + b$$

and corresponds to the exit channel α_b. This dissertation is concerned with the compound nucleus ^{26}Al, formed via the entrance channel (p + ^{25}Mg). A schematic representation of the entrance and exit channels is given in figure 2.1. Since the

compound nucleus has such a long lifetime, the resonances are very narrow and the states can be thought of as almost stable. The states can therefore be expressed as a linear combination of standing waves. A resonant nuclear state is characterized by a rapid change in the cross section as a function of energy. The cross section for this process is:

$$\sigma_{ab} = \frac{\pi \lambda\!\!\!^{-2} g \Gamma_a \Gamma_b}{\left[(T - T_0)^2 + \frac{\Gamma^2}{4} \right]} \qquad (2.1)$$

where $\lambda\!\!\!^{-}$ is the center-of-mass wavelength of the bombarding particle a, T is the center-of-mass energy, T_0 is the center-of-mass energy at which there is a resonance with the level E_i, and g is a statistical factor of the order unity which depends on the intrinsic spins. This is known as the Breit-Wigner resonance formula. This formula corresponds to the case for which only one orbital angular momentum value contributes to the reaction. It is valid for all channels except the elastic channel, for which the interference with diffractive and reflective scattering must be considered. The spin factor g is given by:

$$g(J) = \frac{2J+1}{(2I_1+1)(2I_2+1)} \qquad (2.2)$$

where J is the total angular momentum of the compound state, and I_1 and I_2 are the spins of the projectile and the target. The "level widths" Γ_a and Γ_b refer to the probability of decay via the α_a and α_b channels. The total width Γ of the resonance is the sum of partial widths for all possible decay modes:

$$\Gamma = \Gamma_{elastic\ scattering} + \Gamma_{inelastic\ scattering} + \Gamma_{\alpha\text{-}particle} + \ldots + \Gamma_{\gamma} \quad . \qquad (2.3)$$

Figure 2.1 Allowed channels for proton-induced reactions for the compound nucleus ^{26}Al. The incident proton strikes the target nucleus ^{25}Mg, and forms the compound nucleus ^{26}Al in an excited state (E_x, J^π). The compound nucleus then decays to an energetically allowed state ($E_f < E_x$) in the nucleus ^{25}Mg by emitting a proton. All other particle-decay channels, such as α-emission, are closed.

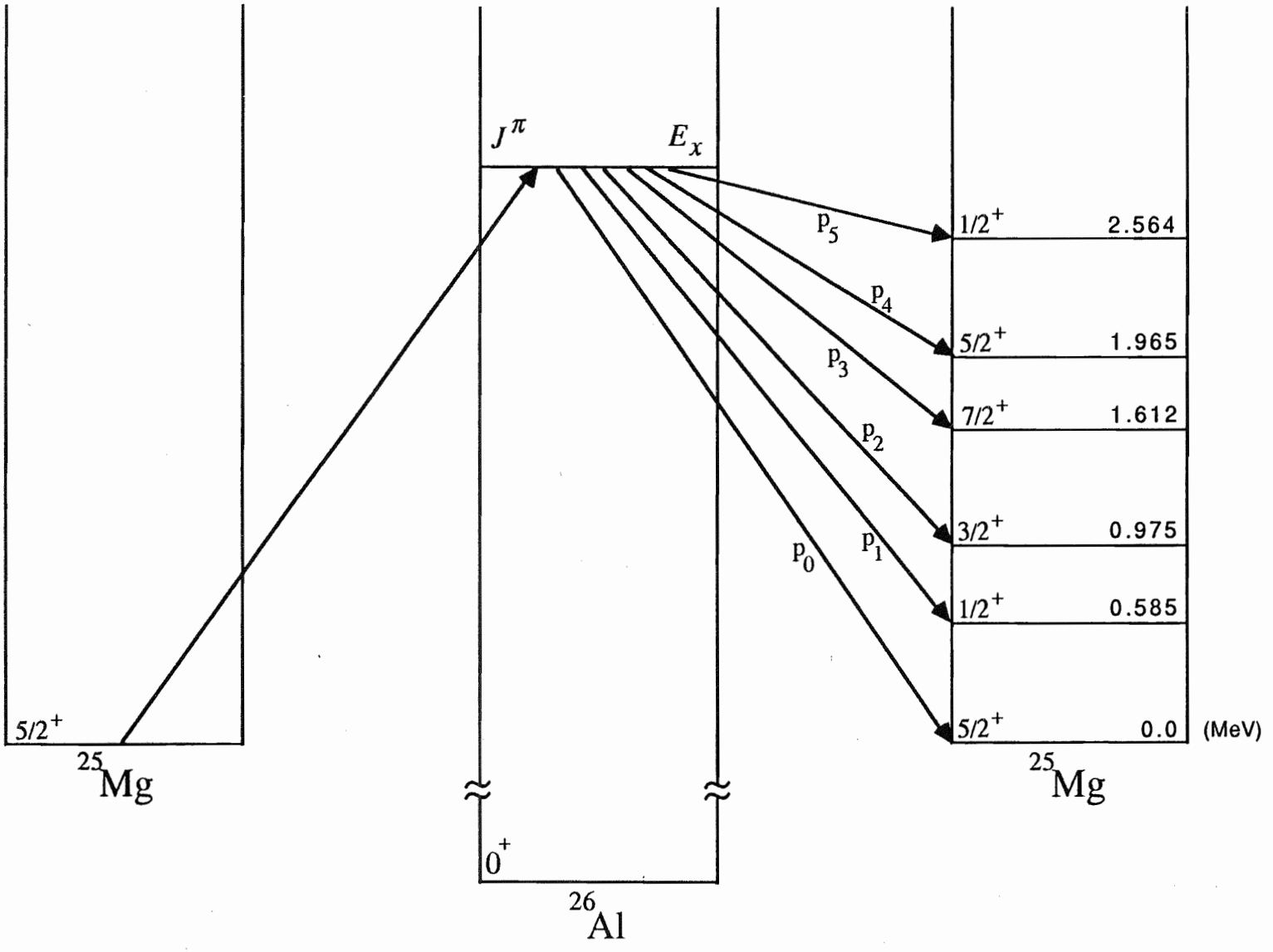
J^π
E_x
p_5
p_4
p_3
p_2
p_1
p_0
1/2+ 2.564
5/2+ 1.965
7/2+ 1.612
3/2+ 0.975
1/2+ 0.585
5/2+ 0.0 (MeV)
5/2+
25Mg
0+
26Al
25Mg

A large number of reaction theories have been developed to describe compound-nuclear resonances. In general, the theories fall into three classes: (1) those which define the resonances of the compound nucleus by means of imposed boundary conditions at the radius of each channel; (2) those which use a modified Hamiltonian and projection operators to produce the resonances and avoid the use of channel radii; (3) those based on analytical properties of the scattering matrix. Each of these approaches has its own particular advantages.

3. Wave Theory

Before examining more closely the specific theory which we adopt, some general aspects of the formalism should be considered. Wave theory provides a convenient description of collisions in nuclear physics which emphasizes the role of conserved angular momentum. When scattering is due to a localized spherically symmetric potential with a radius of the same order of magnitude as the de Broglie wavelength of the incident particle, the partial-wave formalism is especially suitable. This formalism describes the scattering in terms of phase shifts which can be determined from experimental differential cross sections. The solution of the Schrödinger equation is then given by an initial in-bound asymptotically plane wave and an asymptotic final state which is a superposition of spherical waves. If the interaction potential involves only a central force the solutions are eigenfunctions of the angular momentum operator and describe particles with definite L^2 and L_z with the target as origin and a selected quantization axis z. At a potential boundary, there may be a change in amplitude phase. If only a change in phase occurs, then elastic scattering occurs; if the amplitude of the wave changes, the process is nonelastic

scattering. The partial-wave method is generally useful in sorting out complex situations in which overlapping resonances are present, and measurements of both elastic and nonelastic (or total) cross sections as a function of energy are necessary.

For the case of a single open spinless channel, the partial-wave decomposition of the scattering amplitude is well known:

$$f(\theta)=\frac{1}{k}\sum_{l=0}^{\infty}(2l+1)e^{i\delta_l}\sin\delta_l\ P_l(\cos\theta) \tag{2.4}$$

where θ is the scattering angle, k is the wave number, l is the angular momentum in the partial-wave decomposition, δ_l is the phase shift for the partial wave l and is energy-dependent, and $P_l(\cos\theta)$ is the Legendre polynomial. The differential cross section for scattering into the solid angle element $d\Omega$ is then simply:

$$\frac{d\sigma}{d\Omega}=|f(\theta)|^2. \tag{2.5}$$

The partial-wave expansion of an incident plane wave in a Coulomb field will prove useful. This is given by Schiff (1949) as:

$$\Psi_{\alpha sv}^{\text{inc}} = \frac{1}{\sqrt{v_\alpha}}\psi_{\alpha sv}\left[\left(1-\frac{\eta_\alpha^2}{ik_\alpha(r_\alpha-z_\alpha)}\right)\exp i\left(k_\alpha z_\alpha-\eta_\alpha\ln k_\alpha(r_\alpha-z_\alpha)-\sigma_{\alpha 0}\right)\right.$$

$$\left.-\frac{\sqrt{\pi}}{r_\alpha k_\alpha}\ C_\alpha(\theta_\alpha)\ \exp i(\rho_\alpha-\eta_\alpha\ln 2\rho_\alpha+\sigma_{\alpha 0})\right] \tag{2.6}$$

Our goal is to derive an expression for the cross section in terms of parameters of the resonant compound-nuclear states. The first thing we will do is define a "configuration space" in which the "internal region" represents that part of space where the nuclear force affects the nucleons, and the "external region" is where only

non-nuclear forces affect the nucleons. Schrödinger's equation will then be formed for the interior and exterior regions, and wave functions which satisfy Schrödinger's equations will be obtained. These wave functions will be expressed in convenient forms and appropriate boundary conditions applied. Finally, an expression for the cross section will be obtained.

4. Configuration Space

In order to describe resonance reactions, it is useful to employ a configuration-space view of the different entrance and exit channels of the compound state. In this view, space is divided into an "internal" region and an "external" region. Because of the short range of nuclear forces, the compound nucleus occupies a small volume V in the configuration space of all the nucleons. The dimension of the configuration space is $3A$, where A is the number of the nucleons. The volume V is chosen to be that part of the space in which all of the nucleons are close enough together to interact via the strong nuclear force. Whenever a group of nucleons is separated from the other nucleons by a distance larger than the range of the nuclear force, the groups are considered to move under the influence of the electromagnetic interaction of the groups. The various possible modes of decay or formation of a compound state are called channels. All channels are regions in configuration space projecting from the volume V which encloses the compound nucleus.

For low-energy nuclear reactions, multi-body breakup usually is not energetically allowed. Even when it is allowed, the process may be described in terms of successive two-body breakups. Therefore, the following treatment is restricted to two-body breakup. The decay by emission of a gamma ray is not properly defined as a

channel, but this process can be accommodated by the resonance theory. The word channel is usually defined to mean a pair of reaction products, their states of excitation, their relative orbital angular momentum, and their "channel spin" s, defined as the sum of the spins of the two reaction products. A given channel is described by a constant a_c called the channel radius, which can be thought of classically as the sum of the radii of the two reaction products:

$$a_c = r_0\left(A_1^{1/3} + A_2^{1/3}\right). \tag{2.7}$$

Then the specific nuclear interactions dominate in the internal region, and only the well-known interactions, such as Coulomb forces, occur in the external regions. A channel c is specified by the quantum numbers $c=\{\alpha, s, l, J, M\}$ where α represents the particle pair, for example (p + ^{25}Mg), and $\{s, l, J, M\}$ are quantum numbers in the channel-spin notation (see figure 2.2).

B. R-Matrix Theory

A reaction theory which is based on the analytical properties of the scattering matrix is the Wigner-Eisenbud theory. It is widely used in the analysis of reaction data, and has recently been applied to the quark bag model (Jaffe, 1979; Lomon, 1983). In this theory, the compound states exist in the configuration space of the compound nucleus. Since the solution of the Schrödinger equation for the nucleus is extremely complicated, this theory does not attempt to obtain exact expressions for the nuclear wave functions. Instead, where sharp resonances occur, the wave function is dominated by one or a few of the stationary states. This drastically decreases the number of parameters needed to describe the cross section in the vicinity of resonances.

Figure 2.2 Angular momentum coupling scheme in the channel spin representation. The particle pair, e.g. target nucleus and projectile, has a relative orbital angular momentum $\boldsymbol{l}$. The channel spin $\boldsymbol{s}$ (or $\boldsymbol{s}'$) is formed by coupling the spins of the target (or final) nucleus $\boldsymbol{I}_1$ (or $\boldsymbol{I}_2$) and the projectile spin, in this case $\boldsymbol{I}_\mathrm{p}$. The total spin $\boldsymbol{J}$ is then given by the coupling of the channel spin $\boldsymbol{s}$ (or $\boldsymbol{s}'$) with the orbital angular momentum $\boldsymbol{l}$ (or $\boldsymbol{l}'$). The parity is simply defined to be odd for negative values of l and even for positive values of l.

CHANNEL SPIN REPRESENTATION

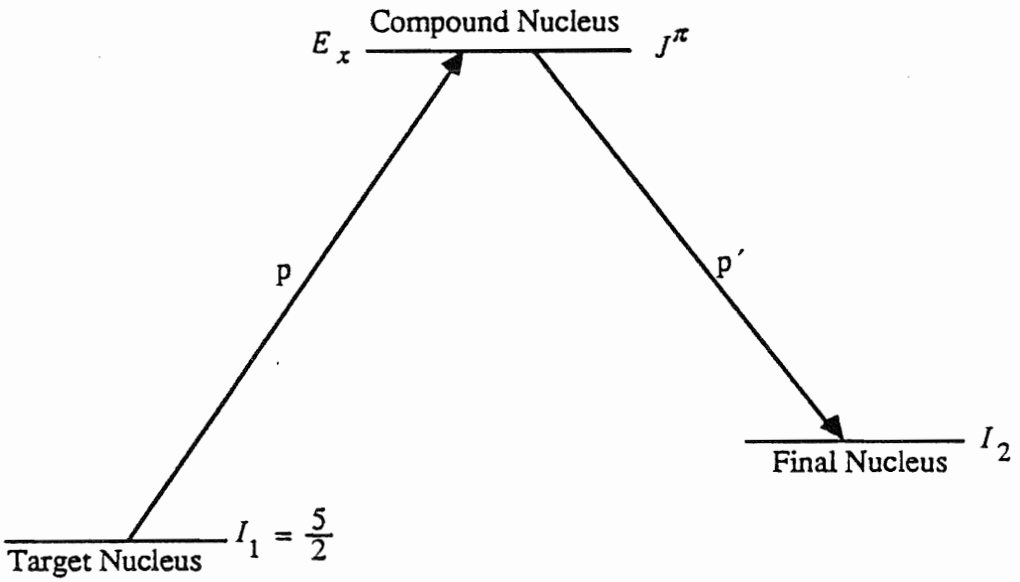

$$s = I_{\text{target}} \oplus I_{\text{projectile}}$$

$$= I_1 \oplus I_p$$

$$= \frac{5}{2} \oplus \frac{1}{2}$$

$$= 2, 3$$

$$s' = I_2 \oplus I_p$$

$$J = s \oplus l$$

$$\pi = (-1)^l$$

The goal here is to derive an expression that describes nuclear cross sections with as few assumptions about the form of the nuclear force as possible. This is done in two steps. First, the cross section is connected to the asymptotic part of the wavefunction via a collision or scattering matrix **U**. This step is concerned solely with the geometry of the experimental setup, and only the results will be presented here. Next, the collision matrix is connected to the parameters of nuclear resonant states via the **R**-matrix. The elements of **U** give the amplitude of a final spin state in the outgoing spherical wave if a particular pure initial spin state is selected. The most general form of **U** is restricted by the symmetry requirements that it be invariant under rotation (conservation of angular momentum), spatial reflection (conservation of parity), and time reversal. If identical particles are involved in the scattering, then the exclusion principle dictates that the form of **U** remain unchanged under the exchange of particle labels and that the total wave function satisfy the usual symmetry requirements for identical bosons or fermions. The mathematical complexity of the scattering matrix is determined by the number of independent amplitudes required to describe the scattering.

In order to extract parameters for resonant states of the compound system, a nuclear reaction theory is sought which provides a direct connection between the wave functions in the asymptotic region and a complete set of nuclear states in the interaction region. In the Wigner-Eisenbud formulation of *R*-matrix theory (Wigner and Eisenbud, 1947; Lane and Thomas, 1958; Vogt, 1962), this connection is established by equating the logarithmic derivatives of internal and external wave functions at a suitable radius a_c for each channel. The following discussion will be restricted to the *R*-matrix formalism, since it has been commonly used to determine nuclear level parameters.

1. Exterior Region

Assuming a spherical nucleus implies separation of the radial and angular parts of Schrödinger's equation. Therefore, the radial part is:

$$H\phi = -\left(\frac{\hbar}{2m}\right)\frac{d^2\phi}{dr^2} + V^{\text{ext}}\phi = E\phi \tag{2.8}$$

where, for the exterior region, the potential is simply the Coulomb potential plus possibly a centrifugal term:

$$V^{\text{ext}} = \frac{\hbar^2}{2m_\alpha}\frac{l(l+1)}{r^2} + \frac{Z_1 Z_2 e^2}{r^2} \tag{2.9}$$

where m_α is the reduced mass for the particle pair α. For l = 0, the wave function outside the potential well can be expressed as a linear combination of incoming waves

$$I \equiv (4\pi v)^{-1/2} e^{-ikr} \tag{2.10}$$

and outgoing waves

$$O \equiv (4\pi v)^{-1/2} e^{ikr} \tag{2.11}$$

thus:

$$\phi^{\text{ext}} = I - e^{2i\delta} O, \quad r > a_c \tag{2.12}$$

where v is the relative velocity, k is the wave number, and δ is the phase shift due to the interaction with the potential well. The cross section can then be expressed as:

$$\sigma = \left(\frac{4\pi}{k^2}\right)\sin^2\delta = \frac{\pi}{k^2}|1-U|^2 \quad \text{for } U \equiv e^{2i\delta}. \tag{2.13}$$

In order to include terms for $l \neq 0$, the wave functions can be expressed in terms of the regular and irregular solutions of the Coulomb equation $F_l(k_c r_c)$, in terms of Bessel functions, and $G_l(k_c r_c)$, in terms of Neumann functions:

$$I_c = (G_l - iF_l)e^{i\omega_c}$$
$$O_c = (G_l + iF_l)e^{-i\omega_c} \tag{2.14}$$

where ω_c is the Coulomb phase shift:

$$\omega_c = \sum_{n=1}^{l} \tan^{-1}\frac{\eta_c}{n} \tag{2.15}$$

and η_c is the Coulomb parameter which depends on the charges Z_1 and Z_2 of the pair of reaction products and on their relative velocity v_c:

$$\eta_c = \frac{Z_1 Z_2 e^2}{\hbar v_c} \quad . \tag{2.16}$$

Following the convention of Lane and Thomas (1958), the total external wave function can then be expressed as a product of the orbital and spin wave functions and a superposition of I_c and O_c:

$$\Psi_{\alpha sv}^{\text{complete}} = \frac{i\lambda}{r}\sqrt{\frac{\pi}{v}} \sum_{\alpha' s' l' m' V' l} (2l+1)^{1/2} \left[\delta_{cc'} I_{c'} - U_{cc'} O_{c'}\right] Y_{l'}^{m'} \chi_{sv'} \quad . \tag{2.17}$$

Considering only the incoming portion of this wave and using equation (2.15), the wave function can be written as:

$$\Psi_{\alpha sv}^{\text{inc}} = \frac{1}{k_\alpha \sqrt{v_\alpha}} \sum_l i^l (2l+1) e^{i\omega_{\alpha l}} \left(\frac{F_{\alpha l}}{r_\alpha}\right) P_l(\cos\theta_\alpha) \psi_{\alpha sv} \quad . \tag{2.18}$$

This function has the same asymptotic form as the partial-wave expansion of equation (2.6). The differential cross section is then given by:

$$\frac{d\sigma_{\alpha s v,\alpha' s' v'}}{d\Omega_{\alpha'}} = \left|A_{\alpha' s' v',\alpha s v}(\Omega_{\alpha'})\right|^2 \tag{2.19}$$

where

$$A_{\alpha' s' v',\alpha s v}(\Omega_{\alpha'}) = \frac{\sqrt{\pi}}{k_\alpha}\Big\{-C_{\alpha'}(\theta_{\alpha'})\delta_{\alpha' s' v',\alpha s v} + i\sum_{l'm'l}(2l+1)^{1/2} \times\left[e^{2i\omega_{\alpha' v'}}\delta_{\alpha' s' l' v' m',\alpha s l v 0} - U_{\alpha' s' l' v' m',\alpha s l v 0}\right]Y_m^l(\Omega_{\alpha'})\Big\}. \tag{2.20}$$

The next step is to find an expression for **U** in terms of the resonance parameters. In the next section, an expression will be found for the **R**-matrix, which can be related to **U** by applying appropriate boundary conditions.

2. Interior Region

For this scattering problem, resonances occur when the wave function has a slope that is very close to zero at the boundary $r_c = a_c$. As the incident particle energy approaches an energy corresponding to a resonance, the internal wave function may be considered to be similar to a standing wave. The reflection which occurs at the edge of the potential well serves to keep any outgoing particle in the well for a long time before it escapes. As a result, the internal wave function may be expanded in terms of a complete set of standing waves. In this expansion often one term dominates, corresponding to the one standing wave function of the resonance. The standing waves are the resonance levels of the compound nucleus. The retention of only one term in the Fourier expansion leads to the Breit-Wigner formula. Let X_λ form a complete

orthonormal set of functions. Then, the Hamiltonian for the interior region is:

$$HX_\lambda = \left[\frac{-\hbar^2}{2m}\nabla^2 + V^{\text{int}}(r)\right]X_\lambda = E_\lambda X_\lambda \tag{2.21}$$

where $V^{\text{int}}(r)$ is unknown. Expanding the interior wave function yields:

$$\phi^{\text{int}} = \sum_\lambda C_\lambda X_\lambda \tag{2.22}$$

where
$$C_\lambda = \int_0^{a_c} X_\lambda^* \phi^{\text{int}}\, dr \,. \tag{2.23}$$

Let the boundary parameter b be defined as:

$$r_c \frac{dX_\lambda}{dr_c}\bigg|_{s_c} = b_c X_\lambda (r_c = a_c) \,. \tag{2.24}$$

For the case of elastic scattering, the entrance channel is equal to the exit channel, and the expressions are greatly simplified. In this case, evaluating the expansion coefficients in terms of the resonance parameters and applying Green's theorem yields:

$$\phi^{\text{int}}(a_c) = \mathcal{R}\left[\phi'(a_c) - b\phi(a_c)\right] \tag{2.25}$$

where

$$\mathcal{R} \equiv \sum_\lambda \frac{\gamma_\lambda^2}{E_\lambda - E} \tag{2.26}$$

and

$$\gamma_\lambda^2 \equiv \left(\frac{\hbar^2}{2ma_c}\right)\left|X_\lambda(a_c)\right|^2 \,. \tag{2.27}$$

The $\mathcal{R}$ function is the Fourier expansion of that part of the phase shift which refers to the properties of the square well. It is equal to Green's function for the potential relating the internal and external wave functions evaluated at the boundary. If the energy E is close to one particular E_λ, one can approximate $\mathcal{R}$ by one term:

$$\mathcal{R} \approx \frac{\gamma_\lambda^2}{E_\lambda - E}. \tag{2.28}$$

This approximation is called the single-level approximation.

By following this same method, but replacing functions everywhere by vectors in the channel-configuration space, the corresponding matrix relations are obtained:

$$\phi_c^{\text{int}} = \sum_{c'} R_{cc'} \{\phi'_{c'} + b_{c'} \phi_{c'}\} \tag{2.29}$$

where:

$$R_{cc'} = \sum_\lambda \frac{\gamma_{\lambda c} \gamma_{\lambda c'}}{E_\lambda - E} \tag{2.30}$$

and:

$$\gamma_{\lambda c} = \left(\frac{\hbar^2}{2m_c a_c}\right)^{\frac{1}{2}} \int \psi_c^* X_\lambda \, dS_c. \tag{2.31}$$

$R_{cc'}$ represents the elements of the **R**-matrix. Its rows and columns refer to channels. The diagonal elements refer to reactions for which $c = c'$, and therefore correspond to elastic scattering. The off-diagonal elements refer to nonelastic scattering. The parameter $\gamma_{\lambda c}$ is the square root of the reduced width for the channel c and the level λ, and E_λ is the energy of the stationary state X_λ. The terms $\gamma_{\lambda c}$ and E_λ are a set of numbers that do not depend on the energy E, but do depend on the boundary condition numbers b_c. By matching the logarithmic derivatives of the external and internal wave

functions at the boundary of the nuclear surface, the matrix **U** can be expressed in terms of the matrix **R** and used in equation (2.20) to obtain an expression for the differential cross section in terms of the resonance parameters.

3. Boundary Condition

We define the logarithmic derivative of the outgoing wave O_l at the boundary as:

$$L_c \equiv \frac{O'}{O} - b_c \equiv S_c + iP_c \tag{2.32}$$

where S_C is the shift function and appears in the expression for the level shift, and P_C is the penetrability and is proportional to the probability of transmission through the external barrier. These are given by:

$$S_c = -b_c + \frac{F_c F_c' + G_c G_c'}{F_c^2 + G_c^2} \tag{2.33}$$

and:

$$P_c = \frac{k_c r_c}{F_c^2 + G_c^2} \tag{2.34}$$

where both P_C and S_C are evaluated at the channel radius $r_C = a_C$.

In order to obtain expressions for the cross sections as a function of energy in terms of the resonance parameters, one applies the boundary condition of matching the logarithmic derivatives of the external and internal wave functions. Specifying the logarithmic derivatives at one point for all energies is equivalent to specifying the cross section for all energies.

Matching the logarithmic derivatives yields a relation for the collision matrix in terms of **R**:

$$U_{cc'} = e^{i(\omega_c+\omega_{c'}-\phi_c-\phi_{c'})}\left[\delta_{cc'} + 2iP_c^{1/2}\frac{1}{1-R_{cc'}L_{c'}}R_{cc'}P_{c'}^{1/2}\right] \tag{2.35}$$

where ω_c is the Coulomb phase shift and ϕ_c is the hard-sphere phase shift. The collision matrix element $U_{cc'}$ is the amplitude of the outgoing wave in channel c′ that is associated with the particular incoming wave in channel c. For example, if c′ = c, this collision matrix element describes elastic scattering. Retaining only one level in the various sums leads to the Breit-Wigner formula, regardless of the number of channels.

The above approximation is based on the assumption of hard-sphere potential scattering, i.e., an abrupt nuclear surface. However, analyses of many nuclear reactions with the optical model suggests that a real diffuse-edge potential would be more appropriate. It can be shown (Vogt, 1962) that the only important change in going from a real square-well to a diffuse-edge potential based on a Woods-Saxon optical model is an increase in the penetrability by a factor of typically 2.67, resulting from the difference in the reflection properties of the two potentials. In the case of a p-wave particle instead of an s-wave particle, the shift function varies appreciably with energy, and must also be multiplied by the reflection factor 2.67. The boundary condition numbers required to cause the level shifts to vanish are also energy dependent, but, under most circumstances encountered in low energy nuclear reactions, the error introduced by neglecting this effect is negligible.

One of the intrinsic difficulties of this treatment is the choice of the channel radii. The radius should be large enough to include the nuclear interactions within the nucleus. If this is true, then the shift functions and penetrabilities are the conventional ones. However, if the radius is too large, the hard-sphere phase shifts and penetrabilities vary too rapidly with energy.

For unpolarized incident and target projectiles, the differential cross section from equation (2.20) can be summed over the different spin orientations to obtain:

$$\frac{d\sigma_{\alpha sv,\alpha' sv'}}{d\Omega_{\alpha'}} = (2s+1)^{-1} \sum_{vv'} \left| A_{\alpha' sv',\alpha sv}(\Omega_{\alpha'}) \right|^2 . \tag{2.36}$$

Transforming the expression for the scattering amplitude $A(\Omega)$ into the quantum numbers of the channel spin representation yields the multichannel, multilevel expression:

$$\frac{d\sigma_{\alpha s,\alpha' s'}}{d\Omega_{\alpha'}} = \frac{\pi}{k_\alpha^2} \left| C_{\alpha'}(\theta_{\alpha'}) \right|^2 \delta_{\alpha' s',\alpha s} + \frac{\sum_L B_L(\alpha' s', \alpha s) P_L(\cos\theta_{\alpha'})}{k_\alpha^2 (2s+1)}$$

$$+ \frac{\sqrt{\pi}}{k_\alpha^2 (2s+1)} \sum_{Jl} (2J+1)\, \delta_{\alpha' s' l',\alpha s l}\, \Re\left[i T^J_{\alpha' s' l',\alpha s l} C_{\alpha'}(\theta_{\alpha'}) P_l(\cos\theta_{\alpha'}) \right] \tag{2.37}$$

where:

$$B_{L(\alpha' s',\alpha s)} = \frac{1}{4} (-1)^{s-s'} \sum_{J_1 J_2 l_1 l_2 l_1' l_2'} \bar{Z}(l_1 J_1 l_2 J_2, sL)$$

$$\times \bar{Z}(l_1' J_1 l_2' J_2, s' L) \left(T^{J_1}_{\alpha' s' l_1', \alpha s l_1} \right) \left(T^{J_2}_{\alpha' s' l_2', \alpha s l_2} \right)^* \tag{2.38}$$

$$T^J_{\alpha' s' l',\alpha s l} = \exp(2i\omega_{\alpha' l'})\, \delta_{\alpha' s' l',\alpha s l} - U^J_{\alpha' s' l',\alpha s l} \tag{2.39}$$

and C_α are given by equation (2.23). The $\bar{Z}$ coefficients are related to the Z coefficients of Blatt and Biedenharn (1952), and the $P_l(\cos\theta)$ are the Legendre polynomials with the phase convention of Condon and Shortley (1951).

The first term of equation (2.37) represents pure Coulomb scattering, the second term represents resonance scattering and reactions, and the last term is the

interference between the first and second terms. This is the expression used by the program MULTI6 to calculate cross sections to compare with experimental yield curves. The Coulomb and the interference term vanish except in the case of pure elastic scattering. For nonelastic scattering, the remaining reaction term has the same energy and spin dependence as the resonance term. Since the reaction cross sections for different channel spins add incoherently, there are no cross terms.

In general, the *R*-matrix procedure of analyzing experimental data consists of calculating the cross section (including Coulomb, hard-sphere, and resonance scattering contributions) in terms of certain entrance and exit channels, described by the projectile and target masses and charges, the reaction *Q*-value, the allowed spins and orbital angular momenta, etc. The calculated cross section is required to fit, as closely as possible, the experimentally derived cross section by varying the parameters describing the resonances. These include the energies, angular momenta, channel spins, orbital angular momenta, and widths.

4. Application to Resonance Analysis

The collision matrix takes on a more familiar form if it is restricted to single level, single channel elastic scattering. For c′ = c, equation (2.35) becomes:

$$U_{cc} = e^{2i(\omega_c - \phi_c)}\left[1 - \frac{2iP_c\gamma^2}{E_\lambda - E - \gamma^2(S_c - b_c) - iP_c\gamma^2}\right] \tag{2.40}$$

where S and P are the shift function and the penetrability of equations (2.33) and (2.34), and b_c is the boundary parameter defined in equation (2.24). By defining the laboratory width $\Gamma \equiv 2P\gamma^2$ and the level shift $\Delta_\lambda \equiv \gamma^2(S - b_c)$, the expression can be written as:

$$U_{cc} = e^{2i(\omega_c - \phi_c)}\left[1 - \frac{i\Gamma}{\left(E_\lambda - E - \Delta_\lambda\right) - \frac{i\Gamma}{2}}\right] \tag{2.41}$$

which is the well-known Breit-Wigner formula. The apparent resonance energy is different from the eigenstate energy E_λ by the amount Δ_λ which depends on the shift function S. In most cases the energy dependence of Δ_λ is negligible through the width of a resonance. Therefore, for this analysis and in keeping with past convention, the level shift Δ_λ is set equal to zero for each resonance. From the definition of Δ_λ above, this sets the boundary parameter equal to the shift function.

The laboratory width Γ of equation (2.41) depends on the penetrability and the reduced width. The probability of a nucleus in an excited state decaying via a particular exit channel is dependent on both the strength of the given channel in the intermediate state and the Coulomb-angular momentum barrier penetrability. In order to compare the relative widths of excited states at different excitation energies, or of states formed via different entrance channels, the kinematic effects inherent in the laboratory widths must be removed. The reduced width is:

$$\gamma_{\alpha sl}^2 = \frac{\Gamma_{\alpha sl}}{2P_l(E)} \tag{2.42}$$

where the penetrability factor $P_l(E)$ contains the kinematic effects due to centrifugal and Coulomb forces. The reduced width amplitude for a given channel is a constant $(\hbar^2/2m_c a_c)^{1/2}$ times the wave function evaluated at the channel surface. It is conventional to define the single-particle reduced width as:

$$\gamma_{sp}^2 = \frac{\hbar^2}{2m_c a_c^2} \tag{2.43}$$

where $m_c = m$ for a single nucleon incident on a target nucleus, and a_c is the channel radius. This definition utilizes the Wigner limit with a factor of 1/2 following the

convention of Bilpuch (1976), which has provided good results for elastic proton scattering data. If one assumes a_c = 1.25 ($A_1^{1/3}$ + $A_2^{1/3}$) F, then for ^{25}Mg, γ_{sp} = 860 keV. The spectroscopic factor is then defined as:

$$S_p = \frac{\gamma_p^2}{\gamma_{sp}^2} \quad . \tag{2.44}$$

The spectroscopic factors from the (p,p) reaction can be determined for individual resonances, and compared with the spectroscopic factors for these states obtained from other reactions such as (^{3}He,d) and (α,t). Chapter VI contains a comparison of the spectroscopic factors for the 5^- and 6^- states measured in this experiment with the corresponding spectroscopic factors obtained from the proton transfer reactions.

C. High Spin States

1. Importance of High Spin States

The interaction between two nucleons in free space does not accurately reproduce effects inside the nucleus. Within the nucleus, the interaction between any two nucleons is influenced by the presence of the mean field produced by the other nucleons. The nucleon-nucleon (N-N) effective interaction attempts to take into account these effects, and is primarily composed of a central force, a spin-orbit force, and a tensor force. Methods are continually sought to unfold the different components of the effective interaction.

Moffa and Walker (1974) first proposed comparing (p,p′) and (p,n) data with (e,e′) results for high spin states (large values of *J*). Because the reaction mechanism for leptonic probes such as electrons is relatively well understood, a comparison of

electron scattering results with (p,p′) and (p,n) data would provide a means of gaining information about the effective interaction. High spin particle-hole "stretched" states are particularly useful. States are said to be "stretched states" if the total spin is the maximum value allowed for the value of the orbital angular momentum (see figure 2.3). For example, a proton incident on a ^{25}Mg target nucleus with $l = 3$ can excite a $J^{\pi} = 6^-$ stretched state in ^{26}Al. Such a state would arise primarily from the $(f_{7/2}d_{5/2}^{-1})$ particle-hole configuration, and would represent a fairly pure single-particle shell-model state. The nearly stretched $J^{\pi} = 5^-$ state, although not uniquely of the $(f_{7/2}d_{5/2}^{-1})$ configuration, can only be formed in a limited number of ways and therefore is also of interest. In practice the 5^- states are also populated rather strongly in inelastic scattering and are sometimes included in studies of stretched states. By extracting spectroscopic factors from stretched states, a comparison can be made to the strength predicted by the simple shell model, also known as the extreme single-particle-hole model (ESPHM). Studies of high spin states are now providing information on effective interactions along with nuclear structure information, and also are serving to test theoretical descriptions of inelastic scattering and reaction models. A discussion of the N-N effective interaction is found in (Love, 1984), and applications to spin excitations via electromagnetic and hadronic probes is found in (Lindgren and Petrovich, 1984).

Certain states exhibit "missing strength" in comparison with standard predictions such as that given by the ESPHM. This is known as "quenching". A famous example of this is the Gamow-Teller resonance. Quenching has also been observed in high spin states. Several explanations for the missing strength have been proposed. Some say the missing strength goes into the transformation of a nucleon into a delta particle (Teller, 1984). Another consideration is including π- and ρ-meson

Figure 2.3 A description of stretched states in both the *j-j* and the *L-S* coupling schemes. The usual description of a stretched particle-hole state involves lifting one particle into the next major shell with both particle and hole having the maximum angular momentum for the respective shells, and these two angular momenta coupled to their maximum or "stretched" value. In the present study the stretched state is $(f_{7/2}d_{5/2}^{-1})$ $J^{\pi} = 6^{-}$. The *j-j* coupling scheme illustrates the particle-hole description of this state. The *L-S* coupling scheme shows the channel spin representation of the stretched state.

j-j Coupling

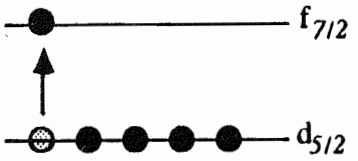

$(f_{7/2}, d_{5/2}^{-1})$

$j_p = l_p + 1/2 \qquad j_h = l_h + 1/2$

$= 3 + 1/2 \qquad = 2 + 1/2$

$= 7/2 \qquad = 5/2$

$J = j_p + j_h = 6$

L-S Coupling

Channel spin s given by $I_{target} \oplus I_{projectile}$:

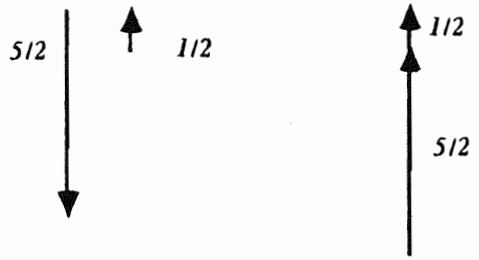

$s = 2 \qquad s = 3$

Total spin J given by $s \oplus l$:

$J = 3 + 3 = 6$

exchange effects in the effective interaction. This is described in the Meson Exchange Current (MEC) model.

Another explanation for quenching is that perhaps the stretched state serves as a doorway state to multiparticle, multihole configurations. This is called "fragmentation" of the state. Fragmentation is a result of the presence of states of the same spin and parity and almost the same energy as the doorway state, but of a different shell-model configuration. Such states would share some of the strength of the doorway state. The strengths of these states could be so small that they would not have been observed with the experimental resolution available in the previous experiments.

Fragmentation is expected to be minimized near closed-shell nuclei and strongest for deformed nuclei. For example, fragmentation is observed in the $(d_{5/2},p_{3/2}^{-1})$, 4^- and the $(f_{7/2},d_{5/2}^{-1})$, 6^- particle-hole states in the deformed nuclei ^{14}C and ^{26}Mg, respectively, whereas the same stretched configurations in the nuclei ^{16}O and ^{28}Si are observed primarily in single states. Comparison with structure calculations of the measured strength and fragmentation of these stretched states provides an important test of such calculations. Such comparisons are needed for both spherical and non-spherical nuclei.

2. Current Experimental Status

Stretched states in the nuclei ^{24}Mg, ^{26}Mg, and ^{26}Al were studied via the reactions $^{25}Mg(\alpha,^3He)^{26}Mg$ (Kraushaar *et al.*, 1986) and $^{25}Mg(\alpha,t)^{26}Al$ (Peterson *et al.*, 1986). Comparisons were made to distorted-wave Born approximation (DWBA) calculations. Considerably more fragmentation was observed in the mass 26 system than had been observed in the mass 28 system. Approximately 27% of the predicted

strength for $J^{\pi};T = 6^{-};1$ in ^{26}Mg was found, and 31% of the $6^{-};0$ strength and 59% of the $6^{-};1$ strength in ^{26}Al was found in these studies.

A summary of electron scattering calculations using Harmonic Oscillator (HO) and Woods-Saxon (WS) wave functions is presented in (Clausen *et al.*, 1988) and a comparison is made to data for 4^{-} states in ^{12}C, ^{14}C, and ^{16}O, 6^{-} states in ^{24}Mg, ^{26}Mg, and ^{28}Mg, 8^{-} states in ^{48}Ca, ^{54}Fe, ^{58}Ni, and ^{60}Ni, the 10^{-} state in ^{90}Zr, and the 14^{-} state in ^{208}Pb. The effect of meson exchange currents (MEC) was also computed, and the influence of WS and HO wave functions was compared. The inclusion of MEC effects was found to increase the theoretical predictions between 15 and 20%, which would further decrease the fraction of the strength observed experimentally. The data for the low mass nuclei, where experimental results are the most complete, were found to exhibit greater fractions of the calculated WS strengths, totaling 105% for ^{12}C and 81% for ^{16}O. Thus, the use of a WS wave function significantly decreases the amount of quenching observed for light nuclei. While this decrease is less dramatic in heavier nuclei (A>16), unobserved weak states could account for the missing strength in those nuclei.

Recently, more exhaustive studies of stretched states in ^{26}Al have been conducted. The reaction ^{25}Mg(^{3}He,d)^{26}Al (Peterson *et al.*, 1988a) reports good agreement with the earlier (α,t) experiment. Peterson *et al.* also studies the reaction ^{27}Al(p,d)^{26}Al (1988b). The reaction ^{26}Mg(p,n)^{26}Al was used to observe the particle-hole states $(d_{5/2},d_{5/2}^{-1})$ 5^{+} and $(f_{7/2},d_{5/2}^{-1})$ 6^{-}; T = 0, 1, and 2 (Lebo *et al.*, 1988). Fragmentation is observed in both 5^{+} and 6^{-} states, especially the T = 1 component of 6^{-}. When compared to the ESPHM, 73% of the $5^{+};0$ strength is observed; 73% is found in $6^{-};0$, 61% in $6^{-};1$, and 27% in $6^{-};2$. The magnitude and distribution of the 5^{+} strength is well described by shell-model calculations. The general distribution of the

6^- states is as predicted, but quantitative agreement with a shell-model calculation is poor. More extensive shell-model calculations are called for, along with experiments with higher resolution to search for smaller, fragmented states. Also, experiments have been performed using pion scattering on ^{24}Mg, ^{26}Mg, and ^{28}Si.

3. Current Experiment

One motivation of the current experiment is to confirm the proposed 6^- stretched state that has been observed at E_x = 9.26 MeV (Peterson *et al.*, 1988b). With the resolution obtainable at TUNL, a definitive spin and parity assignment should be possible.

Another resonance in question is near E_x = 8.6 MeV. The studies mentioned above indicate the existence of a stretched state at this energy. This lies within the energy range of data taken previously at TUNL (Adams, 1983). These data will be reanalyzed, and an updated list of spin and parity assignments will be given in Chapter VI.

In addition to confirming the existence of these states, this study hopes to search for fragmented states with the improved resolution. In Chapter VI spectroscopic factors will be obtained for any stretched states that are found, and these will be compared to previous results.

CHAPTER III

EXPERIMENTAL EQUIPMENT

A. Introduction

The high resolution proton spectroscopy measurements for this dissertation were performed with the High Voltage Engineering Corporation (HVEC) Model K-3000 4 MV Van de Graaff positive ion accelerator. The single-ended horizontal accelerator and associated high resolution energy feedback system is located at Triangle Universities Nuclear Laboratories (TUNL) on the Duke University campus. The high resolution system has been described by Parks (1958), Seibel (1967), and Westerfeldt (1986). The incident proton energies for these measurements ranged from 1.9 MeV to 3.4 MeV. The overall resolution of the data was 300-400 eV, with 2 to 3 μA of beam on target and 20 to 40 nA of beam on the tuning ring. Thin-film carbon-backed targets were used. These measurements were performed with the charged particle scattering target chamber.

B. RF Ion Source and Van de Graaff Accelerator

A schematic of the accelerator, beam line, and feedback systems is shown in figure 3.1. A 100 MHz radiofrequency (RF) ion source at the terminal of the machine ionizes hydrogen that is leaked into a glass bottle. This produces both H^+ (atomic hydrogen or protons) and HH^+ (molecular hydrogen) ions. These ions are repelled by

Figure 3.1 Schematic of the High Resolution KN Van de Graaff single-ended horizontal accelerator, beam line, and energy feedback system.

High Resolution Laboratory and Control Systems

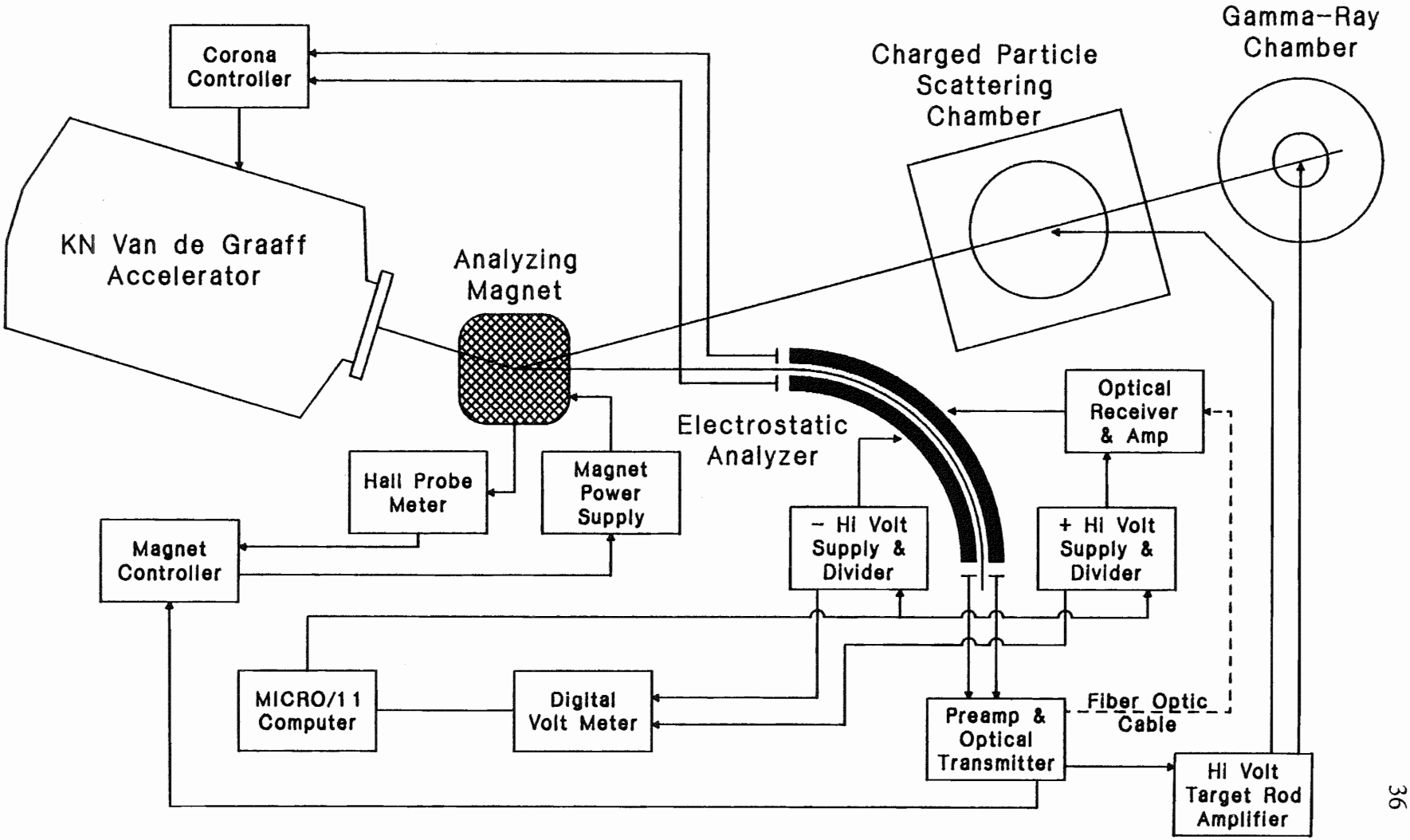

a positively biased probe in the end of the bottle. The ions then travel down an evacuated tube consisting of stainless steel plates alternated with insulating glass or ceramic rings. The terminal end of the machine has a stainless steel dome which is charged to a positive potential via a rubber impregnated cotton belt. A series of 600 MΩ resistors divides the dome voltage into equal steps. Each stainless steel plate in the accelerator tube is electrically connected to one of the resistors and provides a uniform potential gradient for the accelerator tube. This potential gradient accelerates the ions to the energy desired. Recent modifications in the analyzer biasing and feedback circuits allow operation at 4.0 MeV or higher and are described by Nelson (1983).

The accelerator tube, charging belt, and dome are enclosed inside a large tank filled with high pressure gas to prevent voltage breakdown from the dome to ground. The gas is a mixture of 80% nitrogen and 20% carbon dioxide dried to approximately 20 ppm of water, and is normally at 300 psig during operation of the accelerator.

C. Energy Feedback System

1. Analyzing Magnet

After being accelerated through the tube, the beam then reaches an analyzing magnet. The magnetic field of the magnet is maintained such that the HH^+ (molecular hydrogen) ions are deflected 17°, while the H^+ ions (protons) are deflected 25°. The beam therefore splits and travels down two different beam legs, with the molecular hydrogen beam going to an electrostatic analyzer and the proton beam going to the target chamber. As the desired energy of the beam is changed, the magnet setting is adjusted in order to keep the two beams focused down the two beam lines.

2. Electrostatic Analyzer

The HH^+ beam is sent to the electrostatic analyzer, which is basically a parallel-plate capacitor bent into a 90° arc. Two steel plates are placed approximately 4.5 mm apart, with a mean radius of curvature of approximately 1 m. The two plates are equally and oppositely biased, with the inner plate at a negative potential and the outer plate at a positive potential. As the molecular hydrogen beam enters the analyzer, the beam is bent by a horizontal force due to the electrostatic field between the plates. At the entrance and exit points of the electrostatic analyzer are metal slits through which the beam must pass. Due to the geometry of the analyzer, the beam will pass through both sets of slits when the beam energy is equal to 111 times the potential difference between the high voltage plates. The plates are biased such that the beam is centered on the entrance and exit slits if the beam is at the desired energy. When the beam energy falls below the desired energy, the beam is bent more as it passes through the analyzing magnet or through the analyzer. Since the magnet and the analyzer bend the beam in opposite directions, more current would then be intercepted by the left entrance slit and the right exit slit than by the right entrance slit and the left exit slit. Similarly, when the beam energy drifts above the desired energy, more current is intercepted by the right entrance slit and the left exit slit. Fluctuations in the beam energy thus cause a difference in the current readings between the slits. The entrance slits serve as object slits for the beam entering the analyzer and also generate a correction signal for the corona control system. The exit slits serve as the image slits and generate a correction signal for the outer plate of the electrostatic analyzer, the analyzing magnet, and the target rod.

3. Corona Feedback System

An assembly of stainless steel needles is mounted to the wall of the tank near the dome. Because of the high electric field surrounding the points of the needles, ions can be formed in the insulating gas, which then drift to the terminal where they reduce the dome potential. By changing the position of the needle assembly, the distance between the needles and the dome can be varied to regulate the current flow from the dome. Varying the potential on the corona needles also affects the current flow. In these two ways the dome potential, and thus the beam energy, can be controlled. The distance between the needles and the dome is adjusted manually as needed as the desired beam energy increases during the course of the experiment. The potential on the corona needles is controlled by the signal from the electrostatic analyzer entrance slits. Since the ions travel slowly through the tank gas (~25 ms drift time), only low frequency (<20 Hz) corrections to the dome potential can be achieved with the corona system. Irregularities in the belt charging system cause dome voltage fluctuations of 5 to 10 kV_{pp} at approximately 5 Hz. With corona control these fluctuations are reduced to about 2 kV_{pp} of 5 to 10 Hz.

4. Target Rod Voltage

To remove the smaller, faster fluctuations, corrections are applied to the target itself. The targets are mounted on a metal rod which is electrically isolated from ground. During data acquisition the target rod is biased to an initial value of +3 kV DC, which is then varied in order to provide a correction for fluctuations in the beam energy. Since the power supply for the target rod is capable of supplying 6 kV,

fluctuations of up to 6 keV_{pp} may be corrected. A correction signal from the exit slits of the electrostatic analyzer is sent to the target rod, and the bias is increased or decreased as needed to correct for fast fluctuations in the beam energy.

D. Steering Magnets and Focusing Slits

The beam optical elements have been described in detail by Warthen (1987). The ratio of molecular to atomic hydrogen can be adjusted by controlling the rate at which the hydrogen gas passes through a palladium leak into the bottle. The voltage of the probe in the bottle then determines the beam output, and the voltage of the first ring (focus electrode) of the tube determines the focal point of the beam. An X-Y electrostatic steerer focuses the beam into the analyzing magnet, which separates and bends the beam. For the electrostatic analyzer beam, only the focus electrode and electrostatic steerer (and magnetic field of the analyzing magnet) affect the position and focus of the beam. For manipulation of the beam entering the target chamber, there are also L-R-U-D steering magnets, a quadrupole doublet magnetic lens, and a second set of steering magnets.

E. Scattering Chamber, Detectors, and Target Rod

A top view of the charged particle scattering chamber and detector and collimator setup is shown in figure 3.2. The scattering chamber can be evacuated to approximately 10^{-7} torr. As the proton beam approaches the chamber, it is focused by a collimator assembly located in front of the entrance to the chamber. Five Ortec silicon surface barrier detectors were used to detect the scattered protons. The

Figure 3.2 Top view of the charged particle scattering chamber and detector setup.

Charged Particle Scattering Chamber

(Top View)

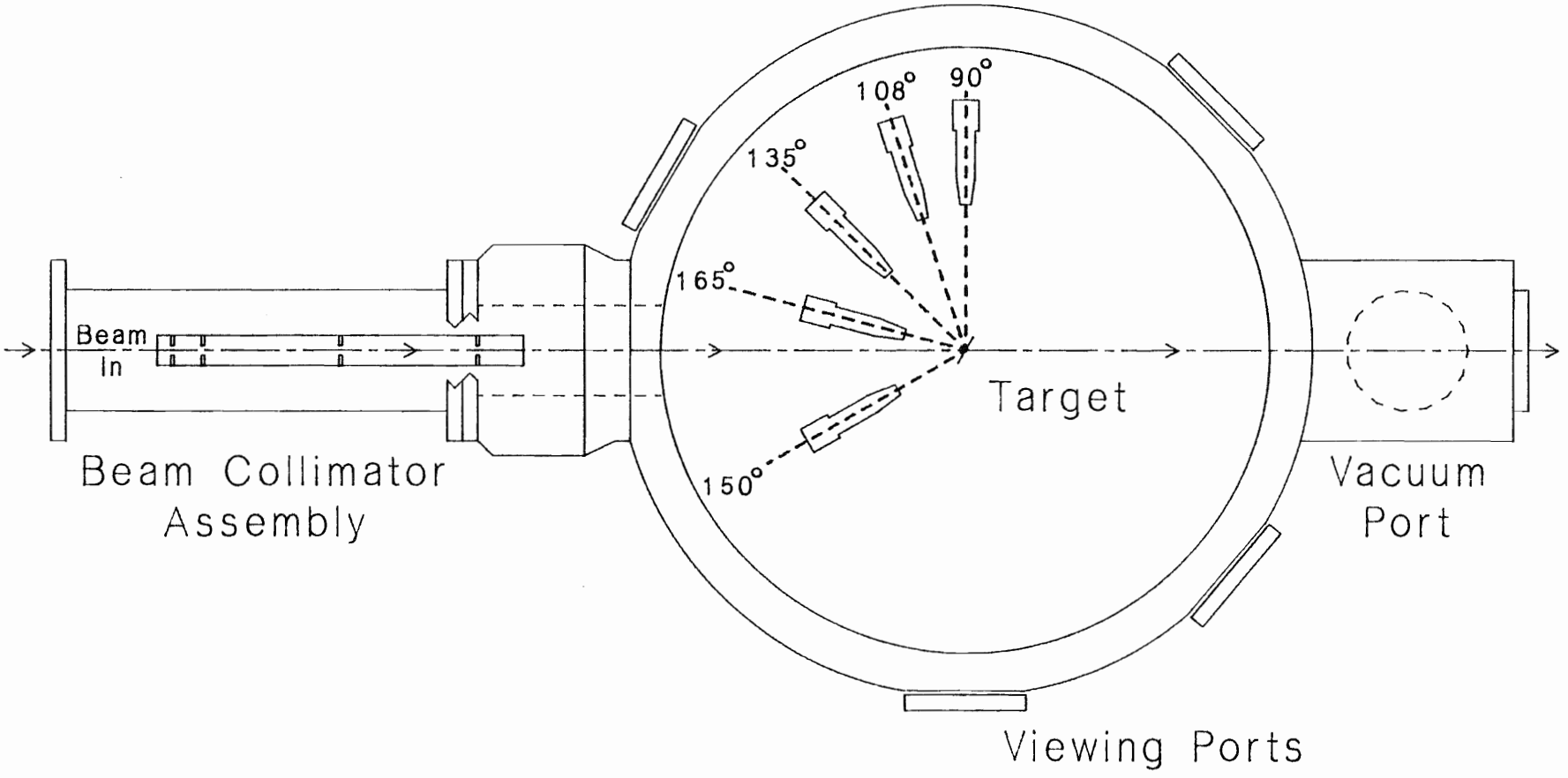

detectors have an active area of 50 mm^2 and a depletion depth of 300 microns. The detectors were placed at angles of 90°, 108°, 135°, 150°, and 165° with respect to the beam line. The target rod was rotated 25° with respect to the beam line during data acquisition in order to provide an unobstructed view of the target by each of the detectors. Through use of the tuning magnets and collimator assembly, the incoming proton beam was collimated to a spot on the target of approximately 1 mm in diameter. The detector solid angles are determined by collimators placed in front of the detectors and by the distance of the detector from the target. The solid angles are chosen such that the stainless steel target rings are obstructed from the view of the detectors while the beam spot on the target is completely contained by each of the detector solid angles. The detector solid angles ranged from 1 msr at 90° to 4.4 msr at 165°. Larger solid angles at back detectors helps equalize the counting statistics at all angles to compensate for increased Rutherford scattering in the forward angles.

F. Data Acquisition System

1. Electronics

Figure 3.3 shows the electronics setup used for the data acquisition for this experiment. When a scattered proton enters one of the five detectors in the target chamber, it produces an output signal. The pulse height of the signal is proportional to the energy of the detected particle. This signal is sent to an EEG ORTEC Model 142 preamplifier with a unity gain, and is then passed to an EEG ORTEC Model 572 linear amplifier. This linear amplifier has both a unipolar and a bipolar output, each ranging from 0 to 10 volts. The unipolar linear output is sent to an EEG ORTEC Model 476-8

Figure 3.3 Block diagram of the data acquisition system used with the High Resolution Laboratory Van de Graaff accelerator and VAX 11/750 computer.

Data Acquisition Electronics Setup

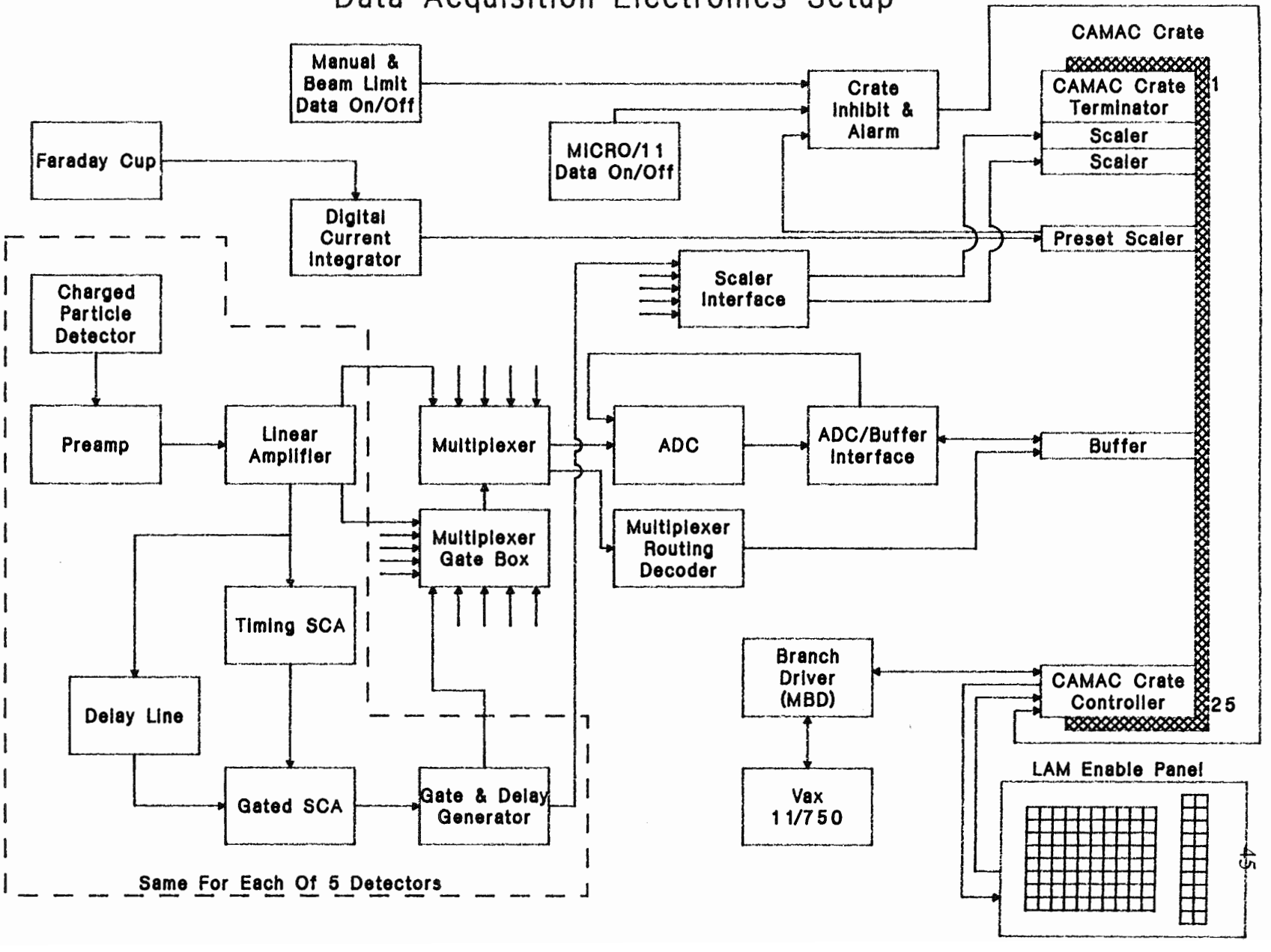

multiplexer after being delayed 2 μs internally. The bipolar linear output is sent to an ORTEC Model 420 Timing Single Channel Analyzer (TSCA) and then to a gated Hewlett Packard Model 5583A Single Channel Analyzer (HP SCA), and also in parallel to a delay line of 0.9 μs and then to the HP SCA. The ORTEC Model 420 TSCA sets a window on the carbon elastic scattering peak and, if the incoming signal is within this window, sends a signal to the HP SCA to reject the signal incoming via the 0.9 μs delay line. In this manner, the HP SCA accepts only those bipolar signals from the linear amplifier not corresponding to carbon scattering. The HP SCA outputs a signal to a multiplexer gate box and also to a gate and delay generator if the input signal is between the upper and lower discriminators. The multiplexer gate box processes logical pulses from each of the five HP SCAs (one for each detector). Upon receiving an input signal, the multiplexer gate box signals the multiplexer to accept the 0.9 μs delayed unipolar signal from the linear amplifier. The multiplexer only accepts signals accompanied by an "OK" (enable) signal from the multiplexer gate box, thus electronically gating out any signals due to the enormous carbon peak before they reach the analog-to-digital converter. By doing this, dead times are significantly reduced.

A Northern Scientific Model 621 analog-to-digital converter (ADC) digitizes the unipolar pulse from the multiplexer. This information is stored in one of two CAMAC ADC buffers before being dumped to a memory buffer in the VAX 11/750 via the Microprogrammable Branch Driver (MBD). The ORTEC Model 416A gate and delay module lengthens the signal from the HP SCA to a 5-volt logic pulse and sends it to a scaler interface each time a non-carbon-related signal is detected. These logic pulses are summed by a CAMAC scaler.

A Faraday cup intercepts the beam after it passes through the target chamber. A digital beam current integrator (BCI) measures beam current on the Faraday cup. When a predetermined value of current (the "preset") has been reached, a signal goes to the CAMAC crate and inhibits the data acquisition. At this time, a series of commands are executed, including writing the scalers and spectra to magnetic tape, summing the areas under the peaks of interest, incrementing the beam energy a predetermined amount, and shifting windows (if needed). Also, the sums from the CAMAC scaler are compared with the counts in the corresponding spectra, and the dead times are computed. This process is explained further in the next chapter. Data taking is then enabled again. A manual switch also allows the data acquisition to be inhibited at any time. In addition, there are manually set gates on the current meter which provide an inhibit signal when the beam drops below or surges above the desired current. Finally, the electrostatic analyzer provides a signal to a PDP-11 microprocessor which inhibits data acquisition when the beam energy differs by more than 10 eV from the desired energy.

2. Computer

The data for this experiment were handled by a VAX 11/750 computer using the VMS operating system. The information from each spectrum was sent from the electronics setup to the computer and was then stored on magnetic tape, along with sufficient information about the spectrum, e.g. incident proton energy, to reproduce the yield curve. Data from a typical week-long experiment would fill nearly two magnetic tapes.

3. Data Acquisition Software

The raw data for this experiment were manipulated using the data acquisition software package XSYS, developed at TUNL for VAX computers (King, 1981). An overview of XSYS and its development is given by Gould (1981). The XSYS Reference Manual (Boyd 1984) describes the actual use of XSYS. Specialized XSYS Fortran programs to automatically produce excitation curves and provide automatic control of beam energy have been written for the High Resolution Group (Warthen, 1987). The Fortran programs used for the offline data analysis are described briefly in the next chapter.

In order to decrease the dead times, the data handling programs were combined into a single master program. This program was then installed as a subprocess on the VAX 11/750. This subprocess "hibernates" during data acquisition and is "awakened" when preset is reached. This method was designed primarily by Bull, and is described in his dissertation (Bull, 1989).

G. Targets

The targets used in this experiment were thin-film targets prepared by evaporation deposition of the element of interest onto self-supporting carbon foil backings. Carbon backings are chosen because of their good vacuum properties, good thermal and electrical conductivity, resistance to high temperatures, and mechanical strength. In addition, the low mass of carbon leads to minimal interference with the nuclear reactions of interest. The carbon foils used for this experiment ranged from 4.3 to 5.0 $\mu g/cm^2$ thick and were obtained from the Arizona Carbon Foil Co. The foils

were floated from glass slides onto stainless steel target rings and placed in a bell jar. A diagram of the evaporation setup is shown in figure 3.4. The target rings were placed on a stand approximately 3.5" above a metal boat containing the element of interest, and the bell jar was evacuated to approximately 10^{-7} Torr. Evaporation was achieved by sending a current of approximately 200 A through the metal boat via two copper electrodes. A shutter could be placed between the boat and the targets and/or moved out of the way by turning the rod on which the shutter is mounted.

The literature (Thomas, 1982; Takayanagi, 1966; Heagney, 1972; Szalay, 1967) contains descriptions of several different methods of making thin-film magnesium targets. The isotope ^{25}Mg is available commercially in the form of magnesium oxide powder in purities of 98.25% enrichment. In order to obtain good resolution, it is desirable to reduce the oxygen contamination as much as possible. Several reducing agents were considered. Although the use of zirconium and aluminum has been described in the literature, tantalum seemed the most likely candidate.

Magnesium oxide reacts with tantalum at approximately 1800° C, well above the melting point of magnesium, but well below the melting point of both magnesium oxide and tantalum. Therefore it would seem that the tantalum would reduce the magnesium oxide at a temperature near 1800° C, and the newly reduced magnesium would immediately evaporate, leaving the tantalum and any unreduced magnesium oxide in the boat. The sublimation point for magnesium at 10^{-6} Torr is 247° C, and for tantalum it is 2240° C. Therefore the desired temperature of the mixture in the boat is between 1800° C and 2200° C.

Adams (1983) found the best technique for evaporating magnesium onto carbon foil backings to be magnesium oxide power in tungsten boats, without a reducing agent. He records that the evaporation of magnesium oxide occurred at approximately

Figure 3.4 Diagram of the bell jar and evaporation deposition setup used to produce thin-film carbon-backed magnesium targets.

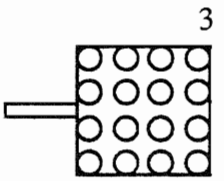

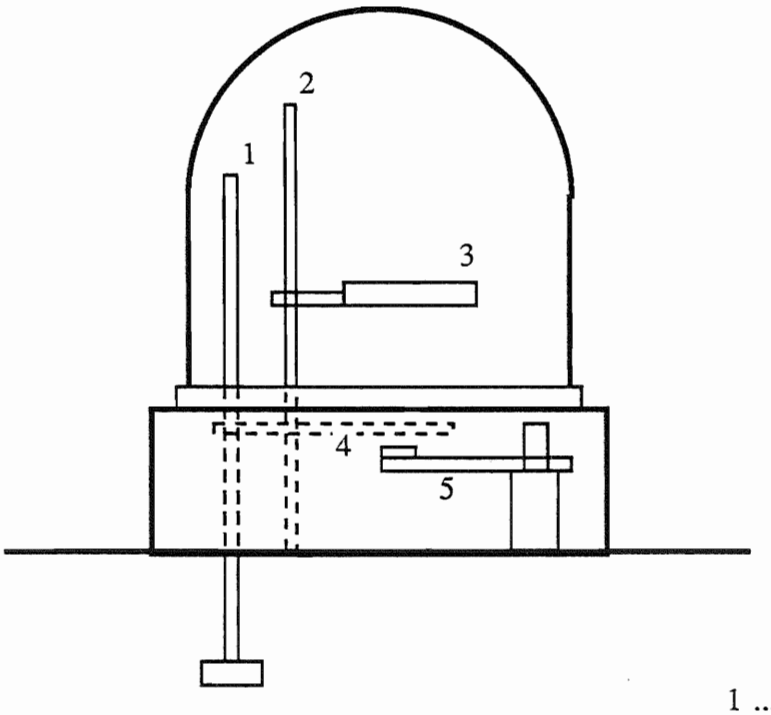

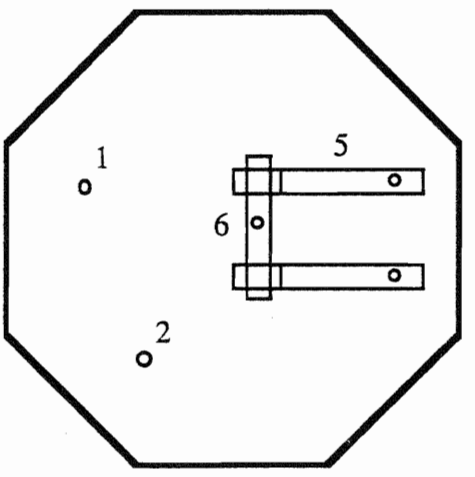

1 ..... Shutter Post

2 ..... Target Post

3 ..... Target Holder

4 ..... Shutter

5 ..... Cu Electrodes

6 ..... Ta Boat

1600° to 1700° F (~890° C), as estimated with a Leeds and Northrup Optical pyrometer. For the present experiment, Maxtek TM-100 Thickness Monitor was used to monitor the amount of substance being evaporated. As increasing amounts of substance are deposited on the quartz crystal of the Thickness Monitor, the frequency of oscillation of the crystal decreases. The TM-100 provides a direct display of film thickness and deposition rate during evaporation from stored parameters dependent on the substance being evaporated and the geometry of the evaporation setup. The sensor was sufficiently close to the targets that the distance between the sensor and boat was considered equal to the distance between the targets and boat. The film density and acoustic impedance parameters of magnesium, as given in table 7.1 of the Operation and Service Manual of the Thickness Monitor, were used: 1.74 and 5.48, respectively. Given the correct input parameters for the substance being evaporated, the TM-100 should give an accurate value for the amount of substance deposited on the crystal of the thickness monitor, but it cannot identify the material that is being evaporated. The TM-100 is used by several people evaporating different substances. At any given time, the quartz crystal thus is likely to have several substances deposited onto its surface, each with different acoustic impedances and densities. Although the parameters for magnesium were programmed into the TM-100, it is doubtful that an accurate value for the total thickness deposited was received. Therefore, the thickness monitor was used chiefly to monitor relative rates of evaporation, along with the vacuum gauge.

The desired thickness of magnesium for targets is 1 $\mu g/cm^2$ for low energies and 3 $\mu g/cm^2$ for higher energies. A thinner target is desired for lower energies, in order to keep the background noise in the spectrum to a minimum and to reduce the energy loss as the beam passes through the target. At higher energies, Rutherford

scattering does not pose as much of a problem, and targets can be thicker in order to provide higher count rates.

Gold is often evaporated onto the carbon foil backings prior to evaporation of the element to be used for the experiment. This is done to prevent the element of interest from reacting with the carbon or migrating into the foil, which would increase the energy spread of the beam as it travels through the carbon before striking the element of interest. In addition, the gold is often used to monitor the target for tears or breaks, which are reflected as sudden changes in the yield curve, and to normalize the detectors, since the gold exhibits pure Coulomb scattering at energies of a few MeV. In this case there seemed to be little need for using gold to separate the magnesium from the carbon foils, and the tantalum on the targets was sufficient for monitoring the targets.

Gold and other elements also have been used to promote the element of interest sticking to the carbon foils during evaporation. One of the main difficulties with producing magnesium targets of sufficient thickness is that the evaporated magnesium adheres poorly to the carbon foils. Over the years, a number of people have attempted to produce thin-film magnesium targets at TUNL, and have tried various elements as a coating for the carbon foils. Gold produced poorer results than the carbon foils alone. Other elements that have been tried are silver, copper, aluminum, and bismuth. However, for the targets described here it was found that the problem of the magnesium adhering to the carbon foils could be solved satisfactorily by carefully monitoring the evaporation process and by placing the foils close to the tantalum boat. Then one could avoid adding another element to the targets, which would increase the thickness and degrade the resolution of the targets. The following is a detailed description of the process used to produce the thin-film magnesium targets.

The first method of evaporation attempted used tantalum as a reducing agent:

$$5\ MgO + 2\ Ta \longrightarrow Ta_2O_5 + 5\ Mg.$$

Equal volumes of magnesium oxide powder and tantalum powder were combined with enough distilled water to form a good paste. This paste was used to coat the dimple of an open tantalum boat, S2A-.005TA, from R.D. Mathis Company. A shutter was not used to shield the carbon foils for this initial evaporation. Glass slides were placed on top of the carbon foils during evaporation in order to prevent a deposit on the back of the targets during evaporation.

When these targets were tested in the beam for decay, contamination, and thickness, no decay was observed with approximately 1.8 μA of beam on target. However, these targets had only ~0.2 $\mu g/cm^2$ of magnesium, which was not thick enough, and had too much tantalum, ~12 $\mu g/cm^2$. There were also several contaminants on these targets. Possible sources for the contamination included old magnesium oxide powder and unclean "distilled" water.

The same general technique was then tried with a newer source of magnesium oxide powder. This time the boat was outgassed prior to the evaporation. Also, instead of mixing the MgO-Ta powder mixture in a mortar and pestle with distilled water, a small amount of tantalum powder was placed directly into the new tantalum boat. Then a small amount (in a 2:1 ratio with the tantalum powder) of magnesium oxide powder was placed into the boat, and the mixture was carefully stirred. This procedure eliminated contamination from the mortar and pestle and the distilled water. Once again, no decay was observed. These targets were thicker- 2-4 $\mu g/cm^2$ of magnesium. Shorter evaporation times were also investigated, in order to decrease the chances of the boat becoming too hot and developing hot spots in the powder, which might cause tantalum or magnesium oxide to evaporate.

It has been reported (Heagney, 1972) that a useful evaporating technique is increasing the vapor pressure of materials such as zinc, cadmium, magnesium, and calcium, which do not readily condense on a substrate. In an attempt to insure the magnesium oxide was reduced before evaporation occurred, and possibly increase the vapor pressure of the magnesium, a closed boat was tried next. Equal volumes of tantalum and magnesium oxide powder were placed on a piece of wax weighing paper which was folded to mix the powder together. The carbon foils were moved closer to the boat, and a shutter was used. This procedure proved to be the most reliable, and was used to produce the targets actually used in these experiments. The current was first increased slowly to approximately 100 A to bake out the powder mixture with the shutter closed. The current was then reduced until the vacuum returned to ~1 μTorr. The current was then increased slowly to 200 A. The shutter remained closed until evaporation actually began to occur, then it was opened and left open during the entire evaporation. The evaporation was halted by turning the current off and leaving the shutter open. The current was only left on for 10 minutes or less at a time, in order to prevent hot spots from developing in the powder, which might have become sufficiently hot to melt the tantalum or the magnesium oxide instead of only the reduced magnesium. Short evaporation times have also been described as a method of reducing the amount of oxygen contamination on magnesium targets. The temperature of the mixture in the boat was estimated at 1700° to 1850° C with an optical pyrometer. During evaporation, the vacuum would typically increase to 30 to 40 μTorr and remain steady until the current was decreased.

This technique proved to produce the most consistently acceptable targets. The magnesium seemed to stick to the carbon foils more with this technique than with any other. The oxygen contamination was not large enough to provide problems, and the

resolution was acceptable. The thicknesses of the targets used for this experiment were:

$$1.05 - 1.72 \ \mu g/cm^2 \quad Mg$$
$$0.03 - 0.21 \ \mu g/cm^2 \quad Ta$$
$$2.61 - 3.95 \ \mu g/cm^2 \quad O_2$$

Very little decay of the magnesium targets was observed.

The targets were stored in a desiccator when not in use. Targets were transported from the evaporator room to the laboratory enclosed in a nitrogen-filled plastic bag. When loading the targets onto the target rod and into the target chamber, a reasonable amount of caution was practiced, but oxygen contamination did not appear to be much of a problem. It is believed that for such thin films any oxidation would occur almost instantaneously, and the amount of caution observed in transporting the targets seemed unrelated to the amount of oxygen on the targets. A typical spectrum is shown in figure 3.5.

H. Experimental Resolution

Several factors determine the resolution of the data taken in these experiments. The energy of the incident beam has fluctuations due to irregularities in the charging belt, inherent energy spread and instability in the RF source and gas bottle, electronic breakdown along the beam tube or column, etc. The feedback systems also affect the beam energy resolution. The observed resolution is affected by Doppler broadening of the incident beam, the thickness and uniformity of the target, and the presence of

Figure 3.5 Typical charged particle spectrum from the 165° detector. The carbon peak has been electronically gated out in order to decrease dead times. The first inelastically scattered proton peak is covered by the low-energy shoulder of the carbon peak, but the second and third inelastically scattered proton peaks are clearly distinguishable in this spectrum. In addition to scattering from magnesium nuclei, elastically scattered protons corresponding to oxygen and tantalum contaminants were observed.

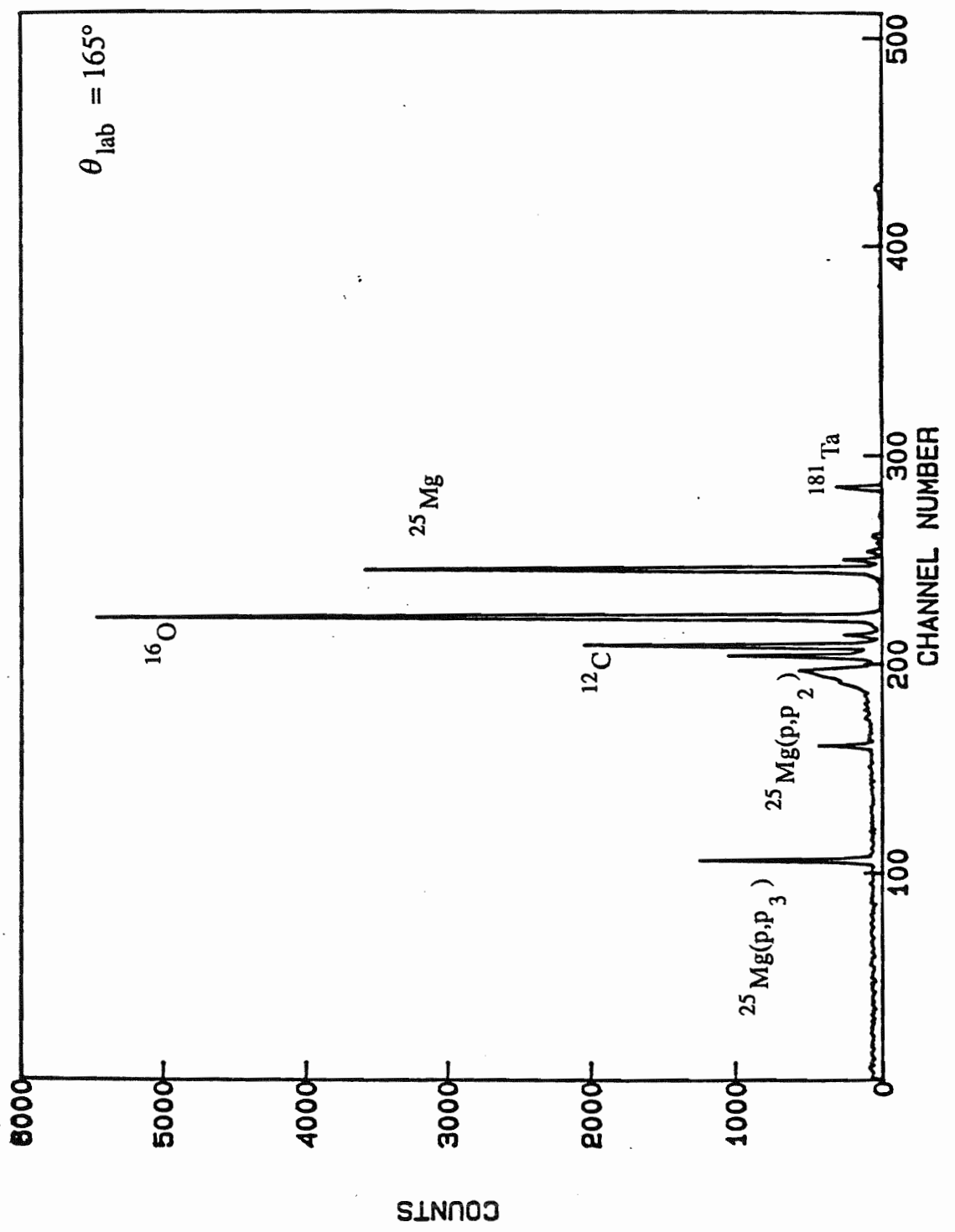
$\theta_{lab} = 165°$
^{16}O
^{25}Mg
^{181}Ta
^{12}C
$^{25}Mg(p,p_2)$
$^{25}Mg(p,p_3)$
COUNTS
CHANNEL NUMBER
0
1000
2000
3000
4000
5000
6000
100
200
300
400
500

contaminants on the target. The size of the beam spot on the target and movement of the beam spot will also affect the observed resolution.

The energy resolution of these data was determined by fitting small isolated resonances, for example, two d-wave resonances observed by Adams at E_p = 1.1640 MeV and 1.9569 MeV (Adams, 1983). The resolution was determined to be approximately 400 eV. Energy calibration was performed using a secondary standard resonance in $^{44}Ca(p,p_0)$. The process of energy calibration and data normalization is described in more detail in the next chapter.

I. Experimental Procedure

In order to obtain the best possible resolution, significant time was spent tuning the machine. It is desired to achieve a stable beam current with a small beam spot that does not move on the target. This is usually accomplished by first tuning the beam through the analyzer, using the focus electrode and the X-Y electrostatic steerer located in front of the analyzing magnet. After current is centered in the analyzer, the tuning ring is put in the beam line in the target chamber. The tuning ring is positioned at 0° to the line of the beam (with the plane of the ring perpendicular to the beam line). Using the two sets of L-R-U-D steering magnets and the quadrupole magnetic lens, the current striking the tuning ring is minimized while the current passing through the hole in the center of the ring is maximized.

Changing targets is fairly easy. Up to four targets and a tuning ring can be mounted on a vertical target rod in the center of the target chamber. This rod can be raised and lowered relative to the target chamber without opening the chamber, thus changing the target that is in the line of the beam.

A spectrum consists of 512 channels corresponding to energies of detected particles. There are five spectra in this experiment, one for each detector. The peaks in the spectra correspond to elastic or inelastic scattering of protons from different elements in the target.

A yield curve, or excitation function, is generated by summing under the peaks of interest in the spectrum and possibly performing a background subtraction, multiplying by the dead time correction factor, and storing this value in the channel corresponding to that beam energy in the yield curve. Then the beam energy is incremented, another spectrum is obtained, the summation process is repeated, and another point in the yield curve is obtained. The standard time for each yield curve point to be obtained (the time for a "run") is typically one to two minutes.

When the preset value for the beam current integrator (BCI) is reached, the data acquisition is halted by the CAMAC crate. This signals the end of one "run" of data acquisition taken at one beam energy. The analyzer plate voltage is then increased by the amount necessary to increment the beam energy for the next "run". The spectra and scalers are written to magnetic tape after performing any background subtraction and dead time calculations and corrections. The yield curves are generated by summing under the peaks of interest, subtracting background, and multiplying by the dead time correction factor. The windows on the peaks of interest are shifted if this becomes necessary after incrementing the beam energy. All spectra and scalers are cleared, and data acquisition is then resumed for the next "run". This is all performed automatically, using hibernating subprocesses on the VAX 11/750.

These data were taken in the energy range from E_p = 1.95 MeV to 3.40 MeV. The energy step size was typically 100 to 400 eV, with the larger steps only taken

between resonances. There was usually ~2-4 μA on target, with ~20-40 nA on the tuning ring and ~300 nA in the electrostatic analyzer. Data were accepted only when the incident beam energy was within 10 eV of the desired beam energy.

CHAPTER IV

DATA REDUCTION AND RESONANCE ANALYSIS

A. Preparation of Data

1. Data Handling Programs

The spectra acquired in these experiments were processed using the data acquisition and analysis software package XSYS. The Fortran program XSTRIP was written by Warthen (1987) and was used for offline data analysis. XSTRIP generates yield curves from data stored on magnetic tape, calibrates the spectra, and performs dead time corrections. The option of performing a linear, polynomial, or no background subtraction is provided. Using the calibration parameters, the program determines where the peaks of interest should appear in the spectrum and defines "windows" to include the peaks. The area under the portion of the spectrum included within each window is computed. A background subtraction and dead time correction is applied to this sum, and the resultant number is plotted versus the energy of the incident proton beam. The plot of the sum of a window as a function of incident proton energy is then called the yield curve or excitation function.

The XSYS program XCALIB was used to shift the windows of the peaks of interest as the incident proton energy was incremented, so that the windows remained centered on the peaks of interest. The program calculates the energy of each calibration peak, performs a linear least squares fit of the calculated energies to the

channel numbers of the highest points for each peak, and then calculates the positions of the peaks of interest.

2. Stripping Procedure

The data were separated into sections of similar tunings and target spots. A typical spectrum in each section was calibrated, using as calibration peaks the magnesium, oxygen, and tantalum elastic scattering peaks. Five spectra were generated, one per angle, for each incident proton energy. Only approximately 50 to 100 points were stripped at a time, in order to ensure that the windows remained centered on the peaks of interest.

A linear background subtraction was performed. Two points on each side of the window were used to determine a straight line background under the peak. Counts inside the window were summed and the background corresponding to that peak was subtracted. For elastic scattering of protons on magnesium, usually less than 2% of the total number of counts was background.

B. Offline Analysis of Data

1. MULTI6

The yield curves were fit using the Fortran program MULTI6 written by Sellin (1969) and modified by others at TUNL over the years, including Watson, Nelson, Vanhoy, Shriner, and Keeter. MULTI6 uses the *R*-Matrix theory of Lane and Thomas (1958) to calculate theoretical elastic and nonelastic differential cross sections for the

multilevel, multichannel case. MULTI6 then normalizes the data to the fit by comparing the area under the theoretical cross section to the area under the data curve for the energy region of interest.

The program has been modified over the years to enlarge the number of resonances, channels, and J^{π}'s that could be handled. MULTI6 can currently handle up to 1000 data points, 1000 calculated fit points, 300 levels, 14 J^{π} values, 5 reaction channels, and orbital angular momentum values up to $l = 5$. For this analysis, the program was modified to include up to 14 J^{π} values.

The input for the analysis program includes the masses of the projectile and the target, the reaction Q-values, the allowed channel spin and orbital angular momentum values and the possible values of J^{π}. These parameters are used to determine the allowed entrance and exit channels.

Also input to the program are the laboratory angles at which scattered particles were detected, the boundary condition value, and the nucleon unit radius. The boundary condition value may be set equal to the shift function either for each resonance or at the center of the data section. For this analysis the boundary condition was set equal to the shift function for each resonance. The nucleon unit radius was chosen to be 1.25 F for consistency with other data from this research program.

The variables in the program are the energies of the resonances, the specific exit channel for each resonance (including the J^{π}, channel spin, and orbital angular momentum values), the partial width for each exit channel, and the signs of the reduced width amplitudes. These variables are adjusted to produce a visual fit to the data.

The calculations performed by MULTI6 include Coulomb, "hard sphere", and resonance scattering. The output is a theoretical excitation function based on the input resonance parameters.

2. Resolution Width Determination

A resolution function is calculated by the subroutine SMEAR in order to simulate the finite resolution of the system plus straggling effects in the target. A Gaussian function with a Lorentzian leading edge reproduced the actual laboratory effects well. This function was specified by a Gaussian FWHM and the ratio of the Lorentzian FWHM to the Gaussian width. These quantities were determined by fitting a narrow resonance. It was found that these numbers were fairly constant even for different targets and tunings of the beam.

3. Energy Calibration

Both primary and secondary standards have been used to calibrate the beam energy of the accelerator. The primary standards used are the neutron thresholds ^{7}Li(p,n) at E_p = 1.8806 MeV and ^{13}C(p,n) at E_p = 3.2375 MeV (Marion, 1966). Secondary standards commonly used include the ^{44}Ca(p,p_0) s-wave resonance at E_p = 1.8840 Mev and the ^{29}Si(p,p_0) f-wave resonance at E_p = 1.7715 MeV, and another ^{29}Si(p,p_0) f-wave resonance at E_p = 3.2451 MeV. During the course of these experiments, the ^{44}Ca(p,p_0) s-wave resonance at E_p = 1.8840 MeV was measured along with known resonances in the ^{27}Al(p,p_0) cross section for calibration purposes.

C. Fitting Procedure

The fitting process is largely trial and error. It consists of visually determining the energies of resonances in a given section of data and making an educated guess

about the spins, parities, and widths of the resonances. These assumptions are used by MULTI6 to produce a theoretical fit to the data which is then viewed and compared. Changes are then made as seem appropriate, for example, increasing the width of a resonance or changing the spin. Catalogs of resonances which detail channel spin mixing, orbital angular momentum mixing, etc., prove very useful. Often it is easy to choose the correct J^{π} value, so only certain channels need to be tried. Also, some small number of generalizations can be made. Usually the large, obvious, isolated, or previously known resonances are the first to be included in a given section of data. Next, the smaller resonances, and those that are closer together, are included. This can prove very difficult, as resonances may interfere with each other. Hence, after achieving a fairly good fit with one resonance, or section, the fit can be completely altered when a neighboring resonance is added.

The value for the orbital angular momentum and thus the parity is usually obvious from the resonance shape. Resonances with even parity usually exhibit a dip in the yield function at 90°, while odd parity resonances are evidenced by a bump at 90°. By comparing the yield curves from the detectors at 90° and 165°, an l-value is assigned to the resonance. Once a value for the orbital angular momentum has been determined, the total spin of the resonance can usually be determined by examining the shape of the resonance, especially at back angles. For example, the height of the peak of a d-wave (l = 2) resonance increases drastically with increasing spin values, especially at 165°. Examining the yield curves at 90° and 165° is often sufficient for assigning values for the parity, orbital angular momentum, and total spin. Other angles may be useful in analyzing regions of data which prove more complicated. The channel spin is limited to two allowed values for each reaction pair, for example, s = 2 and s = 3 for elastic scattering, and sometimes only one of these values is allowed for

the given spin and total angular momentum.

Since the target has a ground state spin of 5/2 in this experiment, both l-mixing and s-mixing are allowed for a large number of possible J^{π} values. This greatly complicates the data fitting procedure. Often unique values for the laboratory widths of all the allowed channels cannot be determined. This is especially true for channel spin mixing, in which case the effect of adding an $s = 3$ channel can be duplicated by increasing the laboratory width of an $s = 2$ channel. In addition, for some cases of l-mixing, almost identical results can be produced by two different ratios of orbital angular momentum widths. Both kinds of mixing are discussed in greater detail later in this chapter.

D. Catalog of States and Interference Effects

1. Allowed channels

For targets with non-zero intrinsic spin, most excited states can be formed in more than one way. In the resonance reaction model used here, this is exhibited by the existence of several exit channels for the compound nucleus. Table 4.1 lists the J^{π} values that can be formed from various l, s combinations for each particle pair. Values are given for the case of elastic scattering of protons with the target nucleus of ^{25}Mg, and for protons that are inelastically scattered from the first three excited states of the compound nucleus. No reactions involving (p,α) were expected to be observed at these energies.

Table 4.1

Allowed entrance and exit channels for resonances in ^{26}Al.

	p_0		p_1		p_2		p_3	
l	s=2	s=3	s'= 0	s'=1	s'=1	s'=2	s'=3	s'=4
0	2^+	3^+	0^+	1^+	1^+	2^+	3^+	4^+
1	1^-	2^-	1^-	0^-	0^-	1^-	2^-	3^-
	2^-	3^-		1^-	1^-	2^-	3^-	4^-
	3^-	4^-		2^-	2^-	3^-	4^-	5^-
2	0^+	1^+	2^+	1^+	1^+	0^+	1^+	2^+
	1^+	2^+		2^+	2^+	1^+	2^+	3^+
	2^+	3^+		3^+	3^+	2^+	3^+	4^+
	3^+	4^+				3^+	4^+	5^+
	4^+	5^+				4^+	5^+	6^+
3	1^-	0^-	3^-	2^-	2^-	1^-	0^-	1^-
	2^-	1^-		3^-	3^-	2^-	1^-	2^-
	3^-	2^-		4^-	4^-	3^-	2^-	3^-
	4^-	3^-				4^-	3^-	4^-
	5^-	4^-				5^-	4^-	5^-
		5^-					5^-	6^-
		6^-					6^-	7^-

2. Penetrabilities

Penetrability plots for the elastic and inelastic proton scattering channels are shown in figures 4.1 and 4.2. The lowest energy at which protons inelastically scattered to the first excited state of ^{25}Mg are observed is at E_p = 1.284 MeV. The Q-value for this reaction is 0.5852 MeV. The Q-value for the reaction ^{25}Mg(p,p$_2$) is 0.9747 MeV, and the inelastically scattered protons to this state first appear at E_p = 1.899 MeV. The Q-value for the reaction ^{25}Mg(p,p$_3$) is 1.6140 MeV, and protons for this state are first observed at E_p = 1.899 MeV.

3. Proton Resonance Catalog

The effect of the orbital angular momentum value on the shape of the resonance is illustrated by figures 4.3 and 4.4. Figure 4.3 shows theoretical cross sections generated by the program MULTI6 for the reaction ^{25}Mg(p,p$_0$) with exit channels corresponding to $J = 2$ and $s = 2$. The cross sections are calculated for resonances at E_p = 3.00 MeV with a laboratory width Γ_p = 2.00 keV. Figure 4.4 shows theoretical cross sections corresponding to $J = 3$ and $s = 3$. Comparing the cross sections at detector angles of 90° and 165° yields the most information. Although the height of the resonance is increased from $J = 2$, $s = 2$ to $J = 3$, $s = 3$, the general shape of the resonance is relatively unchanged.

Figures 4.5 and 4.6 show how an s-wave ($l = 0$) resonance varies with different values of J^π. Figure 4.5 shows $J^\pi = 2^+$ and 3^+ resonances at five angles. The higher J value causes an increase in the slope and the height of the resonance. The behavior at 135° and 150° is similar to that at 165°. The most pronounced difference is at 90° and

Figure 4.1 Coulomb penetrabilities versus energy for the $^{25}Mg(p,p_0)$ and $^{25}Mg(p,p_1)$ reactions. The horizontal axis is the laboratory energy of the incident proton. The different curves correspond to different values of orbital angular momentum.

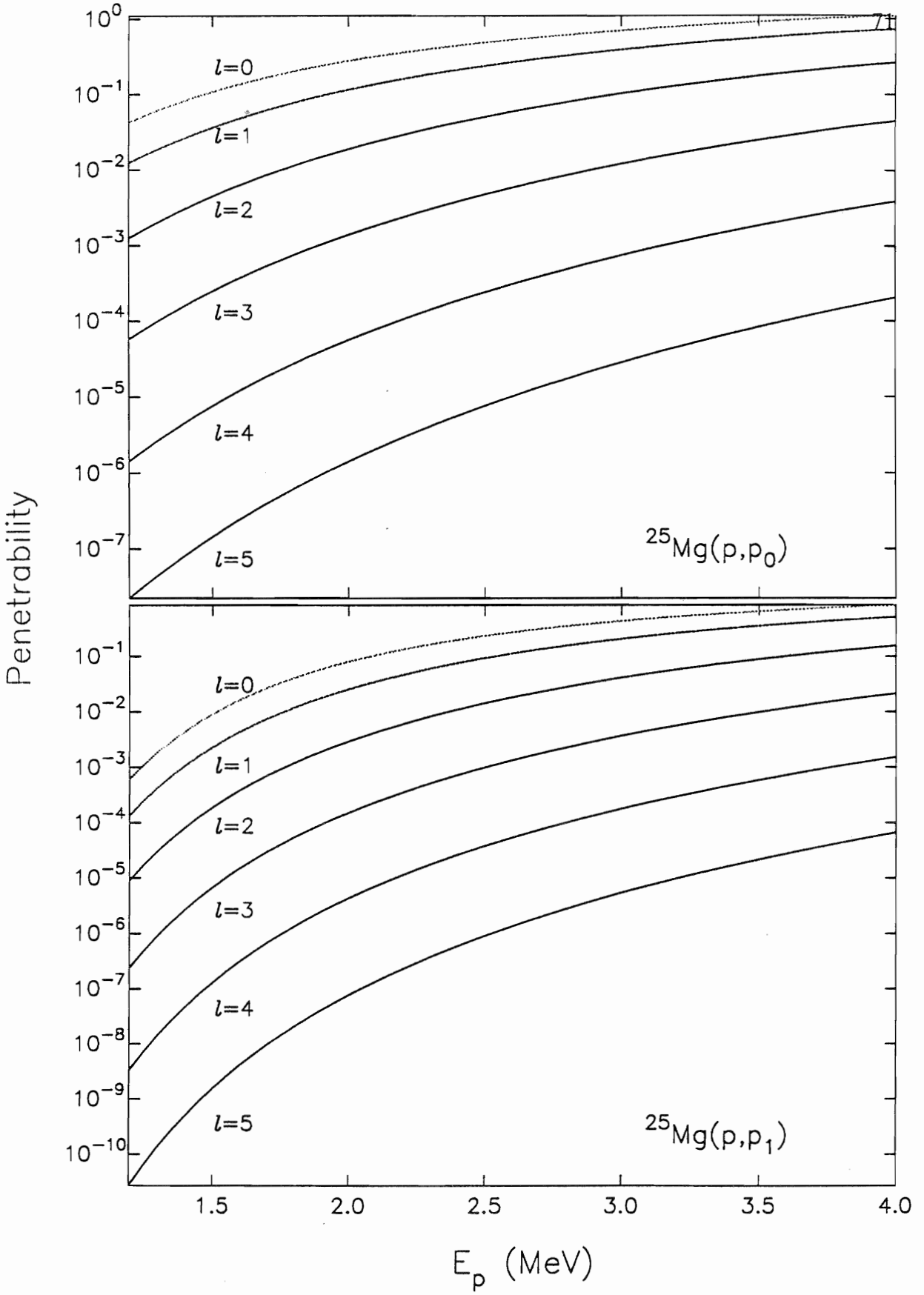
Penetrability
10^{0}
10^{-1}
10^{-2}
10^{-3}
10^{-4}
10^{-5}
10^{-6}
10^{-7}
l=0
l=1
l=2
l=3
l=4
l=5
^{25}Mg(p,p$_0$)
10^{-1}
10^{-2}
10^{-3}
10^{-4}
10^{-5}
10^{-6}
10^{-7}
10^{-8}
10^{-9}
10^{-10}
l=0
l=1
l=2
l=3
l=4
l=5
^{25}Mg(p,p$_1$)
1.5
2.0
2.5
3.0
3.5
4.0
E_p (MeV)

Figure 4.2 Coulomb penetrabilities versus energy for the $^{25}Mg(p,p_2)$ and $^{25}Mg(p,p_3)$ reactions. The horizontal axis is the laboratory energy of the incident proton. The different curves correspond to different values of orbital angular momentum.

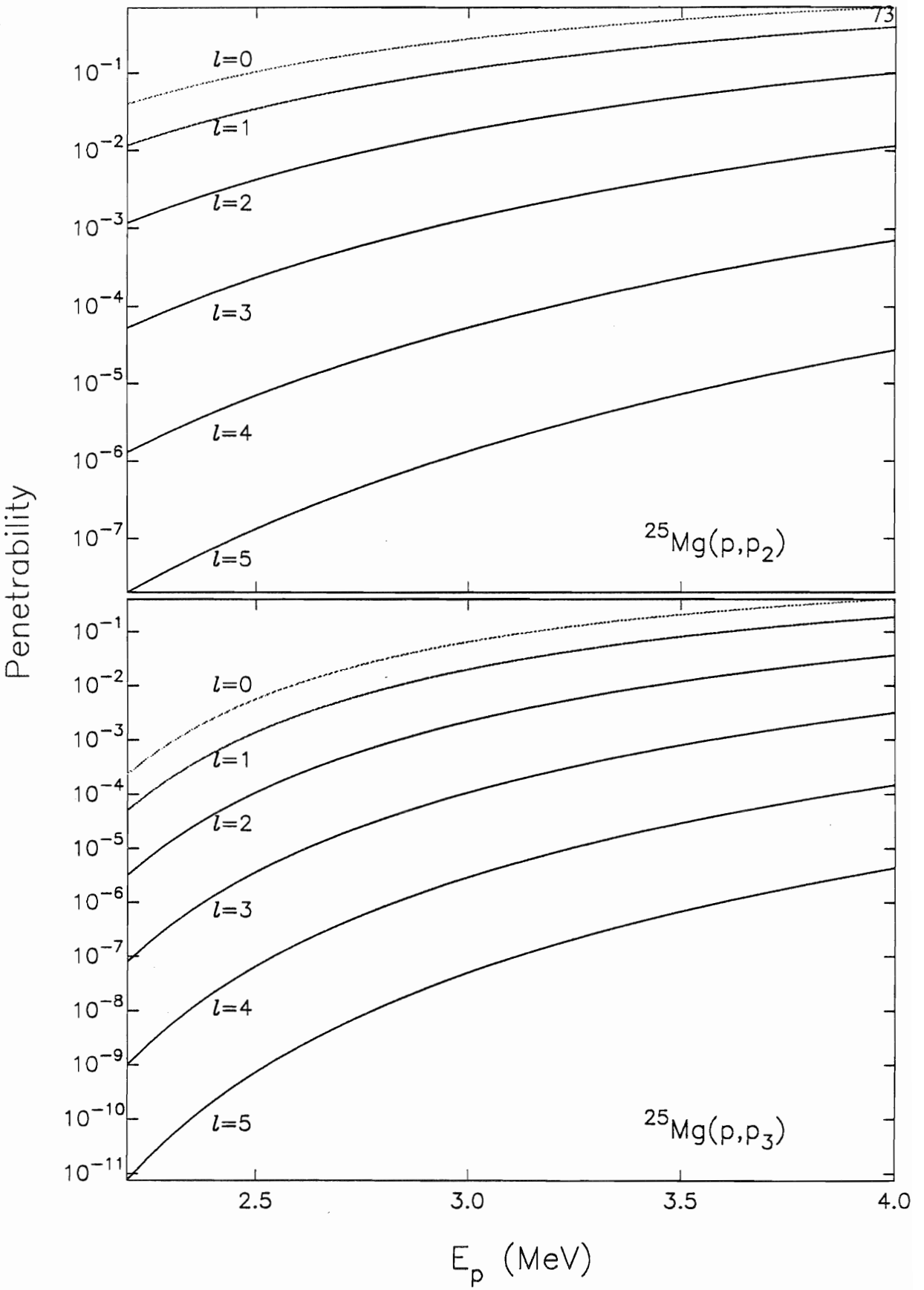
Penetrability
10^{-1}
10^{-2}
10^{-3}
10^{-4}
10^{-5}
10^{-6}
10^{-7}
l=0
l=1
l=2
l=3
l=4
l=5
^{25}Mg(p,p$_2$)
10^{-1}
10^{-2}
10^{-3}
10^{-4}
10^{-5}
10^{-6}
10^{-7}
10^{-8}
10^{-9}
10^{-10}
10^{-11}
l=0
l=1
l=2
l=3
l=4
l=5
^{25}Mg(p,p$_3$)
2.5
3.0
3.5
4.0
E_p (MeV)

Figure 4.3 Variation in resonance shape as a function of detector angle and orbital angular momentum value. Resonance shapes are shown for $s = 2$, $J = 2$ and $\Gamma_p = 2$ keV resonances. The orbital angular momentum is varied from $l = 0$ to $l = 3$.

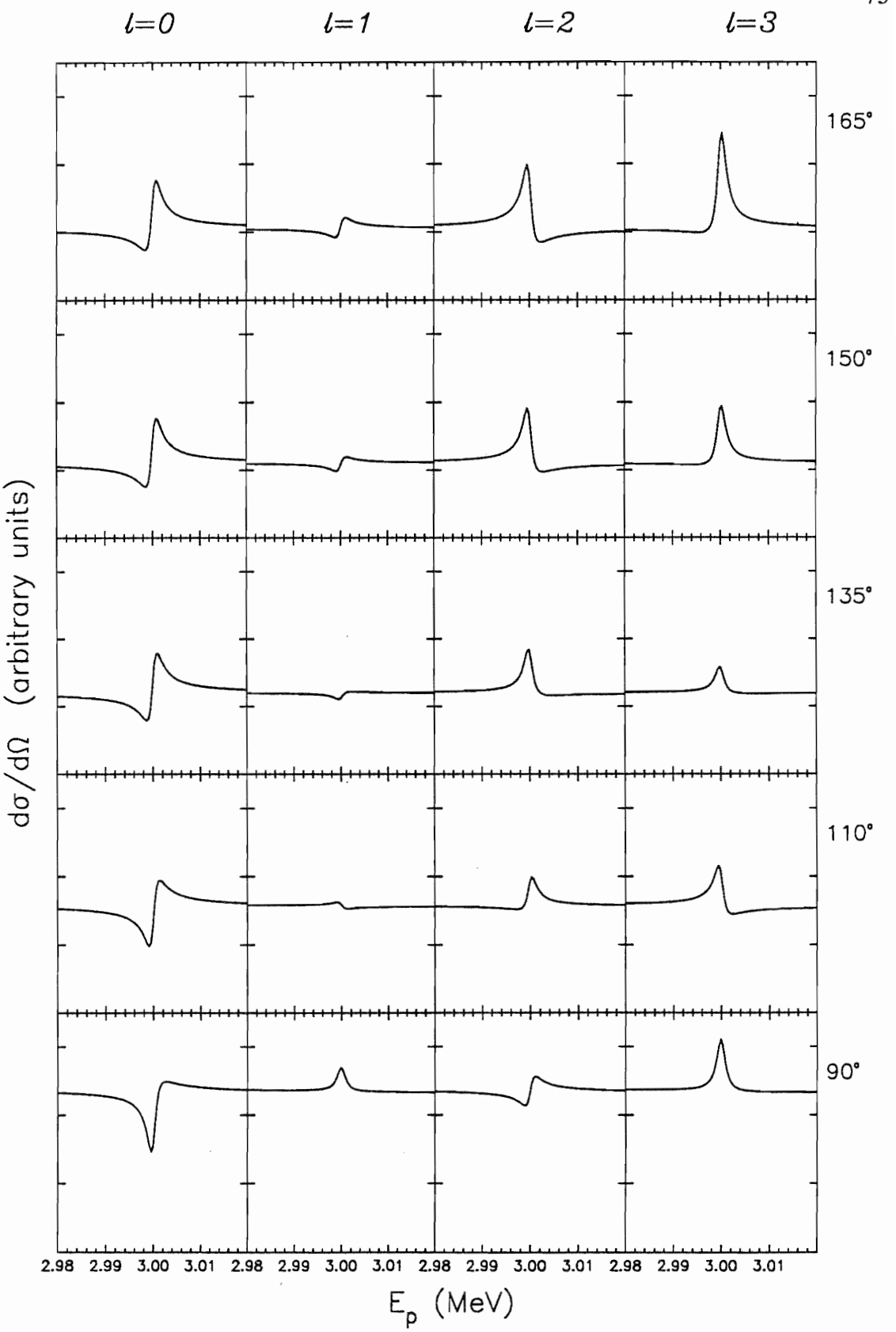
l=0
l=1
l=2
l=3
165°
150°
135°
110°
90°
dσ/dΩ (arbitrary units)
2.98 2.99 3.00 3.01 2.98 2.99 3.00 3.01 2.98 2.99 3.00 3.01 2.98 2.99 3.00 3.01
E_p (MeV)

Figure 4.4 Variation in resonance shape as a function of detector angle and orbital angular momentum value. Resonance shapes are shown for $s = 3$, $J = 3$ and $\Gamma_p = 2$ keV resonances. The orbital angular momentum is varied from $l = 0$ to $l = 3$.

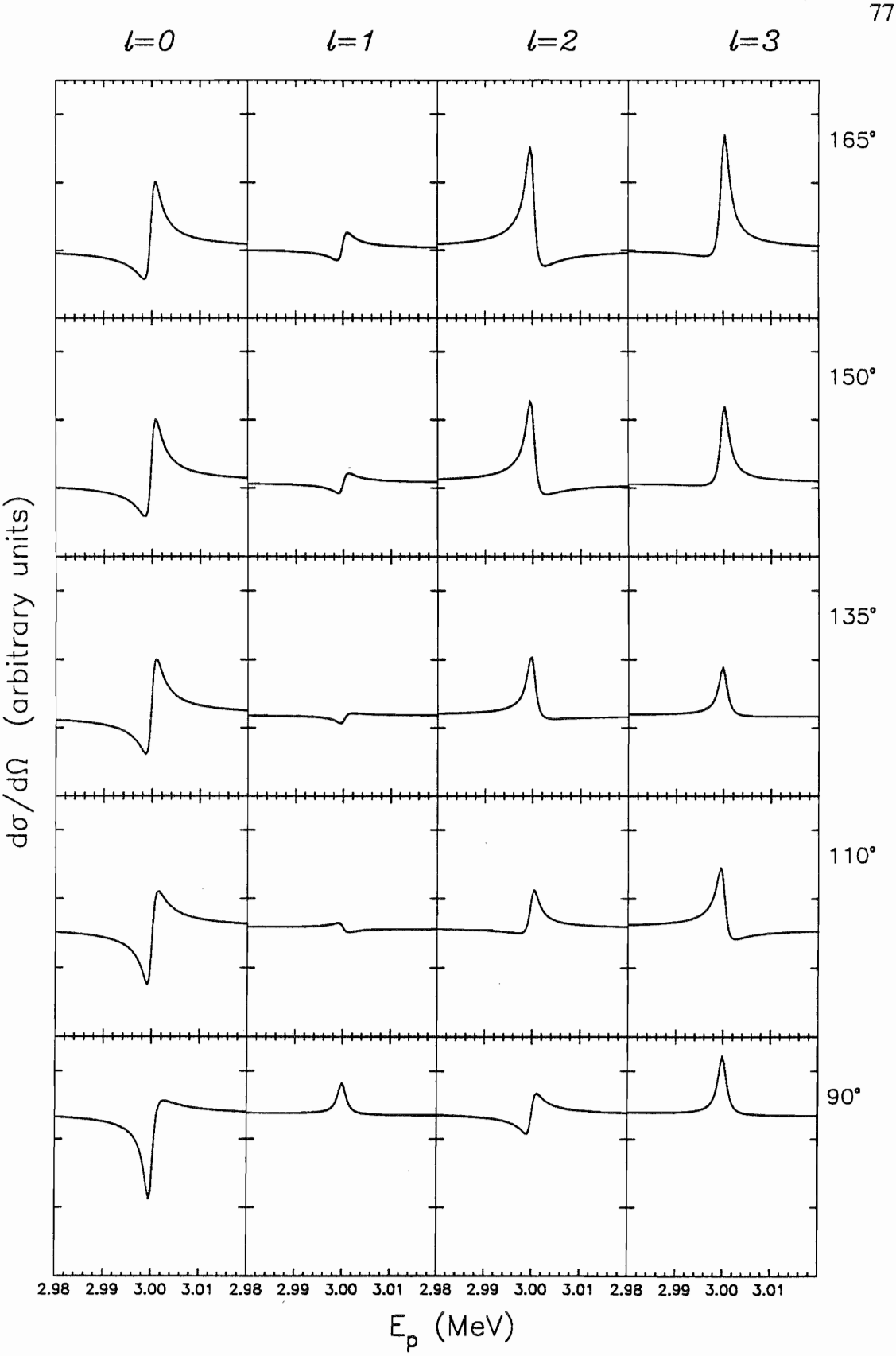
ℓ=0
ℓ=1
ℓ=2
ℓ=3
165°
150°
135°
110°
90°
dσ/dΩ (arbitrary units)
2.98 2.99 3.00 3.01 2.98 2.99 3.00 3.01 2.98 2.99 3.00 3.01 2.98 2.99 3.00 3.01
E_p (MeV)

Figure 4.5 Variation in s-wave resonance shape as a function of J. Resonance shapes for $J^{\pi} = 2^{+}$ and $J^{\pi} = 3^{+}$ are shown at 5 angles. The laboratory width is constrained such that $(2J + 1)\Gamma_{p}$ is held constant.

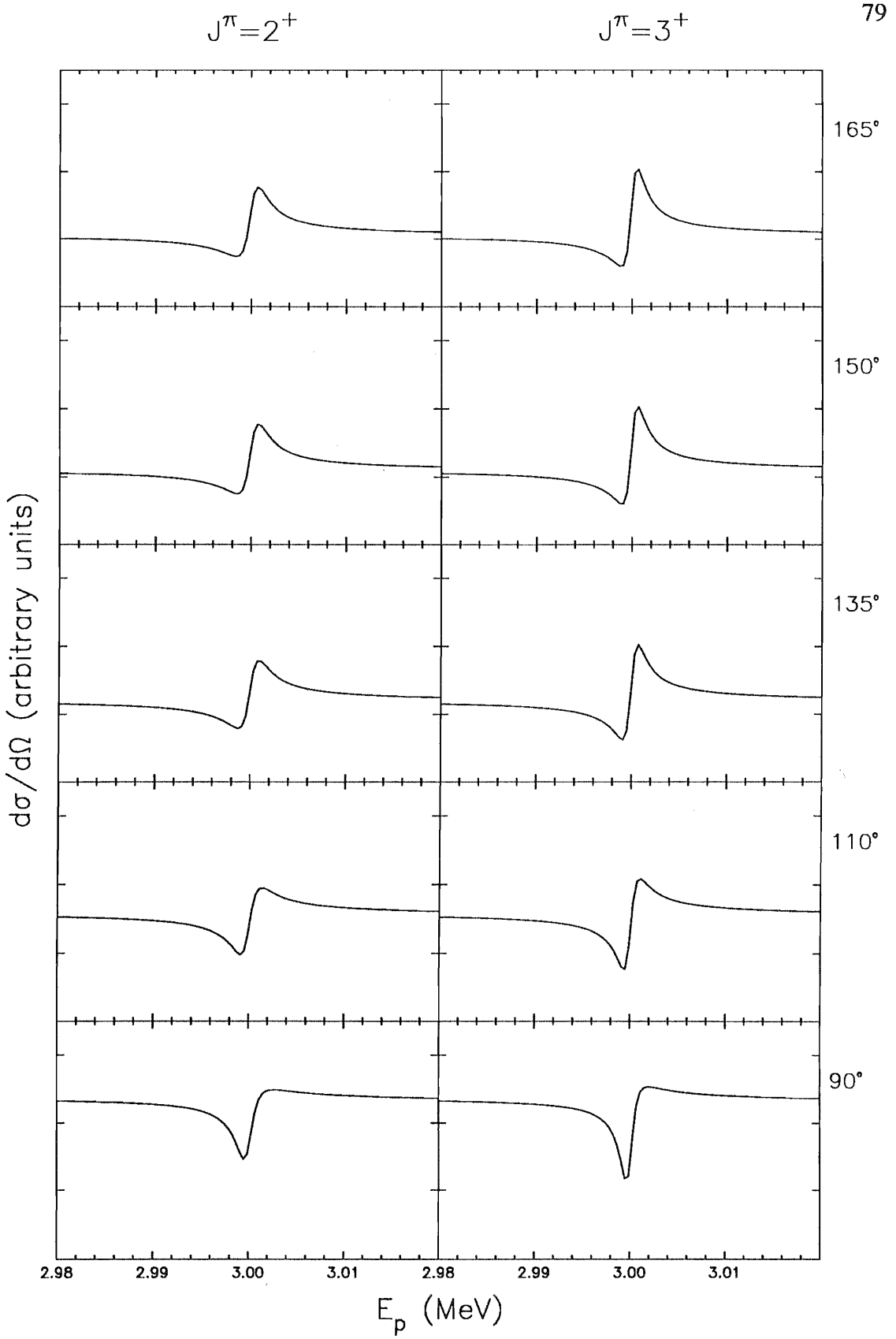
$J^{\pi}=2^{+}$
$J^{\pi}=3^{+}$
165°
150°
135°
110°
90°
dσ/dΩ (arbitrary units)
2.98
2.99
3.00
3.01
2.98
2.99
3.00
3.01
E_p (MeV)

Figure 4.6 Variation in s-wave resonance shape as a function of J. Resonance shapes for $J^{\pi} = 2^{+}$ and $J^{\pi} = 3^{+}$ are shown at 90° and 165°. The solid line corresponds to $J^{\pi} = 2^{+}$, and the dashed line represents $J^{\pi} = 3^{+}$.

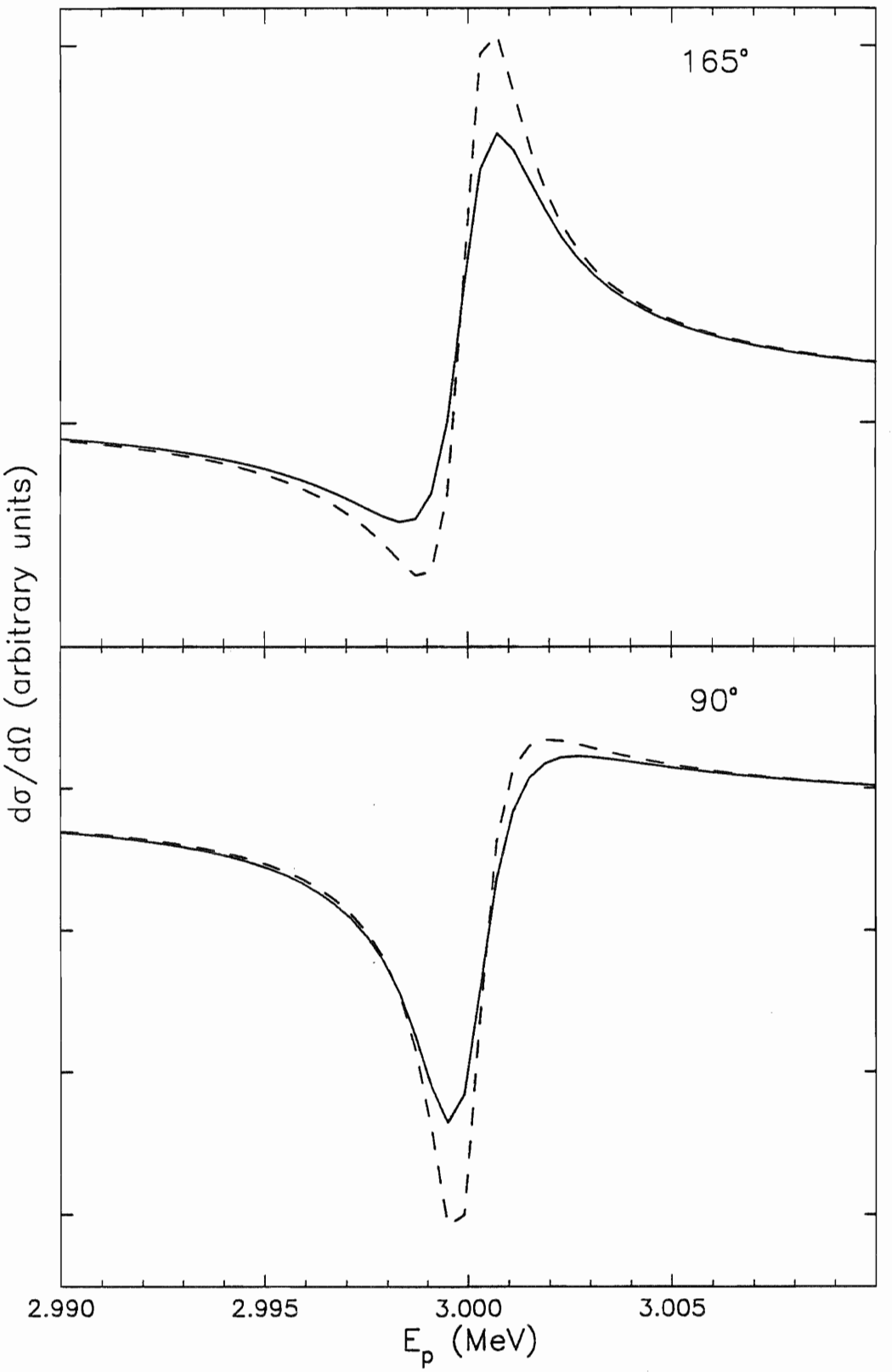
165°
90°
dσ/dΩ (arbitrary units)
2.990
2.995
3.000
3.005
E_p (MeV)

165°, and figure 4.6 shows these two angles with $J^{\pi} = 2^{+}$ and 3^{+} superimposed. Unless otherwise specified, all resonances are evaluated at $E_p = 3.00$ MeV, with the laboratory widths chosen such that $(2J + 1)\Gamma_p$ is constant, with the width corresponding to the lowest value of J set equal to 2.00 keV.

Figures 4.7 and 4.8 show how a p-wave ($l = 1$) resonance varies with different values of J^{π}. Figure 4.7 shows $J^{\pi} = 2^{-}$, 3^{-}, and 4^{-} resonances at five angles. Again, the most pronounced differences are at 90° and 165°, and figure 4.8 shows these angles with the cross sections of the different J^{π} values superimposed. At 165°, the shape of the resonance changes drastically from $J^{\pi} = 2^{-}$ to $J^{\pi} = 3^{-}$. The shape of $J^{\pi} = 4^{-}$ at 165° is then similar to the shape of $J^{\pi} = 2^{-}$, only with a steeper slope. At 90°, the height of the resonance decreases from $J^{\pi} = 2^{-}$ to $J^{\pi} = 3^{-}$, then increases for $J^{\pi} = 4^{-}$. Using these two angles would thus serve to determine uniquely the spin and parity of a p-wave resonance. Although only resonance shapes for $s = 3$ channels are shown, the behavior for $s = 2$ p-wave resonances is almost identical.

Figures 4.9 and 4.10 show how a d-wave ($l = 2$) resonance varies with different values of J^{π}. The behavior at 150° and 165° is a simple increase in height of the resonance with increasing J values, but the shape of the resonance changes dramatically at 90°. The height at 135° changes significantly from $J^{\pi} = 1^{+}$ to $J^{\pi} = 2^{+}$, and also from $J^{\pi} = 4^{+}$ to $J^{\pi} = 5^{+}$. Again, the resonances shown correspond to exit channels with $s = 3$, but $s = 2$ resonances are identical in shape with a slight decrease in height.

Figure 4.7 Variation in p-wave resonance shape as a function of J. Resonance shapes for $s = 3$, $J^{\pi} = 2^-$, 3^- and 4^- are shown at five angles, with $(2J + 1)\Gamma_p$ held constant.

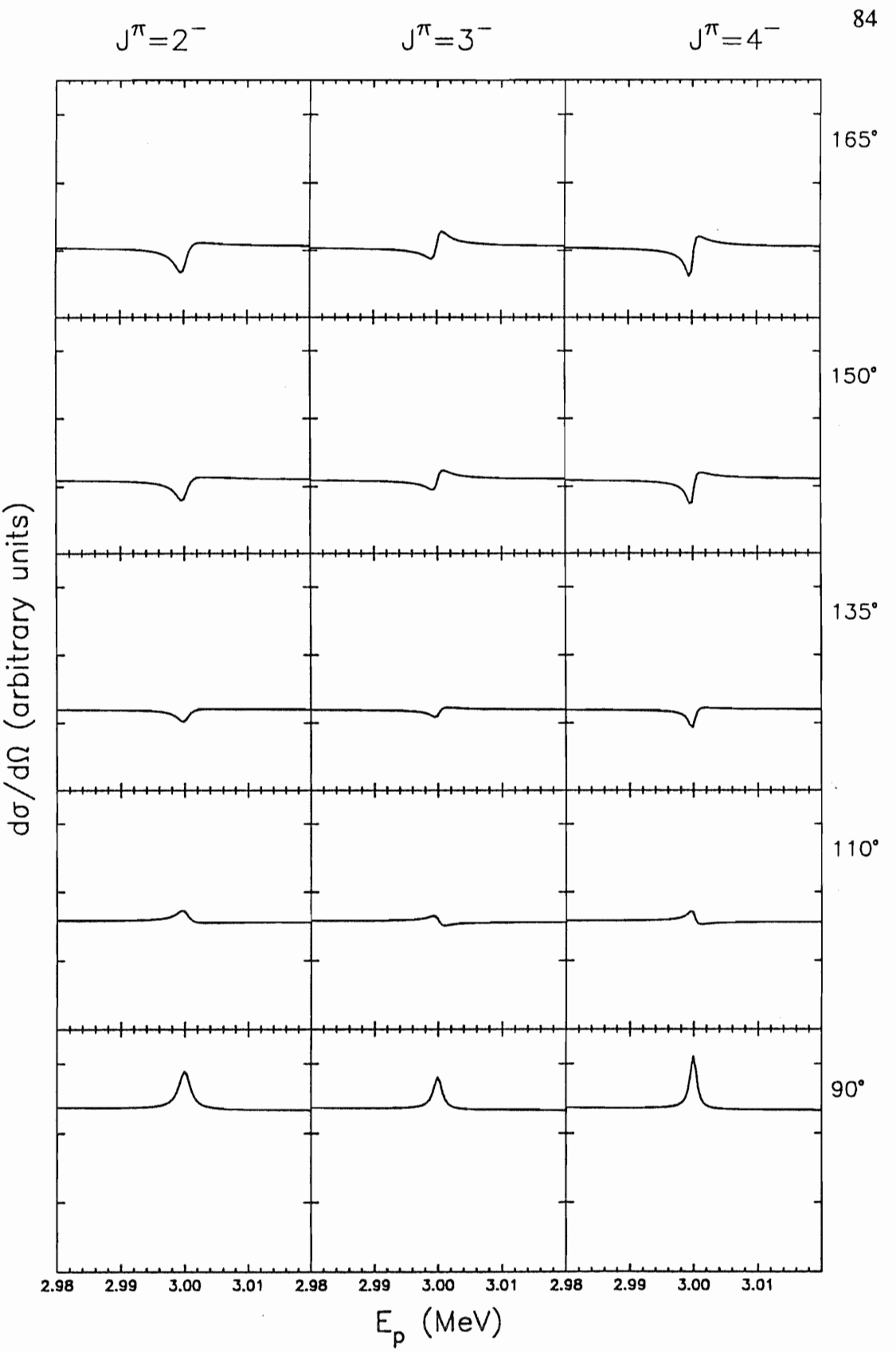
$J^\pi=2^-$
$J^\pi=3^-$
$J^\pi=4^-$
165°
150°
135°
110°
90°
dσ/dΩ (arbitrary units)
2.98
2.99
3.00
3.01
E_p (MeV)

Figure 4.8 Variation in p-wave resonance shape as a function of J. Resonance shapes for $s = 3$, $J^{\pi} = 2^{-}$, 3^{-} and 4^{-} are shown at 90° and 165°. The solid line represents $J^{\pi} = 2^{-}$, the dashed line represents $J^{\pi} = 3^{-}$, and the dot-dash line represents $J^{\pi} = 4^{-}$.

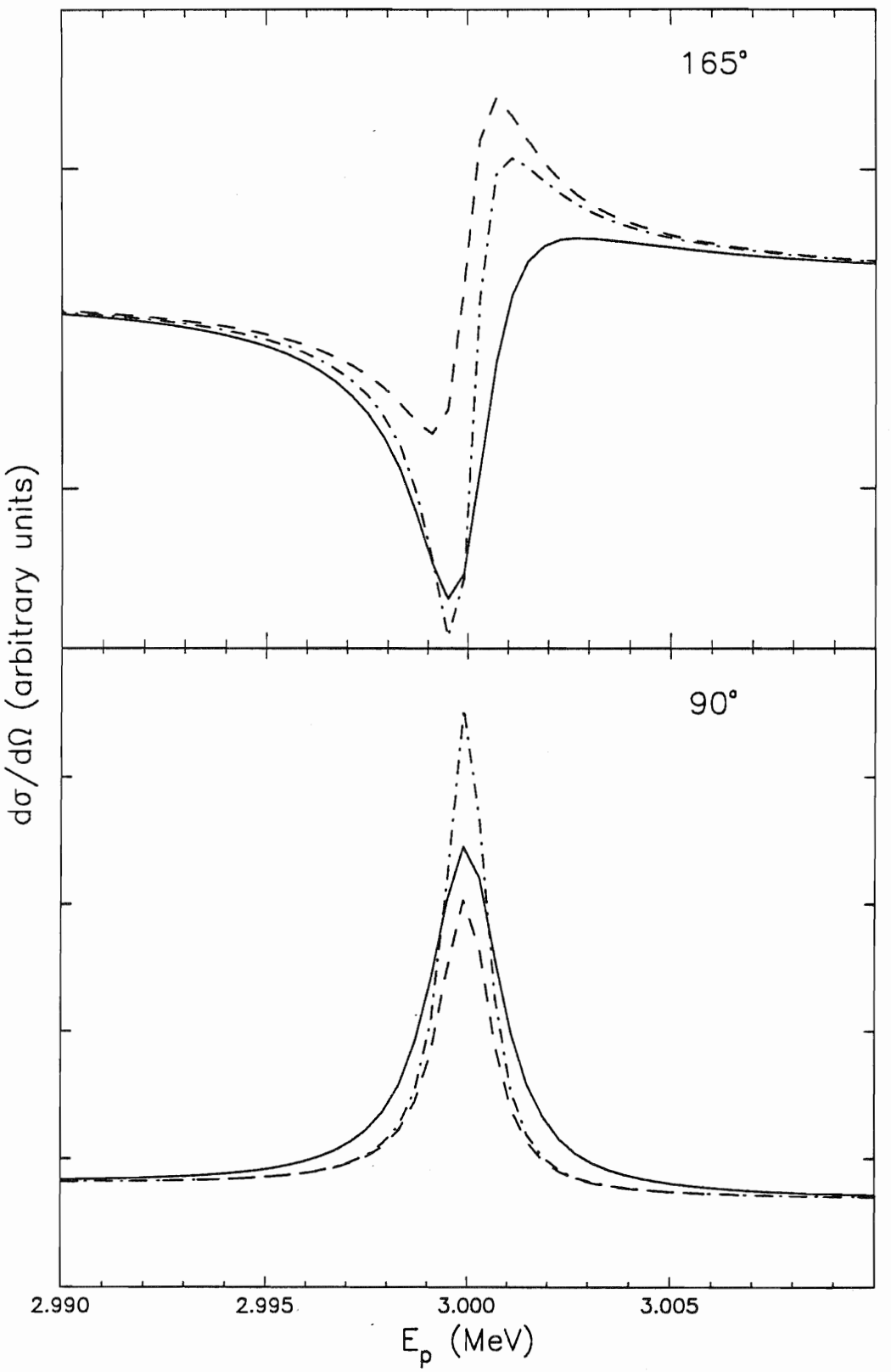
165°
90°
dσ/dΩ (arbitrary units)
2.990
2.995
3.000
3.005
E_p (MeV)

Figure 4.9 Variation in d-wave resonance shape as a function of J. Resonance shapes for $s = 3$, $J^{\pi} = 1^{+}, 2^{+}, 3^{+}, 4^{+}$ and 5^{+} are shown at five angles, with $(2J + 1)\Gamma_{p}$ held constant.

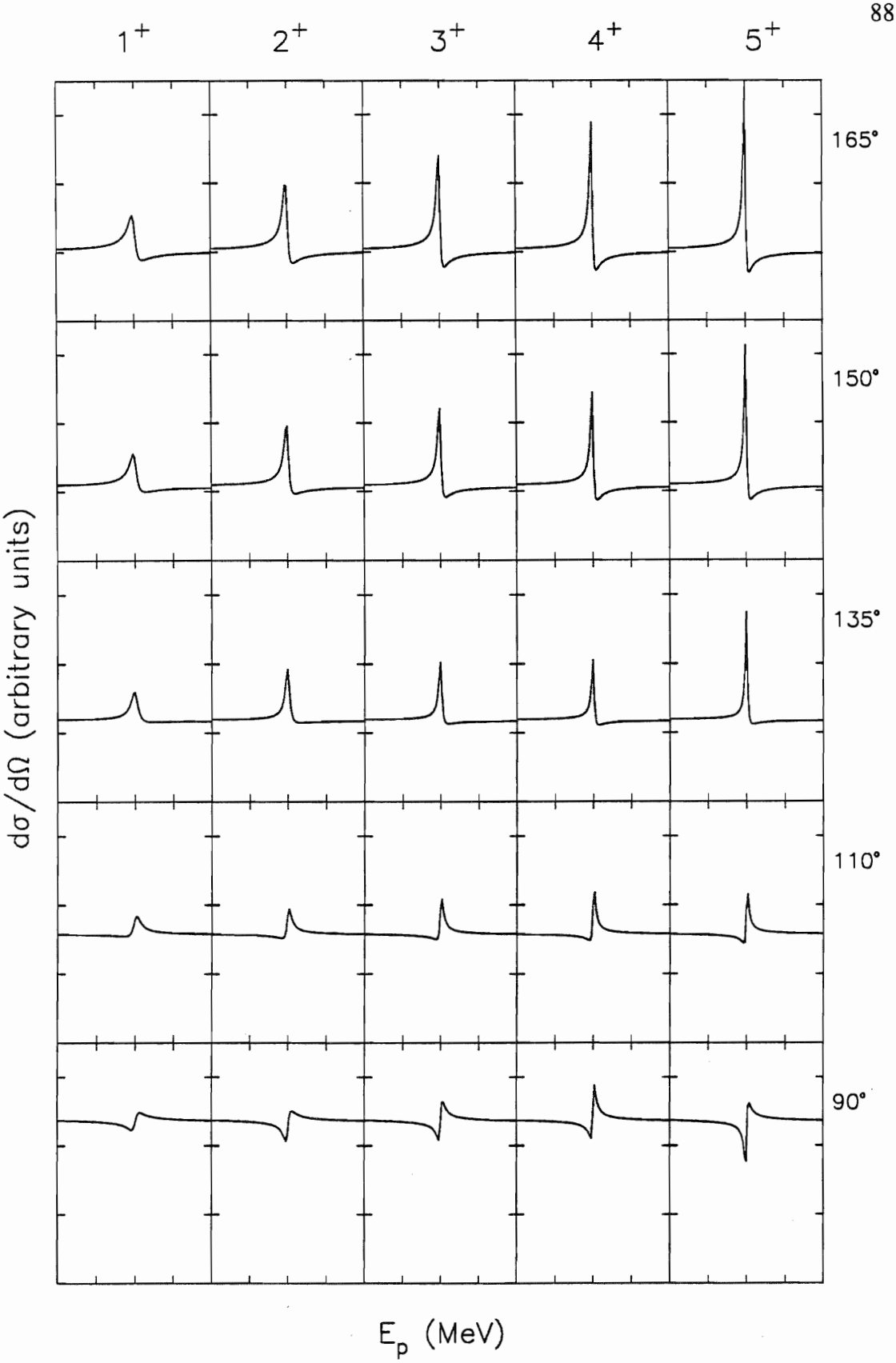
1+
2+
3+
4+
5+
165°
150°
135°
110°
90°
dσ/dΩ (arbitrary units)
Ep (MeV)

Figure 4.10 Variation in d-wave resonance shape as a function of J. Resonance shapes for $s = 3$, $J^{\pi} = 1^{+}$, 2^{+}, 3^{+}, 4^{+} and 5^{+} are shown at 90° and 165°. The solid line represents $J^{\pi} = 1^{+}$, the dashed line represents $J^{\pi} = 2^{+}$, the dot-dash line represents $J^{\pi} = 3^{+}$, the dotted line represents $J^{\pi} = 4^{+}$, and the dash-dot-dot-dot line represents $J^{\pi} = 5^{+}$.

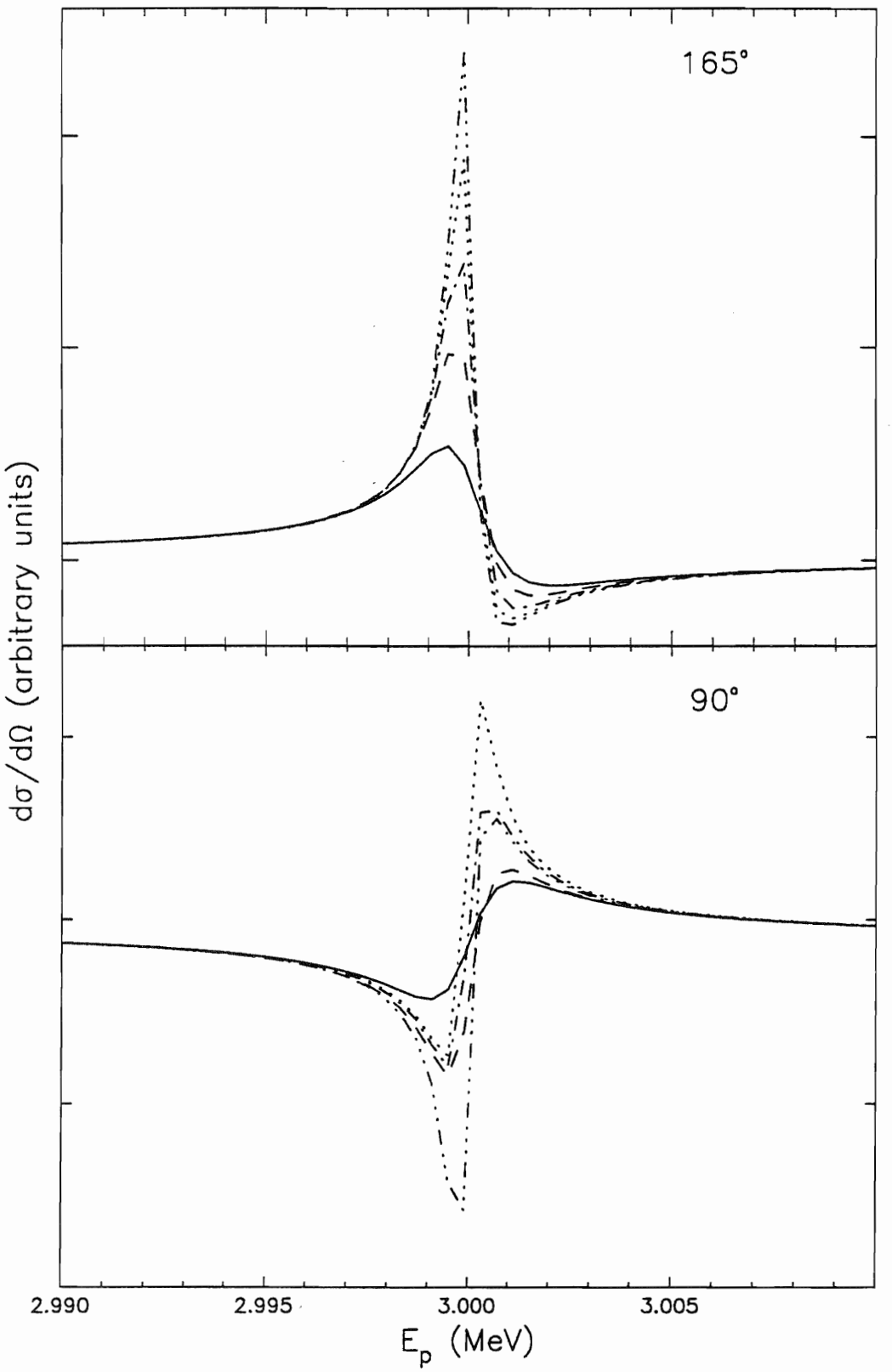
165°
90°
dσ/dΩ (arbitrary units)
2.990
2.995
3.000
3.005
E_p (MeV)

4. Channel Spin Mixing

The effects of channel spin mixing are illustrated in the next four figures. For proton elastic scattering, the allowed exit channel spins are $s = 2$ and $s = 3$, and states are allowed which contain an admixture of these channel spins. A useful parameter is the channel spin mixing ratio:

$$\xi = \frac{\Gamma_{p,s_>,l}}{\left[\Gamma_{p,s_<,l} + \Gamma_{p,s_>,l}\right]}$$

where $\Gamma_{p,s,l}$ is the laboratory width for proton scattering (elastic or inelastic) of the l^{th} partial wave with channel spin s. The lower and higher channel spins are denoted by $s_<$ and $s_>$ respectively, so that for elastic scattering, $s_< = 2$ and $s_> = 3$. Thus, ξ varies from zero for pure $s = 2$ to unity for pure $s = 3$.

Figure 4.11 shows cross sections for $J^\pi = 2^-$, $l = 1$, with the channel spin mixing ratio ξ increasing from zero to unity in increments of 0.25, at five angles. The angles of 90° and 165° are shown with the cross sections superimposed in figure 4.12. The shape of the resonance is not affected much by the value of the channel spin mixing ratio. The most noticeable effect is at 165°. Figures 4.13 and 4.14 show $J^\pi = 3^+$, $l = 2$ resonances, at five angles and then at 90° and 165° in greater detail. Notice that several values of ξ produce duplicate results. In general, channel spin mixing does not affect the shape of the resonance greatly. The most obvious effect is to change the height of the resonance. Since the height can be influenced by several different parameters, the amount of channel spin mixing cannot always be determined uniquely.

Figure 4.11 Variation of resonance shape with channel spin admixture for a $J^{\pi} = 2^{-}$ p-wave resonance at five angles. The channel spin mixing ratio ξ is varied in increments of 0.25, ranging from pure $s = 2$ ($\xi = 0$) in the left-most column to pure $s = 3$ ($\xi = 1$) in the right-most column.

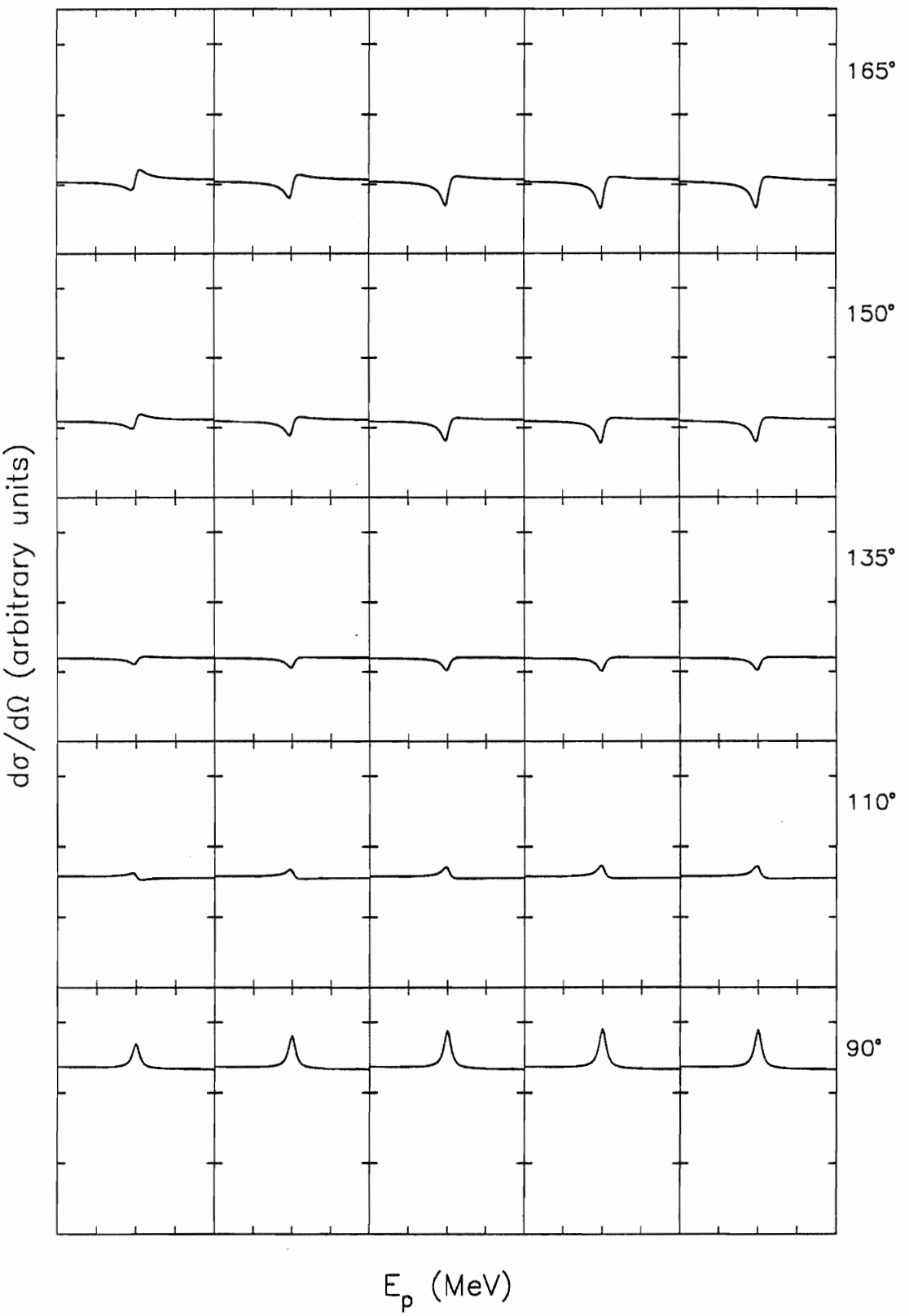
165°
150°
135°
110°
90°
dσ/dΩ (arbitrary units)
E_p (MeV)

Figure 4.12 Variation of resonance shape with channel spin admixture for a $J^{\pi} = 2^{-}$ p-wave resonance at 90° and 165°. The channel spin mixing ratio is varied in increments of 0.25, as follows:

ξ	line style
0.00	solid
0.25	dash
0.50	dash-dot
0.75	dot
1.00	dash-dot-dot-dot

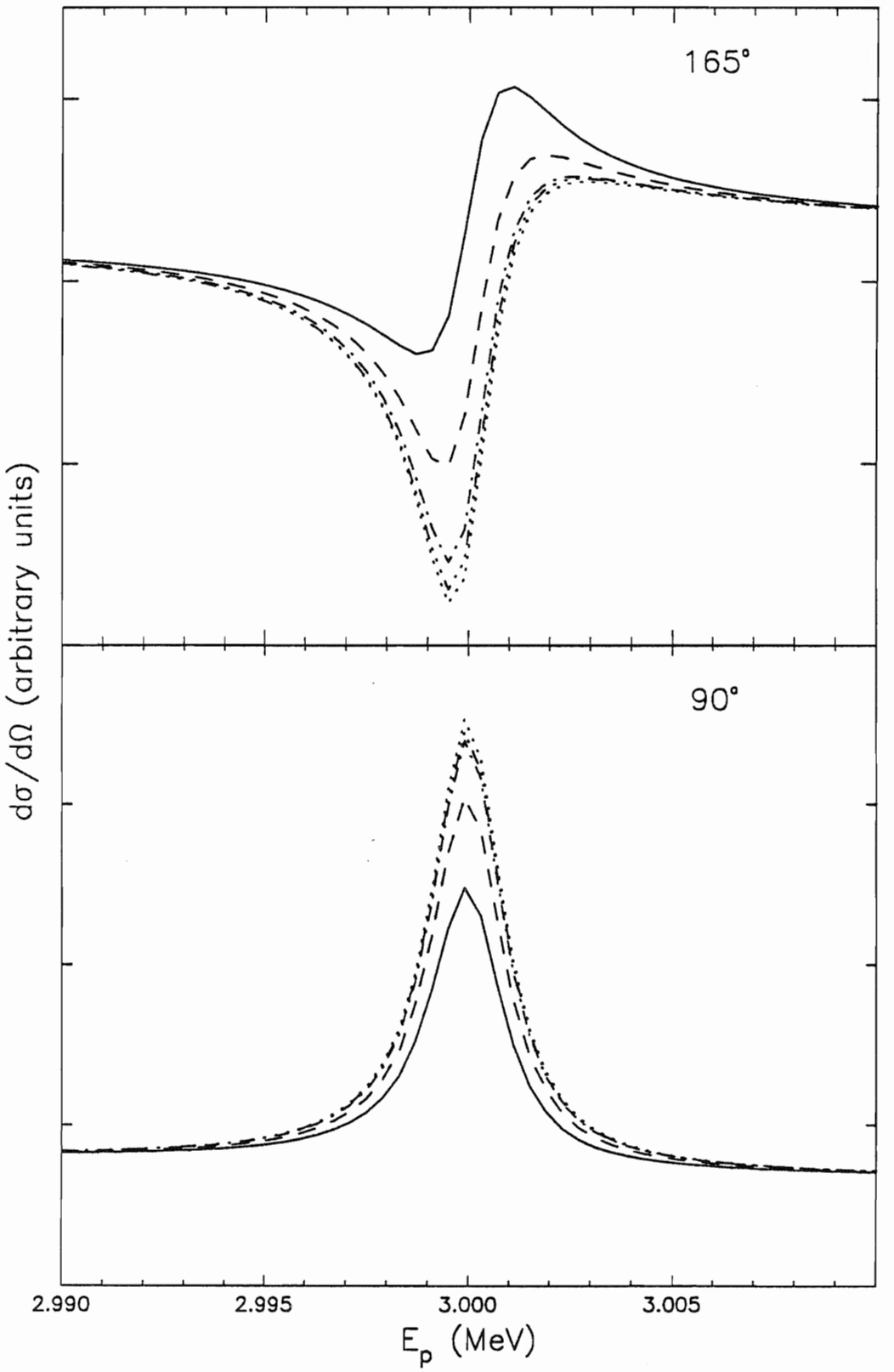
165°
90°
dσ/dΩ (arbitrary units)
2.990
2.995
3.000
3.005
E_p (MeV)

Figure 4.13 Variation of resonance shape with channel spin admixture for a $J^{\pi} = 3^{+}$ d-wave resonance at five angles. The channel spin mixing ratio ξ is varied in increments of 0.25, ranging from pure $s = 2$ ($\xi = 0$) in the left-most column to pure $s = 3$ ($\xi = 1$) in the right-most column.

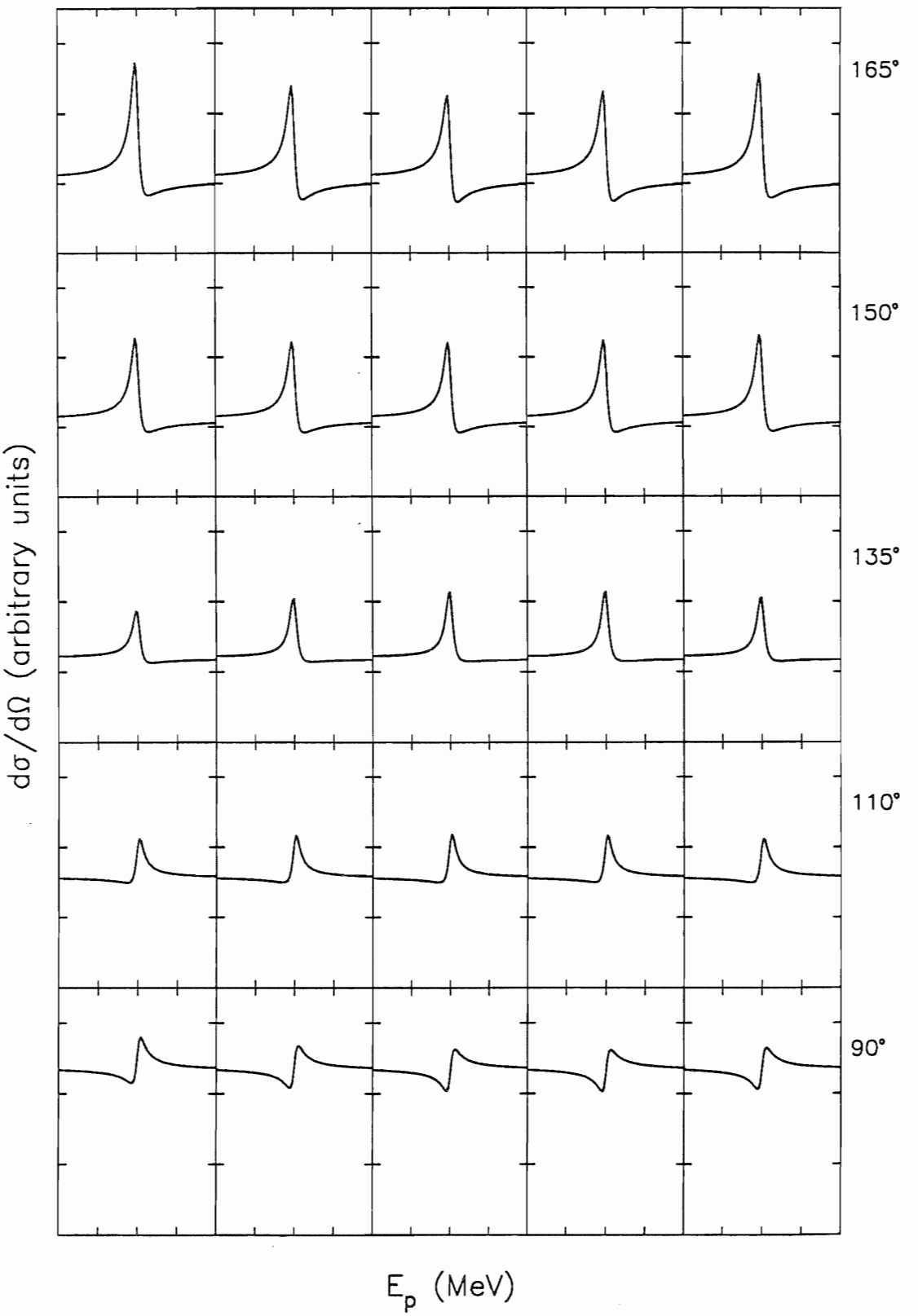
165°
150°
135°
110°
90°
dσ/dΩ (arbitrary units)
E_p (MeV)

Figure 4.14 Variation of resonance shape with channel spin admixture for a $J^{\pi} = 3^{+}$ d-wave resonance at 90° and 165°. The channel spin mixing ratio is varied in increments of 0.25, as follows:

ξ	line style
0.00	solid
0.25	dash
0.50	dash-dot
0.75	dot
1.00	dash-dot-dot-dot

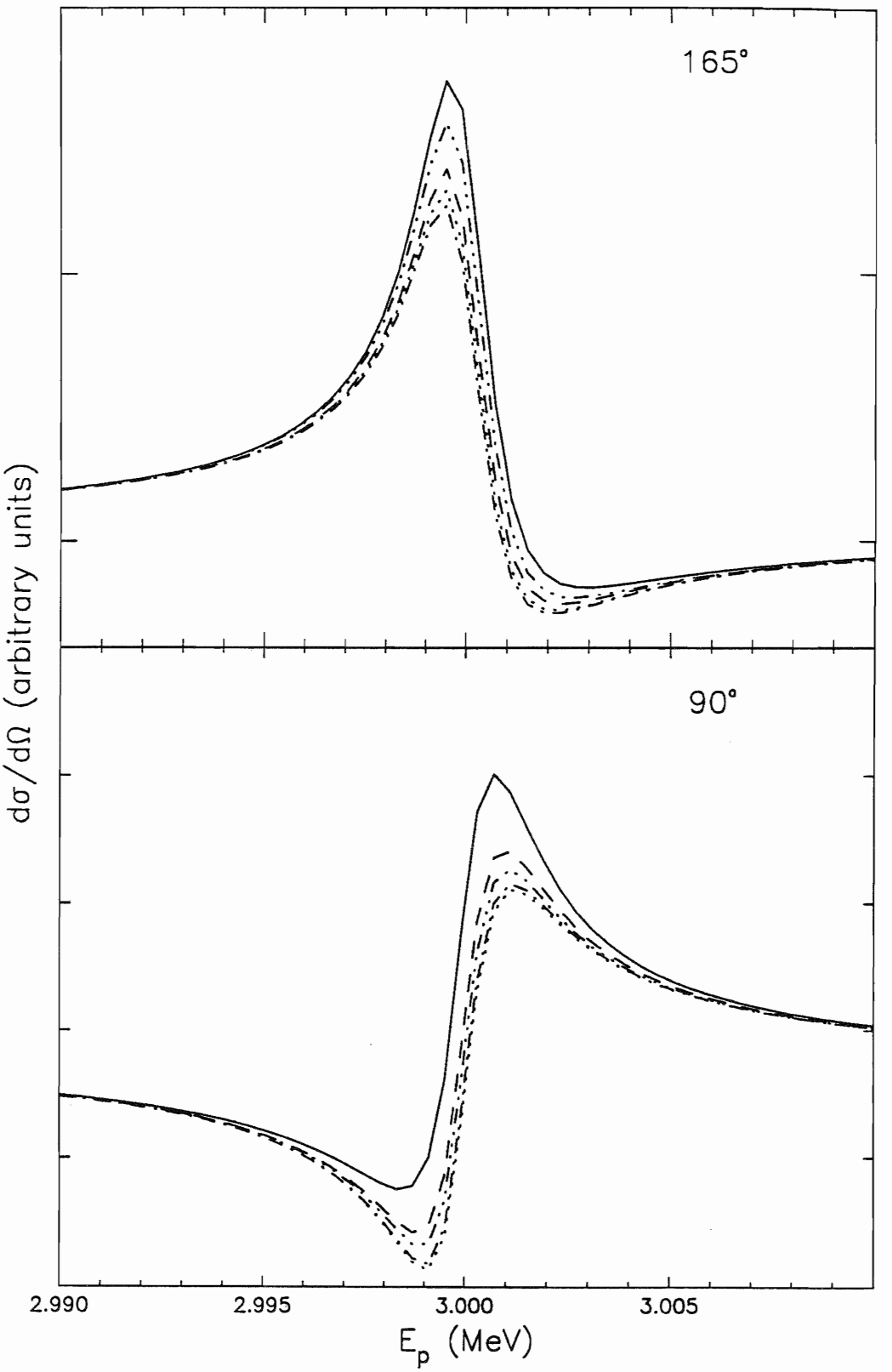
165°
90°
dσ/dΩ (arbitrary units)
2.990
2.995
3.000
3.005
E_p (MeV)

5. Orbital Angular Momentum Mixing

Figures 4.15 through 4.17 give examples of orbital angular momentum mixing. It is convenient to discuss orbital angular momentum mixing in terms of the mixing ratios and mixing angles, defined as follows:

$$\varepsilon = \pm\sqrt{\frac{\Gamma_{p,s,l+2}}{\Gamma_{p,s,l}}}$$
$$\tan\psi = \varepsilon \quad .$$

Thus, ε is equal to zero for formation with only the lowest l-value, and is infinite for formation with pure $l + 2$, and ψ correspondingly varies from -90° to +90°.

Figure 4.15 shows resonances of $J^{\pi} = 3^{+}$, $s = 3$ at five angles, with the orbital angular momentum values ranging from pure $l = 0$ to pure $l = 2$, with the mixing angle ψ varied in increments of 45°. The back angles all exhibit similar changes in shape, with the most pronounced difference being found at 165°. Figure 4.16 shows the angles of 90° and 165° in detail, with the cross sections superimposed. Figure 4.17 shows orbital angular momentum mixing between $l = 1$ and $l = 3$ for $J^{\pi} = 3^{-}$, $s = 2$. In these, the main difference between the different ratios is the height of the resonance. This makes determination of a unique value for ψ more difficult than for the 3^{+} resonances, and it is sometimes necessary to utilize more than two angles when analyzing negative parity resonances.

Figure 4.15 Variation of resonance shape with orbital angular momentum admixture for a $J^{\pi} = 3^{+}$, $s = 3$ resonance at five angles. The orbital angular momentum mixing angle ψ is varied in increments of 45°, ranging from pure $l = 0$ (ψ = -90°) in the left-most column to pure $l = 2$ (ψ = +90°) in the rightmost column.

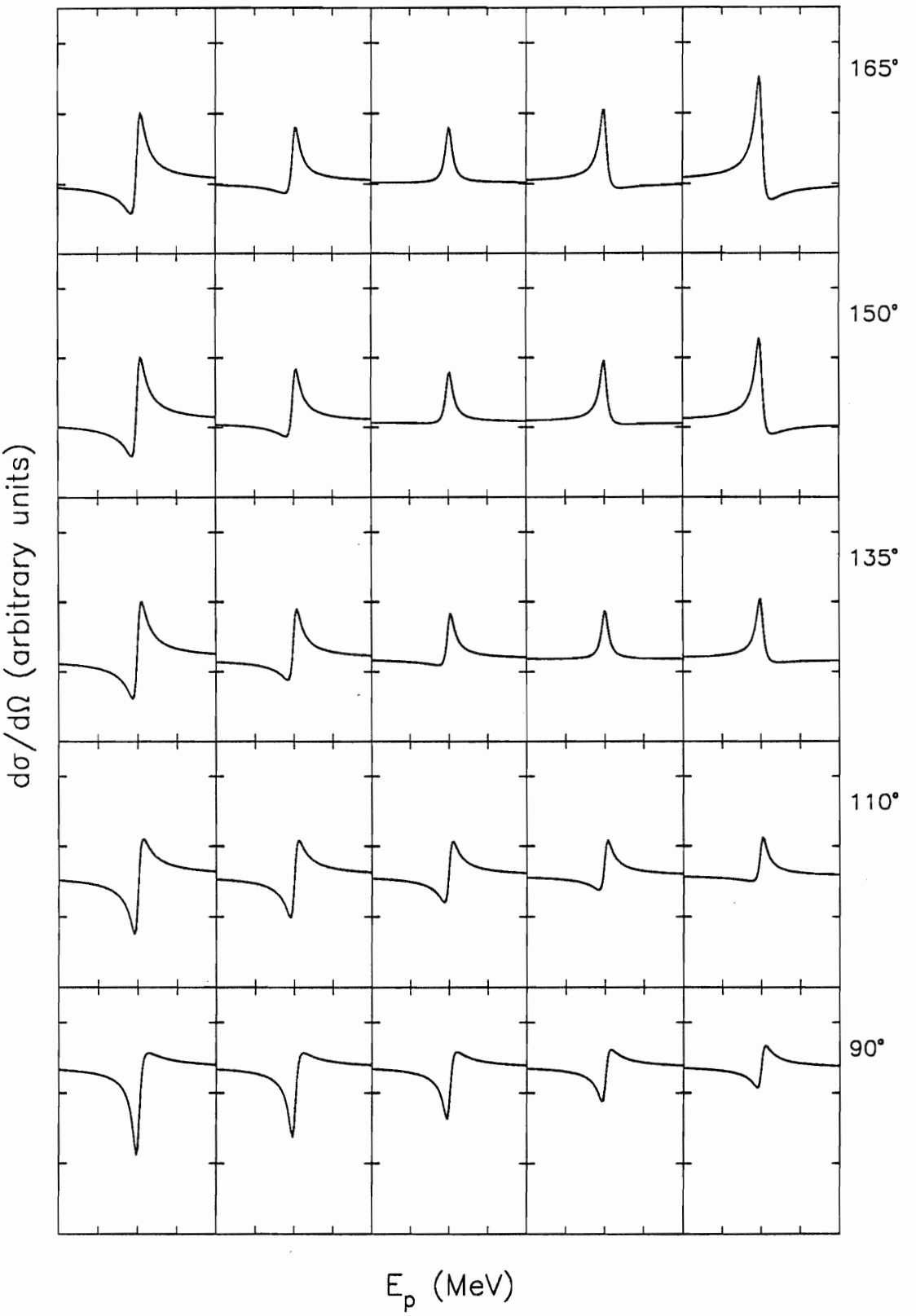
165°
150°
135°
110°
90°
dσ/dΩ (arbitrary units)
E_p (MeV)

Figure 4.16 Variation of resonance shape with orbital angular momentum admixture for a $J^{\pi} = 3^{+}$, $s = 3$ resonance at 90° and 165°. The orbital angular momentum mixing angle is varied in increments of 45°, as follows:

ψ	line style
-90°	solid
-45°	dash
0°	dash-dot
+45°	dot
+90°	dash-dot-dot-dot

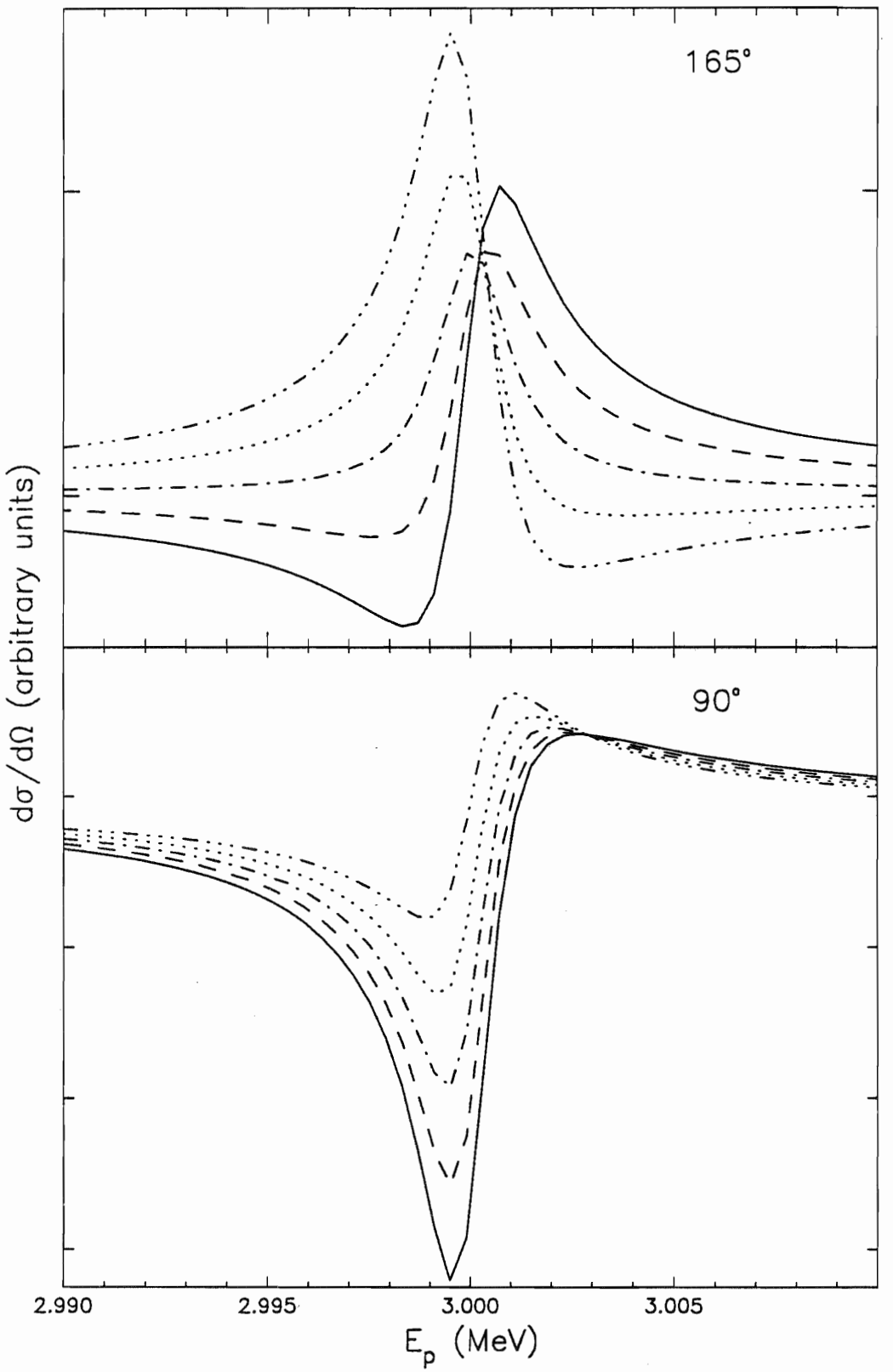
165°
90°
dσ/dΩ (arbitrary units)
2.990
2.995
3.000
3.005
E_p (MeV)

Figure 4.17 Variation of resonance shape with orbital angular momentum admixture for a $J^{\pi} = 3^{-}$, $s = 2$ resonance at five angles. The orbital angular momentum is varied from pure $l = 1$ to pure $l = 3$. The orbital angular momentum mixing angle ψ is varied in increments of 45°, ranging from pure $l = 1$ (ψ = -90°) in the left-most column to pure $l = 3$ (ψ = +90°) in the rightmost column.

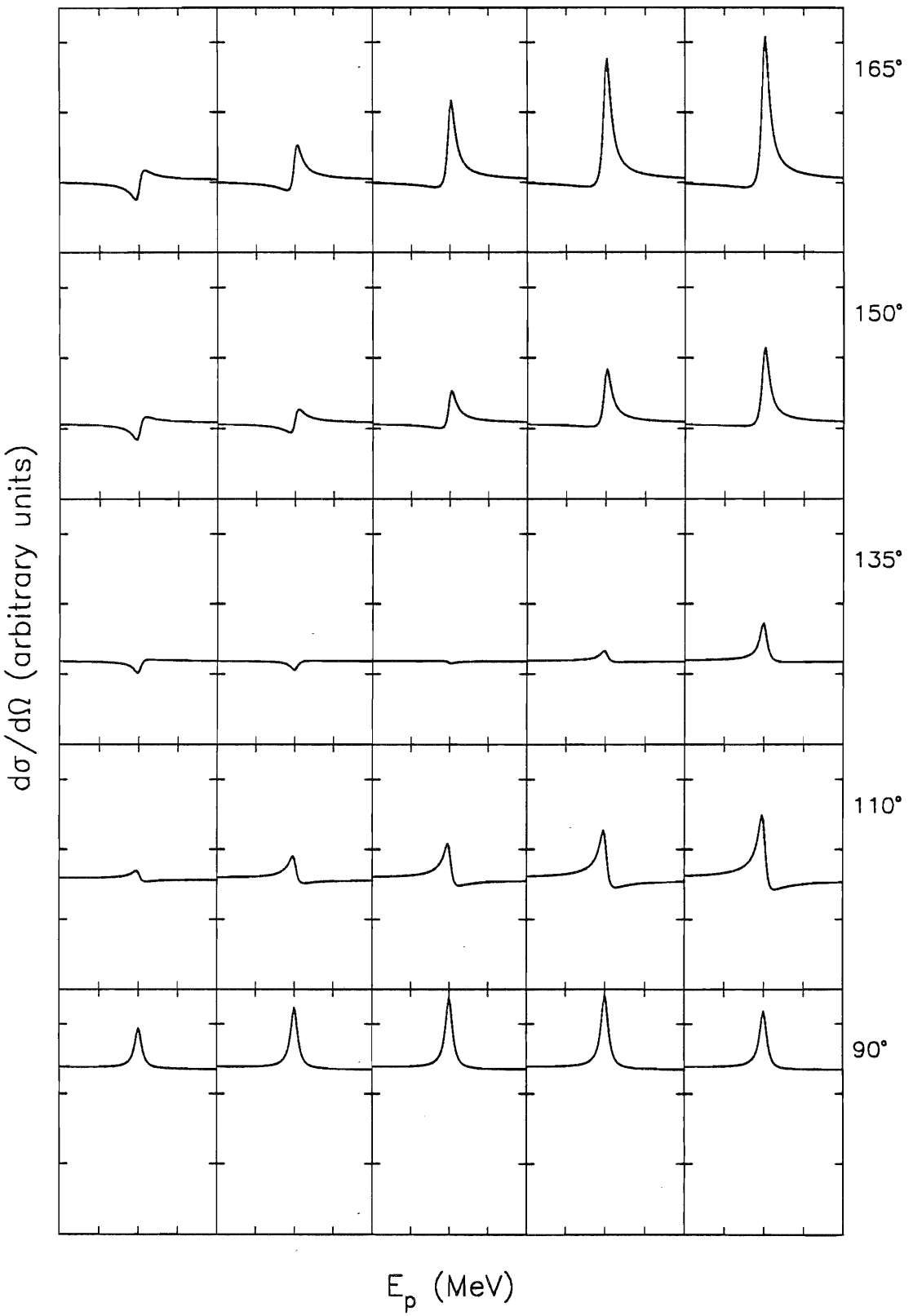
165°
150°
135°
110°
90°
dσ/dΩ (arbitrary units)
E_p (MeV)

6. Interference Effects

The large number of open channels greatly complicates the data fitting procedure for this experiment. A unique determination for the channel spin mixing ratio was often impossible to obtain. The values for the total spin and for the orbital angular momentum mixing angles were often ambiguous as well. This was especially true at higher energies, when the resonances were no longer isolated. Neighboring resonances can interfere to drastically affect the shape of excitation functions. The influence of nearby interfering resonances has been described by Nelson (1985). Interference between two levels with different J^{π} is discussed by Fang (1987) along with interference between two levels with the same J^{π}. Brooks (1988) examines a number of various multilevel interference effects.

Interference effects typically increase with increasing incident proton energy, as a result of the increased number of energy levels in the compound nucleus. Usually the existence of an open (p,α) channel is very useful in the data analysis, because α-decay requires the level to have natural parity ($\pi = (-1)^J$). Unfortunately, for this experiment the (p,α) channel was not energetically allowed. The inelastically scattered proton data was not very helpful. Both entrance and exit *s*- and *l*-mixing were allowed, and the (p,p′) cross sections were usually so small that the quality of the data was much poorer than the data for the elastic scattering. Above E_p = 3.0 MeV the number of overlapping resonances prohibited the determination of unambiguous resonance parameters. As a result, the fit for this region is poorer than the fit for the region below E_p = 3.0 MeV.

CHAPTER V

DATA PRESENTATION

The primary experimental results are presented in this chapter. In the present experiment, excitation functions were measured for the region E_p = 1.9 - 3.4 MeV. These are presented in the first section of this chapter. A total of 64 resonances were observed and fit in this region. These data complement an earlier study of the same reactions performed at this laboratory, which covered the region E_p = 0.7 - 2.0 MeV and reported 46 resonances. The earlier data have been reanalyzed for this dissertation and some changes in the resonance parameters have been made. The second section of this chapter presents an updated list of resonance parameters for the region E_p = 0.7 - 2.0 MeV, and the third section presents the resonance parameters extracted from the data obtained in this experiment.

A. Excitation Functions

Detailed plots of the excitation functions for elastic scattering at 4 angles are shown in figures 5.1 through 5.5. Although five detector angles were used, in most cases the excitation functions for 150° and 165° are very similar, and the curves for 150° are not presented here. The top portion of each plot indicates the spin and parity of each resonance. Tic marks are displayed on all the excitation functions to aid location of the resonances.

Figure 5.1 Differential cross sections for the $^{25}Mg(p,p_0)^{25}Mg$ reaction at θ_{lab} = 165°, 135°, 108°, and 90° from E_p = 1.946 to 3.000 MeV. The solid curve is an *R*-matrix fit. The top portion of the plot indicates the *J*-value of each resonance by a symbol located at the position of the resonance along the energy axis. The symbol is either a plus or minus sign, denoting the parity of the resonance.

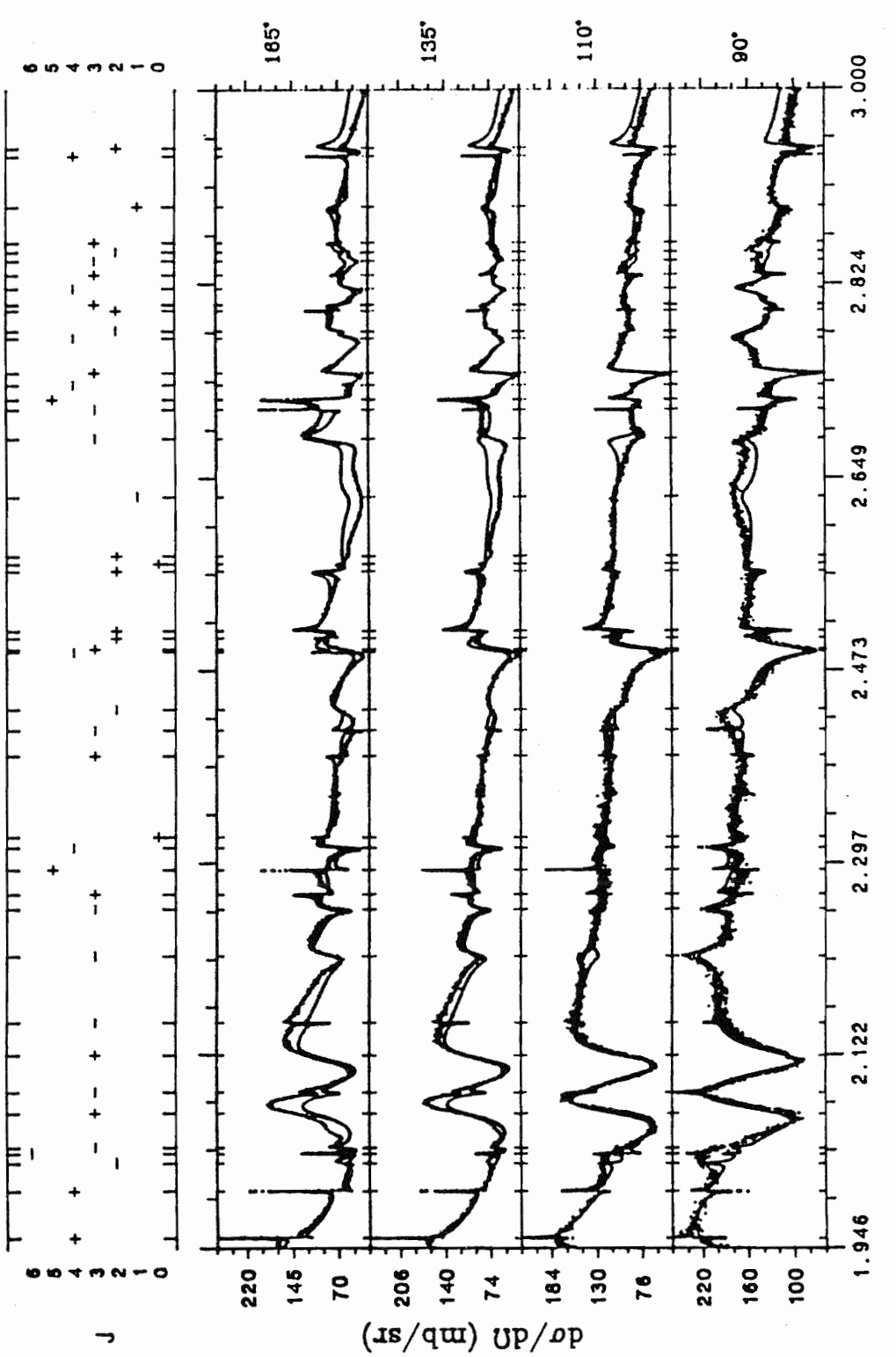
185°
135°
110°
90°
J
dσ/dΩ (mb/sr)
E_p (MeV)
1.946
2.122
2.297
2.473
2.649
2.824
3.000

Figure 5.2 Differential cross sections for the $^{25}Mg(p,p_0)^{25}Mg$ reaction at θ_{lab} = 165°, 135°, 108°, and 90° from E_p = 2.00 to 2.33 MeV. The solid curve is an *R*-matrix fit. The top portion of the plot indicates the *J*-value of each resonance by a symbol located at the position of the resonance along the energy axis. The symbol is either a plus or minus sign, denoting the parity of the resonance.

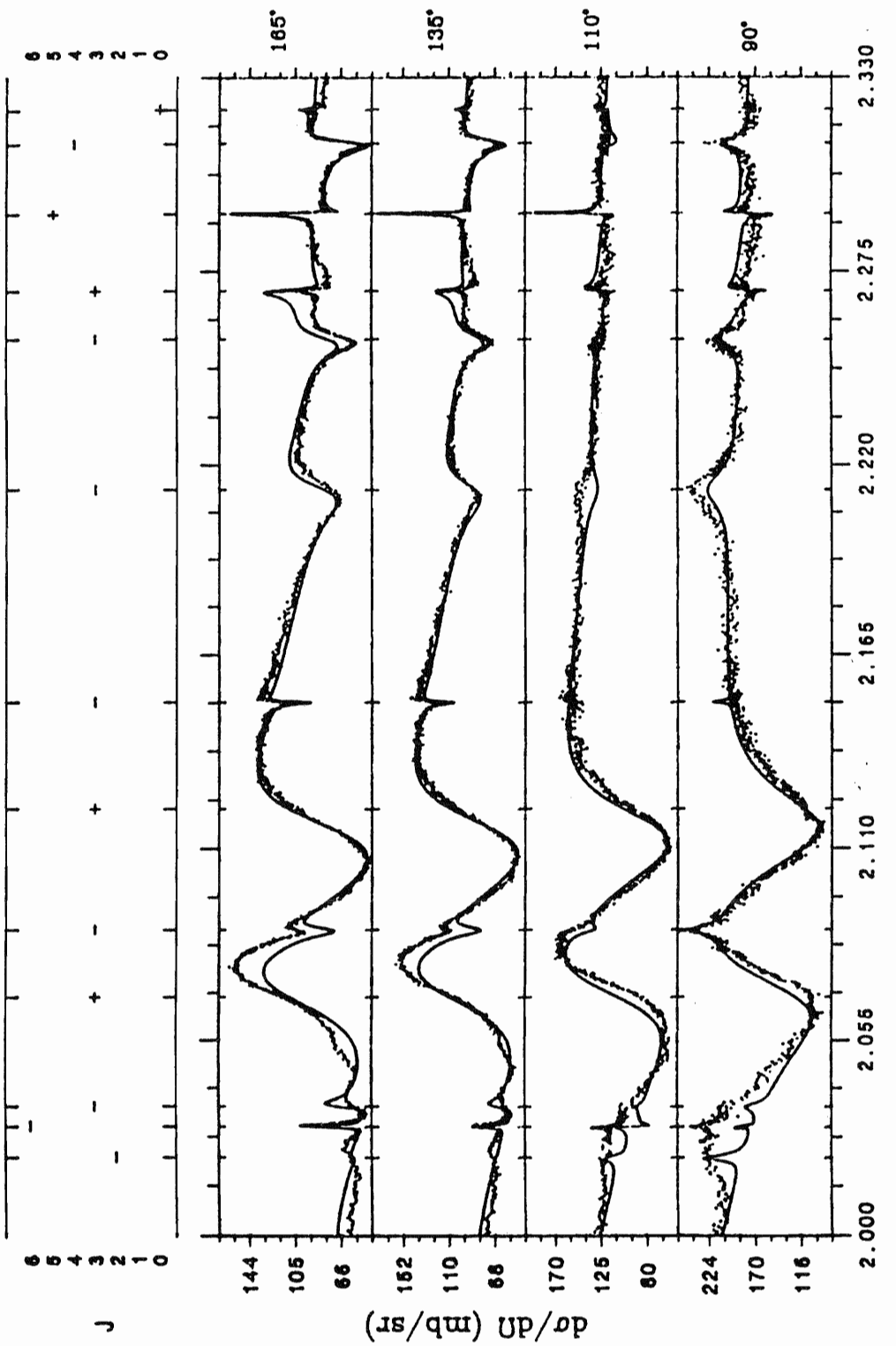
J
dσ/dΩ (mb/sr)
E_p (MeV)
165°
135°
110°
90°
2.000
2.055
2.110
2.165
2.220
2.275
2.330

Figure 5.3 Differential cross sections for the $^{25}Mg(p,p_0)^{25}Mg$ reaction at θ_{lab} = 165°, 135°, 108°, and 90° from E_p = 2.33 to 2.67 MeV. The solid curve is an *R*-matrix fit. The top portion of the plot indicates the *J*-value of each resonance by a symbol located at the position of the resonance along the energy axis. The symbol is either a plus or minus sign, denoting the parity of the resonance.

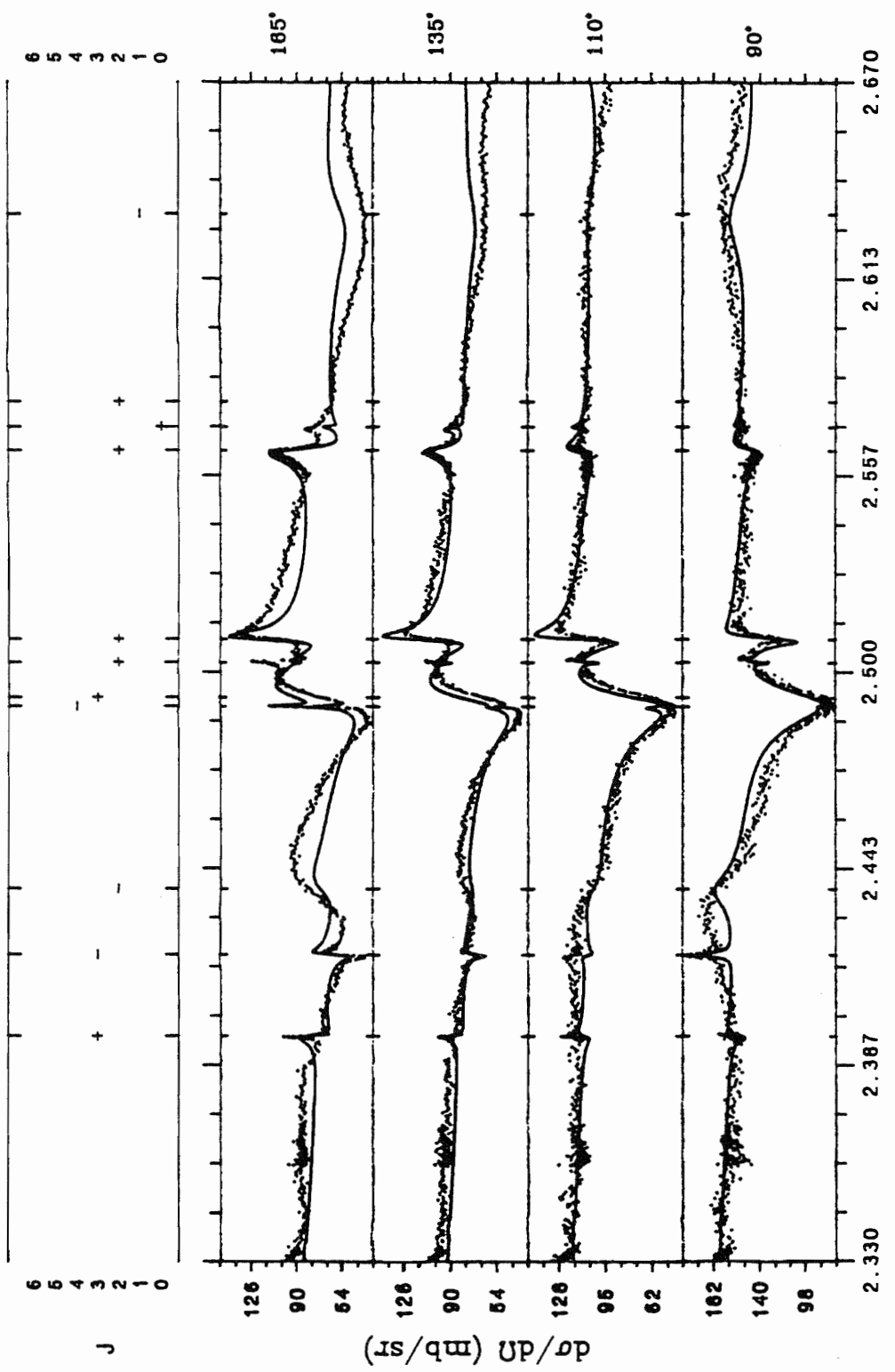
185°
135°
110°
90°
J
dσ/dΩ (mb/sr)
E_p (MeV)

Figure 5.4 Differential cross sections for the $^{25}Mg(p,p_0)^{25}Mg$ reaction at θ_{lab} = 165°, 135°, 108°, and 90° from E_p = 2.67 to 3.00 MeV. The solid curve is an *R*-matrix fit. The top portion of the plot indicates the *J*-value of each resonance by a symbol located at the position of the resonance along the energy axis. The symbol is either a plus or minus sign, denoting the parity of the resonance.

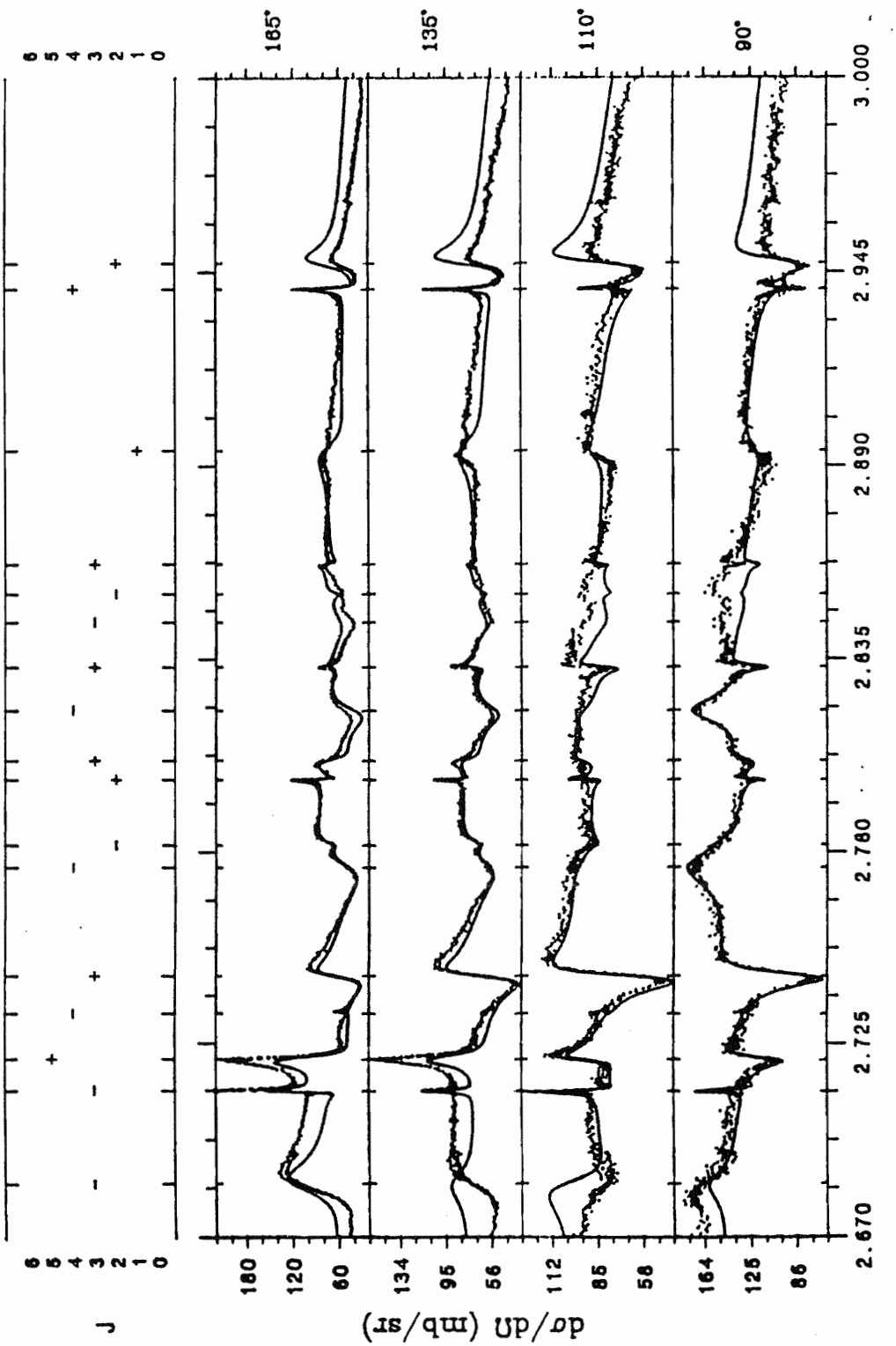
185°
135°
110°
90°
J
dσ/dΩ (mb/sr)
E_p (MeV)
2.670
2.725
2.780
2.835
2.890
2.945
3.000

Figure 5.5 Differential cross sections for the $^{25}Mg(p,p_0)^{25}Mg$ reaction at θ_{lab} = 165°, 135°, 108°, and 90° from E_p = 3.00 to 3.43 MeV. The solid curve is an *R*-matrix fit. The top portion of the plot indicates the *J*-value of each resonance by a symbol located at the position of the resonance along the energy axis. The symbol is either a plus or minus sign, denoting the parity of the resonance.

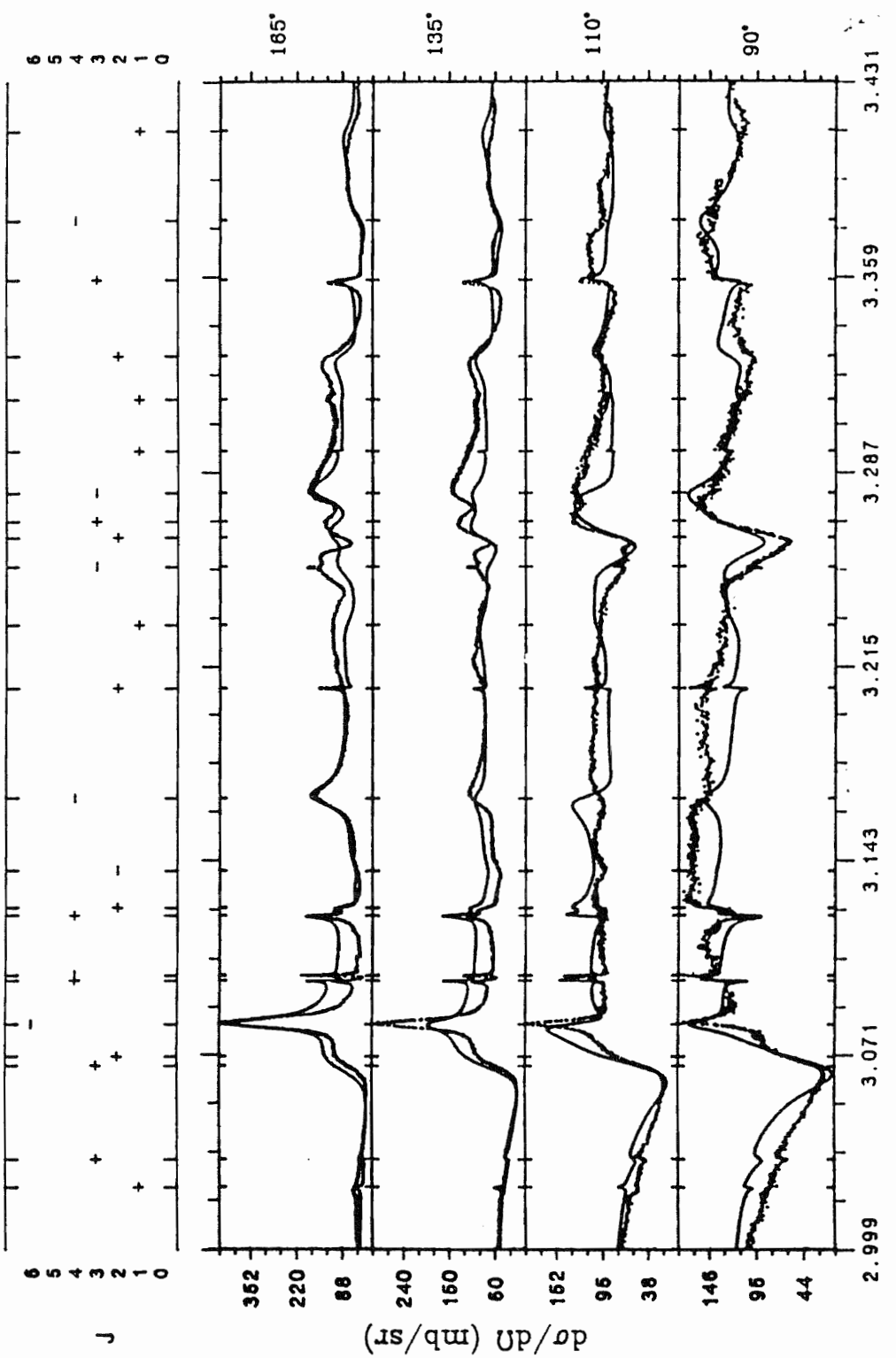
J
π
dσ/dΩ (mb/sr)
165°
135°
110°
90°
352
220
88
240
150
60
152
95
38
146
95
44
2.999
3.071
3.143
3.215
3.287
3.359
3.431
E_p (MeV)

The energy range E_p = 1.946 to 3.124 MeV is presented in figure 5.1. Figures 5.2 through 5.4 show the region from E_p = 2.0 to 3.0 MeV in greater detail. Above E_p = 3.0 MeV, obtaining a reasonable fit to the data became increasingly difficult. The region from E_p = 3.0 MeV to 3.43 MeV is shown in figure 5.5.

B. Resonance Parameters for E_p = 0.7 - 2.0 MeV

Table 5.1 lists resonance parameters for the energy region E_p = 0.7 - 2.0 MeV, using data measured by Adams (1983). The energies listed are those given by Adams. Additional studies of the same compound nucleus via other reactions (Endt *et al.*, 1986) gave excellent overall agreement with this earlier work. However, measurements by Peterson *et al.* (1988) raised issues on a few specific states. Adams' data has been reanalyzed; the resonances that have been changed are indicated by an asterisk in front of the energy in table 5.1. Two of the resonances indicated are new, and the energies of these resonances have been normalized to the energies of their nearest neighbors. Details of the motivation for re-examining these data will be presented in the next chapter along with results of the current analysis and a comparison to the previous results. The data and fit for this energy region with the current resonance parameters are shown in figures 5.6 through 5.9.

Table 5.1
The $^{25}Mg(p,p_0)^{25}Mg$ Resonance Parameters For E_p = 0.7 - 2.0 MeV

E_p (MeV)	J^π	l	s	Γ_p (eV)	γ_p^2 (keV)
0.835	4^-	1	2	75	24.3
0.869	2^-	1	2	200	50.3
0.881	3^+	0	3	88	5.12
0.890	3^-	1	3	55	12.0
0.897	4^-	1	3	80	16.6
0.969	3^-	1	2	75	9.78
		1	3	25	3.26
0.986	2^-	1	2	3400	402
1.025	4^+	2	2	55	57.5
1.083	4^-	1	3	1300	90.3
1.134	2^+	0	2	45	0.69
1.137	3^-	1	2	1370	73.5
		1	3	350	18.8

Table 5.1 (Continued)

E_p (MeV)	J^π	l	s	Γ_p (eV)	γ_p^2 (keV)
1.148	4^-	1	3	200	10.2
1.164	3^+	2	3	85	40.7
1.183	1^-	1	2	40	1.74
1.238	3^+	0	3	80	.822
1.239	2^-	1	2	675	23.3
		1	3	75	2.59
*1.273	6^-	3	3	15	88.8
1.284	2^-	1	2	1580	45.8
		1	3	100	2.90
1.302	2^+	0	2	65	.537
		2	2	100	25.0
1.307	2^+	0	2	2800	22.8
		2	2	150	36.7
*1.339	4^+	2	2	10	2.14
1.352	2^-	1	2	575	13.0
		1	3	55	1.24

Table 5.1 (Continued)

E_p (MeV)	J^π	l	s	Γ_p (eV)	γ_p^2 (keV)
1.376	5^+	2	3	10	1.83
*1.484	2^-	1	2	65	.953
1.514	3^-	1	2	525	7.04
		1	3	975	13.1
1.526	1^-	1	2	5400	69.8
1.569	1^+	2	2	650	58.3
*1.580	4^-	1	3	840	9.33
		3	2	15	22.3
*1.588	4^+	2	2	50	4.23
1.623	2^+	0	2	6300	22.0
		2	2	275	20.7
1.632	3^+	0	3	1100	3.78
		2	3	50	3.66
1.650	4^+	2	2	500	34.6
		2	3	400	27.7

Table 5.1 (Continued)

E_p (MeV)	J^π	l	s	Γ_p (eV)	γ_p^2 (keV)
1.699	3^+	0	3	1400	4.18
		2	3	275	16.4
1.714	4^+	2	2	130	7.39
		2	3	190	10.8
1.744	2^+	0	2	11300	31.0
		2	2	550	28.7
1.763	1^-	1	2	400	2.82
1.771	2^+	0	2	525	1.37
		2	2	325	15.7
*1.774	5^-	3	2	80	58.8
1.811	3^-	1	2	1330	8.44
		1	3	570	3.62
1.829	2^+	0	2	6700	15.8
		2	2	600	24.7
*1.833	5^-	3	2	30	18.2
		3	3	95	57.6
1.883	3^+	0	3	5850	12.6

Table 5.1 (Continued)

E_p (MeV)	J^π	l	s	Γ_p (eV)	γ_p^2 (keV)
1.898	1^-	3	3	200	98.7
1.899	3^-	1	2	1500	7.94
		1	3	1800	9.52
1.933	1^-	1	2	5500	27.5
1.943	3^+	0	3	23000	45.2
1.956	4^+	2	2	260	7.76
1.998	4^+	2	2	570	15.4
		2	3	30	.812

Figure 5.6 Differential cross sections for the $^{25}Mg(p,p_0)^{25}Mg$ reaction at θ_{lab} = 165°, 135°, 108°, and 90° from E_p = 0.70 to 2.00 MeV. The solid curve is an *R*-matrix fit. The top portion of the plot indicates the *J*-value of each resonance by a symbol located at the position of the resonance along the energy axis. The symbol is either a plus or minus sign, denoting the parity of the resonance.

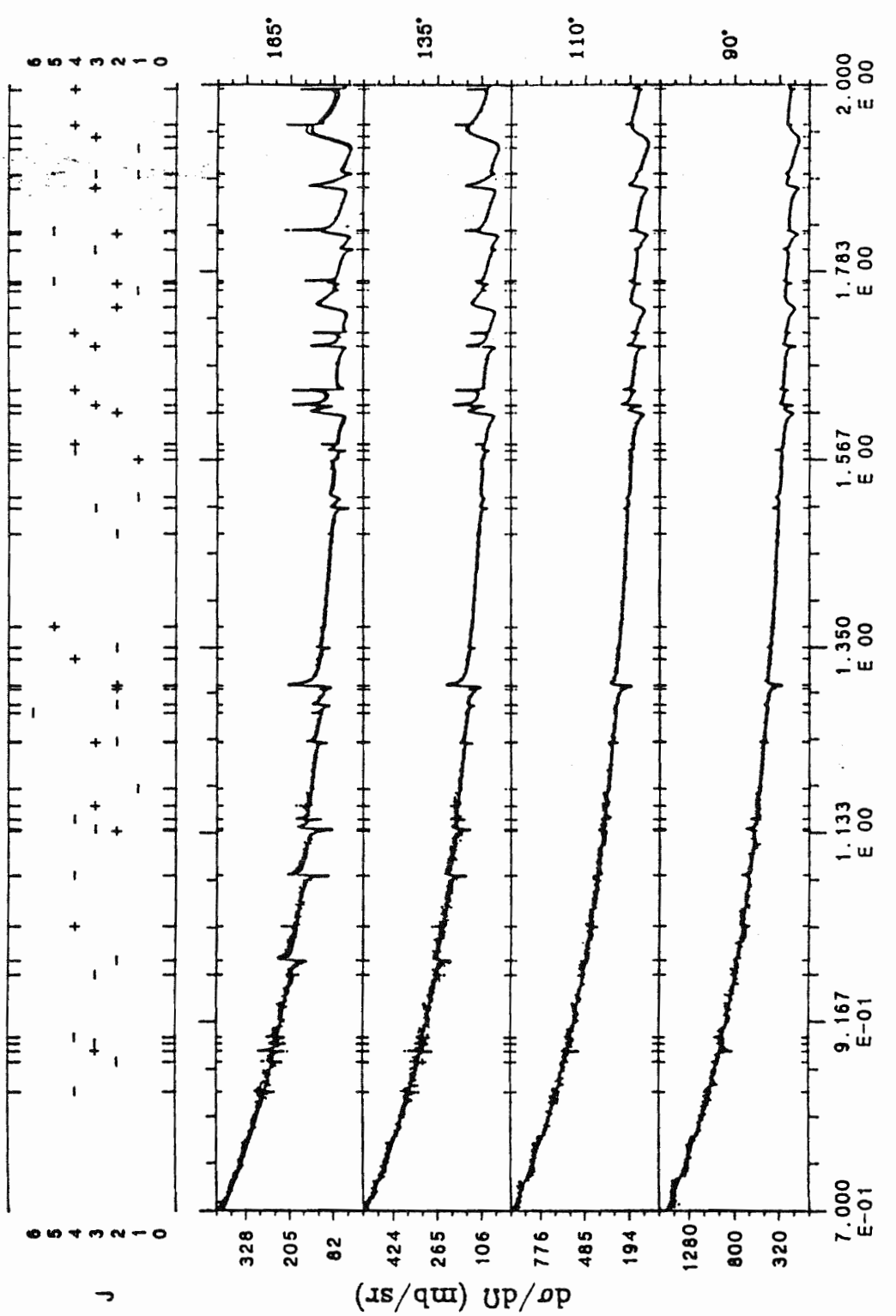
J
dσ/dΩ (mb/sr)
E_p (MeV)
165°
135°
110°
90°
7.000 E-01
9.167 E-01
1.133 E 00
1.350 E 00
1.567 E 00
1.783 E 00
2.000 E 00

Figure 5.7 Differential cross sections for the $^{25}Mg(p,p_0)^{25}Mg$ reaction at θ_{lab} = 165°, 135°, 108°, and 90° from E_p = 0.70 to 1.13 MeV. The solid curve is an *R*-matrix fit. The top portion of the plot indicates the *J*-value of each resonance by a symbol located at the position of the resonance along the energy axis. The symbol is either a plus or minus sign, denoting the parity of the resonance.

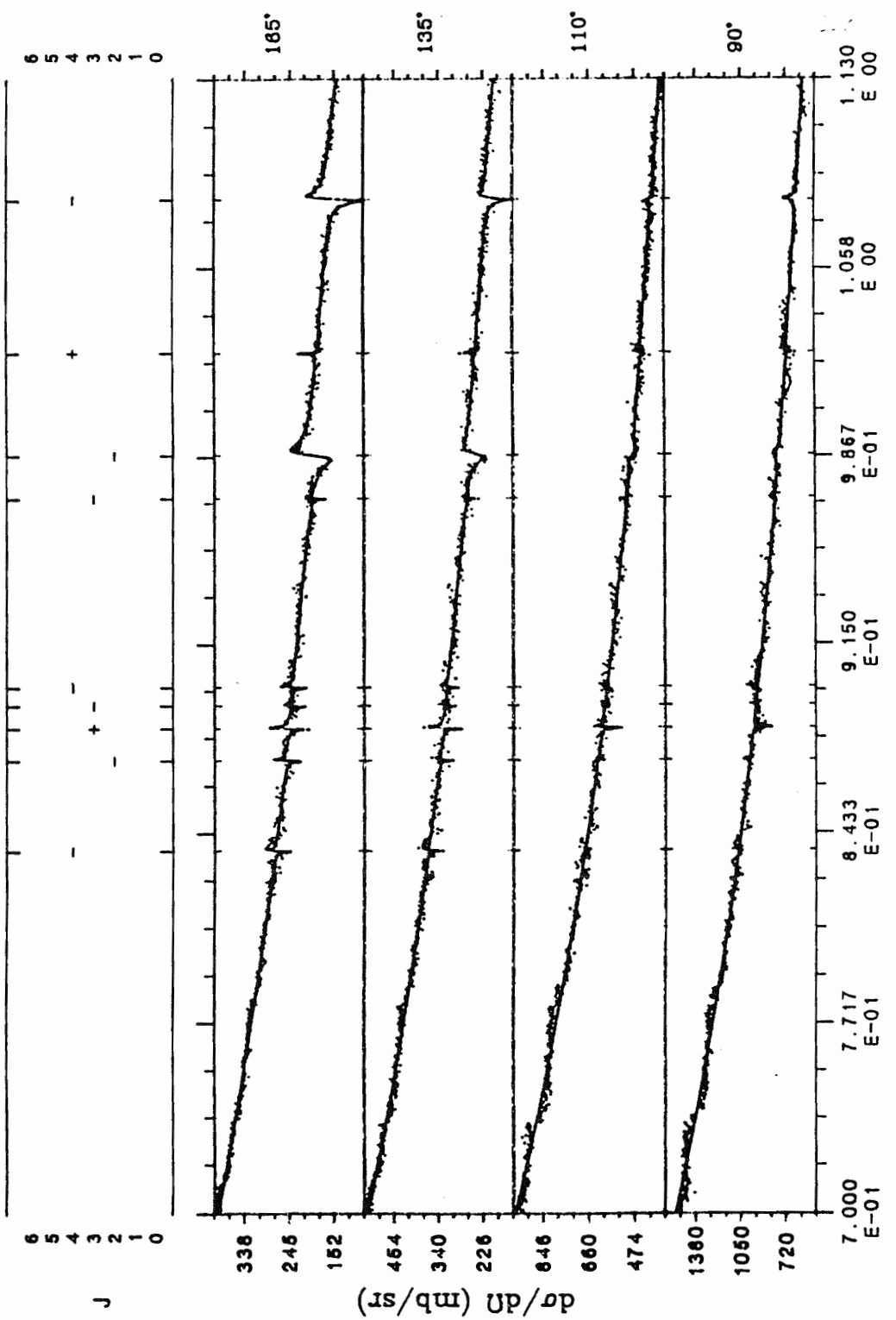
165°
135°
110°
90°
dσ/dΩ (mb/sr)
J
E_p (MeV)

Figure 5.8 Differential cross sections for the $^{25}Mg(p,p_0)^{25}Mg$ reaction at θ_{lab} = 165°, 135°, 108°, and 90° from E_p = 1.13 to 1.57 MeV. The solid curve is an *R*-matrix fit. The top portion of the plot indicates the *J*-value of each resonance by a symbol located at the position of the resonance along the energy axis. The symbol is either a plus or minus sign, denoting the parity of the resonance.

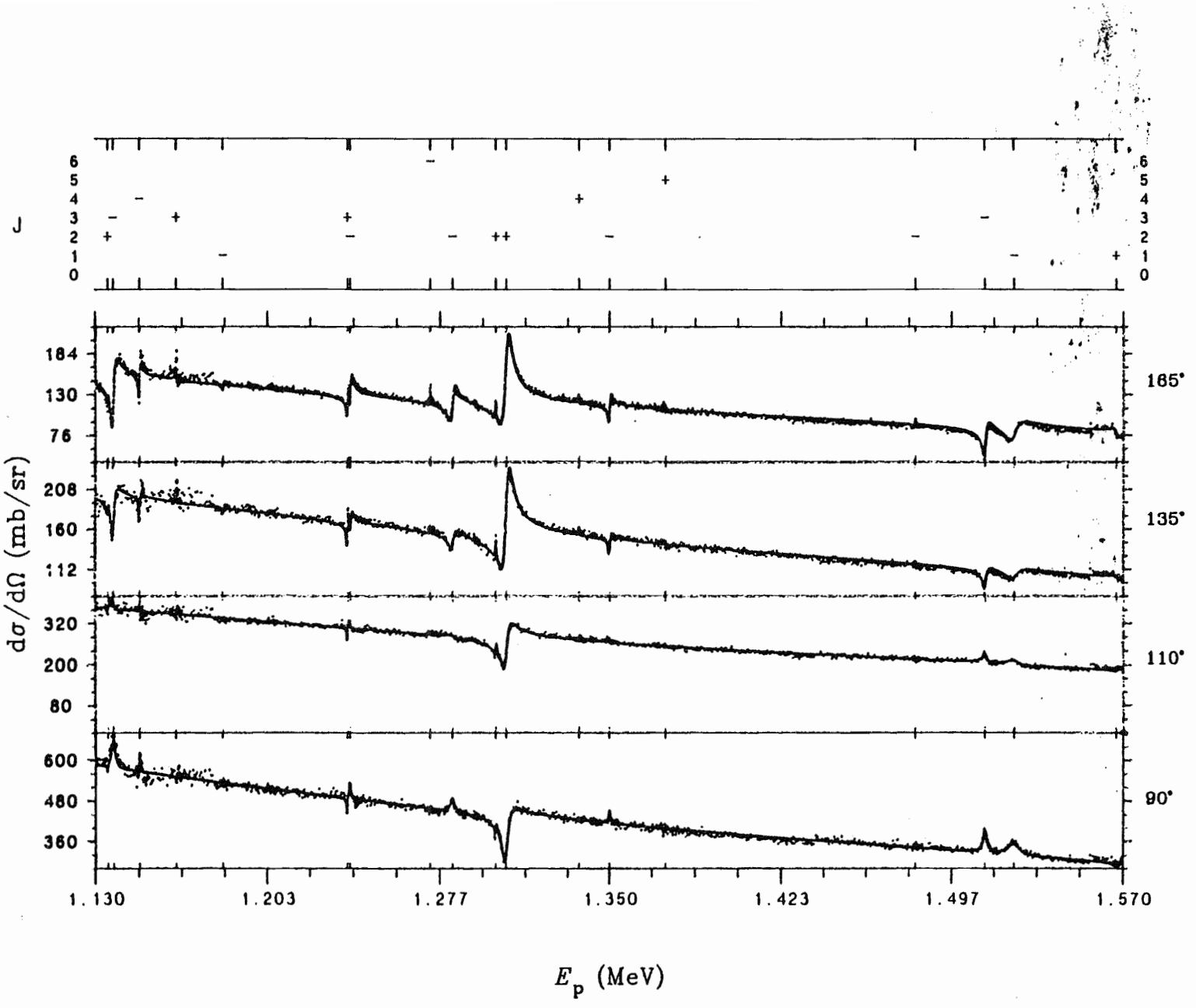
J
6
5
4
3
2
1
0
184
130
76
208
160
112
320
200
80
600
480
360
dσ/dΩ (mb/sr)
165°
135°
110°
90°
1.130
1.203
1.277
1.350
1.423
1.497
1.570
E_p (MeV)

Figure 5.9 Differential cross sections for the $^{25}Mg(p,p_0)^{25}Mg$ reaction at θ_{lab} = 165°, 135°, 108°, and 90° from E_p = 1.57 to 2.00 MeV. The solid curve is an *R*-matrix fit. The top portion of the plot indicates the *J*-value of each resonance by a symbol located at the position of the resonance along the energy axis. The symbol is either a plus or minus sign, denoting the parity of the resonance.

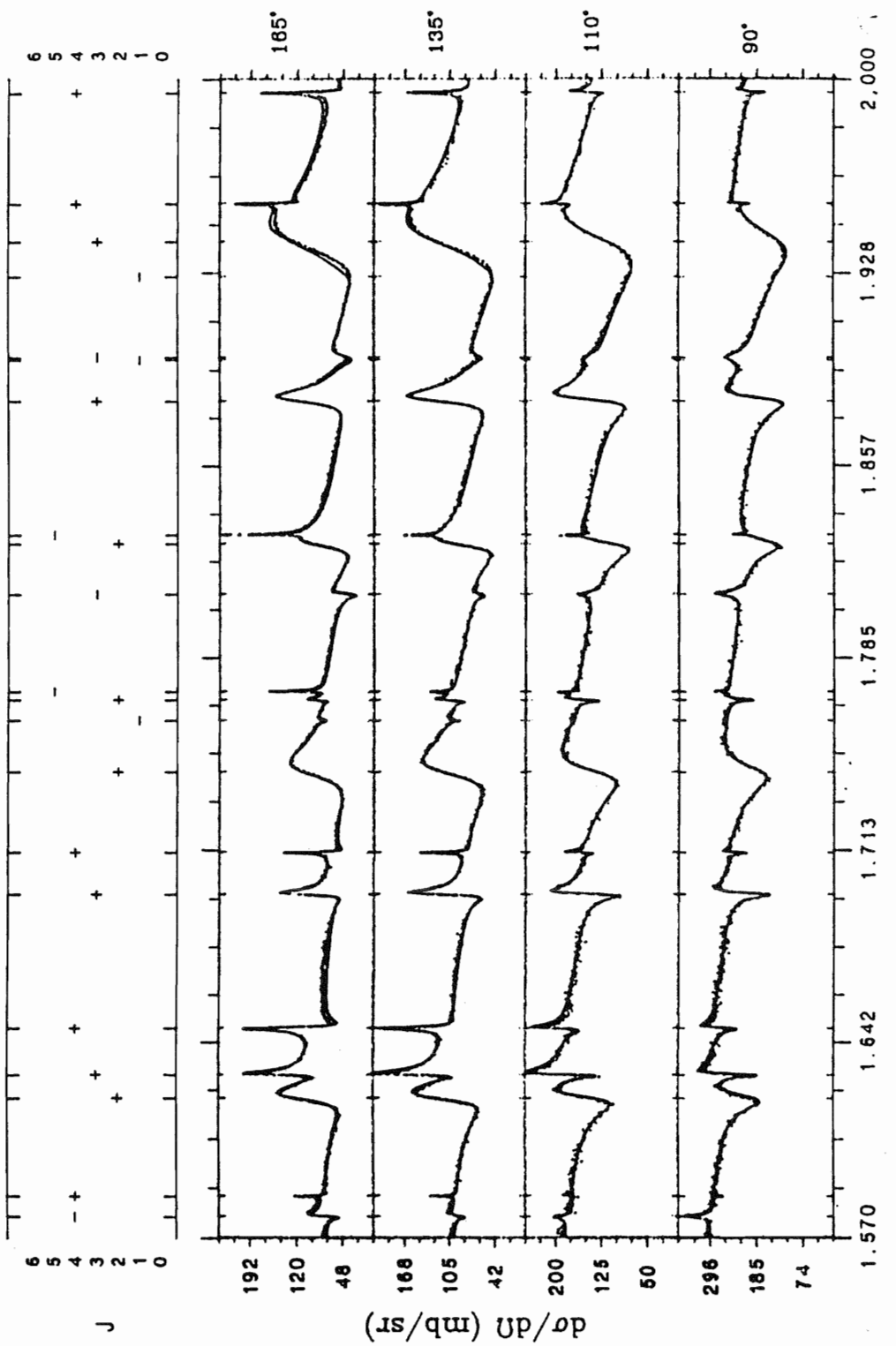
J
dσ/dΩ (mb/sr)
E_p (MeV)
165°
135°
110°
90°
1.570
1.642
1.713
1.785
1.857
1.928
2.000

C. Resonance Parameters for E_p = 1.9 - 3.4 MeV

The resonance parameters for elastic scattering extracted from the excitation functions obtained in the present experiment are listed in Table 5.2. The proton elastic width is the sum of the partial proton elastic widths. Typical uncertainties in the widths are ~±10% for resonances with laboratory widths less than a few keV, and as much as ±30% for large resonances (~50 keV). Tables 5.3 and 5.4 list the resonance parameters for proton inelastic scattering for the energy region E_p = 0.7 - 3.4 MeV.

Table 5.2
The $^{25}Mg(p,p_0)^{25}Mg$ Resonance Parameters For E_p = 2.0 - 3.4 MeV

E_p (MeV)	J^π	l	s	Γ_p (eV)	γ_p^2 (keV)
2.0217	2^-	1	3	2000	8.39
2.0304	6^-	3	3	250	83.4
2.0361	3^-	1	3	2000	8.18
2.0675	3^+	0	3	25000	41.1
		2	3	2000	45.9
2.0870	3^-	1	3	3000	11.3
2.1213	3^+	0	3	30000	46.1
2.1515	3^-	1	2	400	1.53
		1	3	100	.338
2.2129	3^-	1	3	-12000	37.0
2.2558	3^-	1	3	7000	20.3
2.2695	3^+	2	2	1200	18.2
2.2914	5^+	2	3	300	4.36

Table 5.2 (Continued)

E_p (MeV)	J^π	l	s	Γ_p (eV)	γ_p^2 (keV)
2.3113	4^-	1	3	3000	8.03
2.3209	0^+	2	2	1000	13.7
2.3950	3^+	2	2	700	8.41
2.4185	3^-	1	3	1500	3.49
2.4375	2^-	1	2	12000	27.2
2.4901	4^-	3	2	250	27.3
2.4927	3^+	0	3	9200	9.56
		2	3	800	8.13
2.5028	2^+	0	2	60	.062
2.5095	2^+	0	2	2500	2.56
2.5640	2^+	2	3	3000	27.2
2.5708	0^+	2	2	500	4.48
2.6320	1^-	1	2	25000	45.4

Table 5.2 (Continued)

E_p (MeV)	J^π	l	s	Γ_p (eV)	γ_p^2 (keV)
2.6850	3^-	1	3	2000	3.43
		3	3	6000	442
2.7112	3^-	3	3	800	56.1
2.7204	5^+	2	3	2200	15.7
2.7336	4^-	3	2	100	6.72
2.7444	3^+	0	3	5000	4.25
2.7757	4^-	1	3	12000	18.8
2.7820	2^-	1	2	2000	3.12
2.8006	2^+	2	2	500	3.19
2.8060	3^+	2	2	2000	12.7
2.8204	4^-	1	3	8000	12.0
2.8328	3^+	2	3	400	2.45
		0	3	400	.319
2.8455	3^-	1	3	3000	4.41

Table 5.2 (Continued)

E_p (MeV)	J^π	l	s	Γ_p (eV)	γ_p^2 (keV)
2.8535	2^-	1	2	1000	1.46
2.8620	3^+	2	2	500	2.94
2.8945	1^+	2	2	10000	56.3
2.9403	4^+	2	2	700	3.72
2.9476	2^+	0	2	5700	4.22
3.0220	1^+	2	2	1000	4.80
3.0325	3^+	0	3	500	.352
3.0670	3^+	0	3	15000	10.4
3.0705	2^+	0	2	30000	20.7
3.0826	6^-	3	3	4500	166
3.0990	4^+	2	2	400	1.75
3.1010	4^-	3	2	180	6.46
3.1230	4^+	2	2	1300	5.54
3.1258	2^+	2	3	2300	9.76

Table 5.2 (Continued)

E_p (MeV)	J^π	l	s	Γ_p (eV)	γ_p^2 (keV)
3.1393	2^-	1	3	5000	5.75
3.1660	4^-	3	2	7000	227
		1	3	1000	1.13
3.2070	2^+	2	2	700	2.71
3.2305	1^+	2	2	12000	45.3
		2	3	7000	26.4
3.2520	3^-	3	3	10000	285
3.2630	2^+	0	2	10000	6.21
3.2690	3^+	2	2	7000	25.4
3.2795	3^-	3	2	10000	274
3.2950	1^+	2	2	300	1.06
3.3140	1^+	2	2	1500	5.19
3.3300	2^+	2	2	10000	34.0
3.3580	3^+	2	2	500	1.65
		2	3	1500	4.96

Table 5.2 (Continued)

E_p (MeV)	J^π	l	s	Γ_p (eV)	γ_p^2 (keV)
3.3800	4^-	1	3	15000	14.6
3.4130	1^+	2	2	15000	46.9

Table 5.3
The $^{25}Mg(p,p_1)^{25}Mg$ Resonance Parameters For E_p = 0.7 - 3.4 MeV

E_p (MeV)	J^π	l	s	Γ_{p_1} (eV)	$\gamma_{p_1}^2$ (keV)
1.2840	2^-	1	1	170	280
1.5690	1^+	0	1	2000	86.0
1.7630	1^-	1	1	650	39.0
1.8980	1^-	1	1	1000	34.0
1.9330	1^-	1	0	5000	150
3.0325	3^+	2	1	400	4.57
3.1258	2^+	2	0	500	4.88
3.2520	3^-	3	1	2000	160

Table 5.4

The $^{25}Mg(p,p_2)^{25}Mg$ Resonance Parameters For E_p = 0.7 - 3.4 MeV

E_p (MeV)	J^π	l	s	Γ_{p_2} (eV)	$\gamma_{p_2}^2$ (keV)
1.8990	3^-	1	2	300	84.0
2.6780	3^+	2	1	3000	197
2.7145	3^+	2	1	1000	58.7
2.7280	4^-	3	1	100	89.4
2.7760	2^-	1	2	1000	7.02
		3	2	1000	758
2.7990	1^+	0	1	2000	5.06
2.8400	2^-	1	1	6000	36.7
2.8560	1^+	0	1	1000	2.29
2.8870	3^+	2	2	15000	547
3.0325	3^+	2	2	400	10.2
3.0705	2^+	2	2	500	11.8
3.1393	2^-	3	2	7000[a]	1805

Table 5.4 (Continued)

E_p (MeV)	J^π	l	s	Γ_{p_2} (eV)	$\gamma_{p_2}^2$ (keV)
3.1660	4^-	3	2	-1000[a]	241
3.2520	3^-	1	2	2000	5.93
3.2690	3^+	2	1	4000	62.2
3.3140	1^+	2	1	4000	57

[a]From interference effects the relative sign of $|\Gamma|^{1/2}$ was determined to be negative for these two resonances.

CHAPTER VI

ANALYSIS OF RESULTS

A. Comparison With Previous Results

Recent interest in the nucleus ^{26}Al has involved detailed studies of the stretched states with $J^{\pi} = 5^-$ and 6^-. One motivation of the present investigation was to confirm information obtained about these stretched states via other reactions, and to use the high energy resolution system to search for fragmentation of the stretched states. One resonance which had been reported in the literature (Endt *et al.*, 1986; Peterson *et al.*, 1988) as a stretched state should have been observed in the previous study (Adams, 1983) of E_p = 0.7 - 2.0 MeV. The data in this region were reanalyzed in order to search for the reported stretched state, and a state of spin and parity 6^- was found at the energy 1.273 MeV. Figure 6.1 shows the proton elastic scattering data for the region E_p = 1.21 to 1.33 MeV at θ_{lab}=165°. The bottom portion of the figure shows the previous fit, without the 6^- state, and the top portion of the figure shows the fit with the current resonance parameters for that region. Figure 6.2 shows this same resonance with several different calculated fits corresponding to different spins, parities, and widths superimposed. It is obvious that there is some ambiguity in the value of the spin and width, but the best fit is achieved with $J^{\pi} = 6^-$.

The discovery of a resonance in these data that had not been reported in the previous study by Adams motivated a comprehensive reanalysis of these data. The current analysis searched for more resonances that may have gone unnoticed in the first

Figure 6.1 Differential cross sections for the $^{25}Mg(p,p_0)^{25}Mg$ reaction at $\theta_{lab} = 165°$ from $E_p = 1.21$ to 1.33 MeV. The lower half of the figure shows the data with the previous fit (Adams, 1983), while the upper half of the figure shows the data with the current fit, which includes a $J^{\pi} = 6^-$ state at $E_p = 1.273$ MeV.

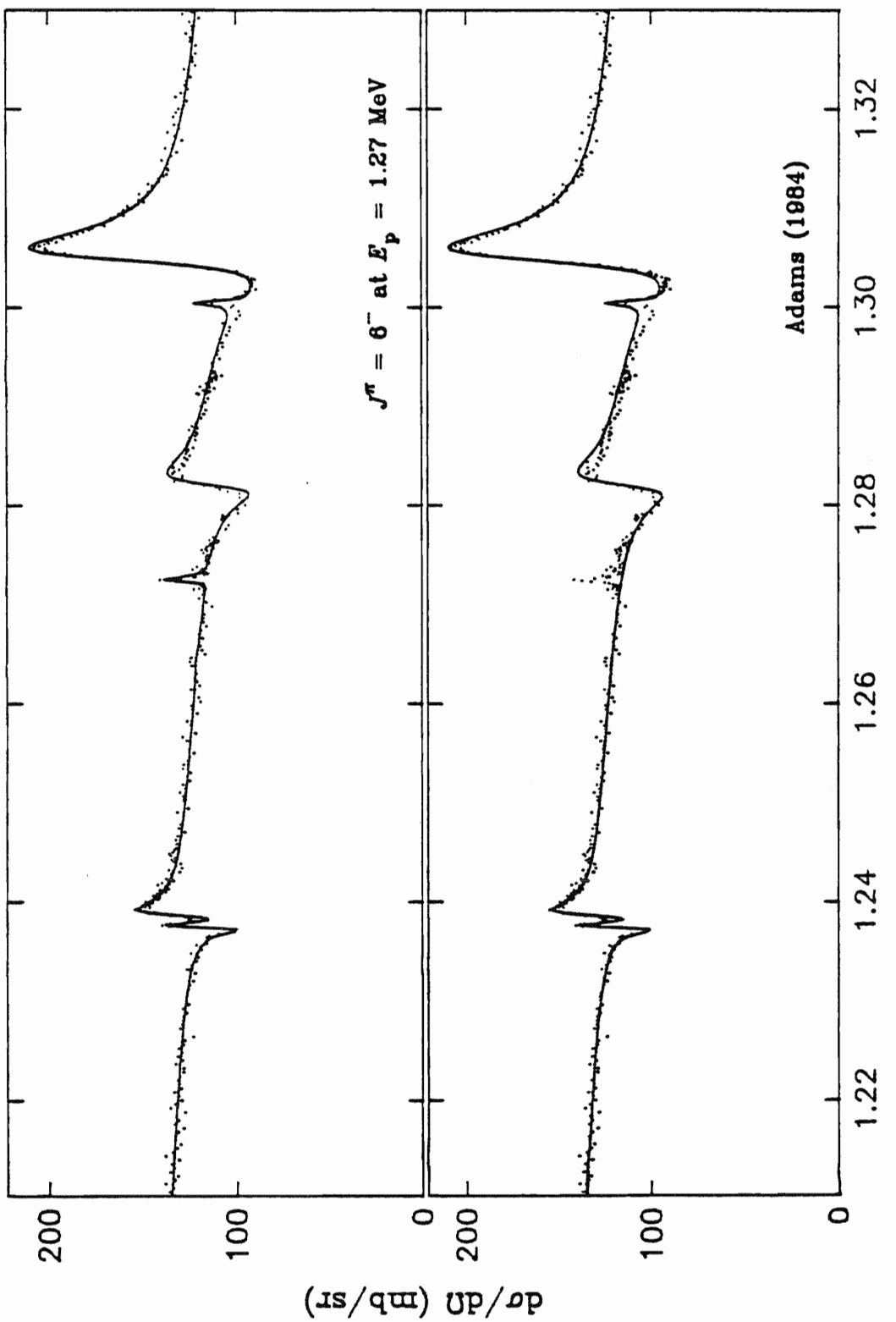
$J^\pi = 6^-$ at E_p = 1.27 MeV
Adams (1984)
200
100
0
1.22
1.24
1.26
1.28
1.30
1.32
E_p (MeV)
$d\sigma/d\Omega$ (mb/sr)

Figure 6.2 A comparison of fits with varying spins and widths for the state at E_p = 1.273 MeV. The solid line corresponds to $J^\pi = 6^-$ and Γ_p = 15 eV, the dot-dashed line corresponds to $J^\pi = 5^-$ and Γ_p = 15 eV, the dashed line corresponds to $J^\pi = 6^-$ and Γ_p = 18 eV, and the dotted line corresponds to $J^\pi = 6^-$ and Γ_p = 12 eV.

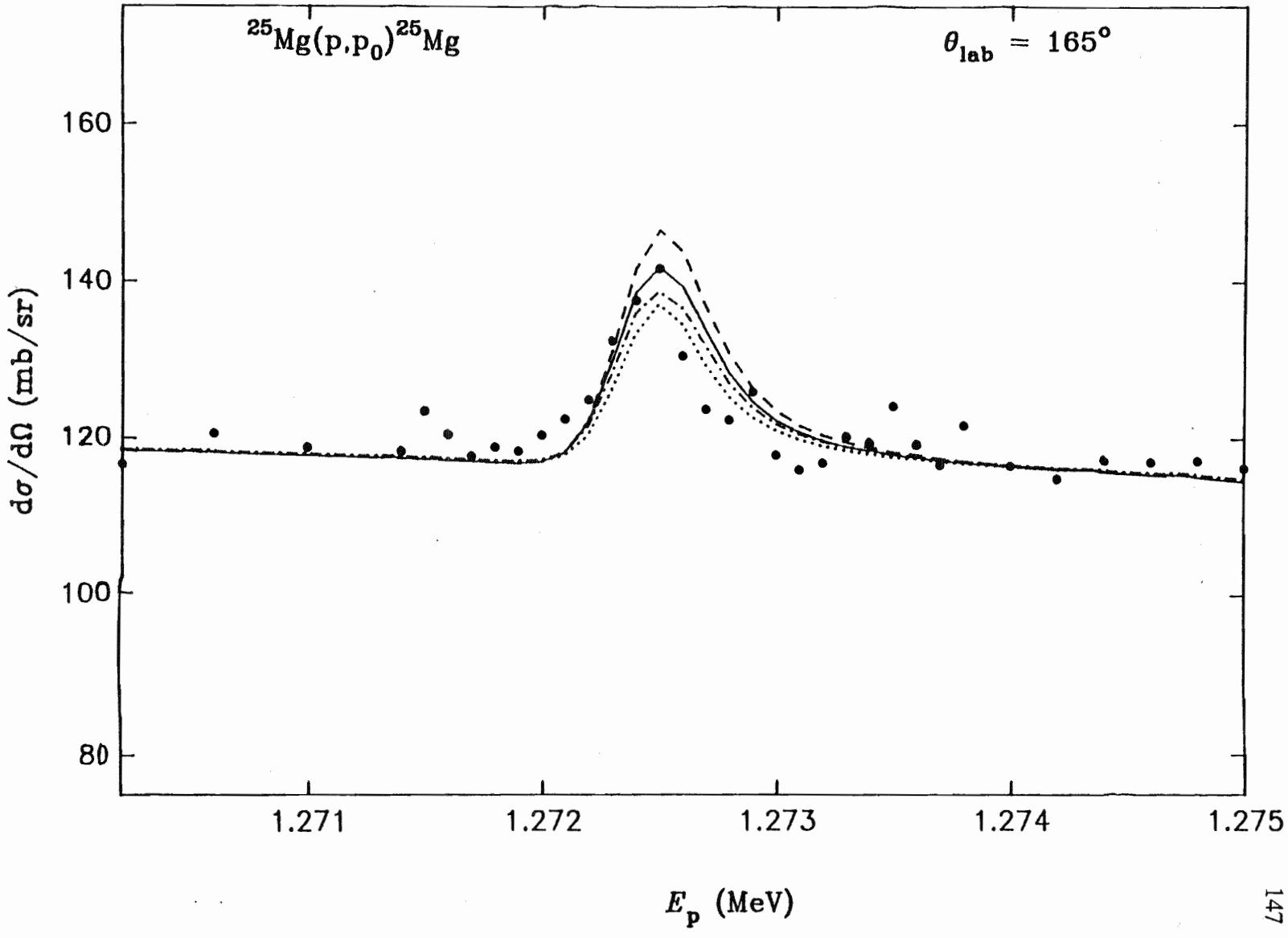
$^{25}Mg(p,p_0)^{25}Mg$
$\theta_{lab} = 165°$
160
140
120
100
80
dσ/dΩ (mb/sr)
1.271
1.272
1.273
1.274
1.275
E_p (MeV)

analysis. In addition, for many resonances Adams was unable to establish a unique J^{π} assignment. For these resonances, several possible spin assignments were reported, along with an estimated reduced width. In such cases, the current study adopted the spin and parity reported by Endt *et al.* and an appropriate value for the reduced width was determined.

In the energy region E_p = 0.7 - 2.0 MeV, 48 resonances were observed. Of these, the parameters for 7 resonances were altered from those previously reported by Adams (1983). In addition, 2 new resonances were found. In particular, the assignment of $J^{\pi} = 6^-$ to the resonance at 1.273 MeV verified the stretched state found by Peterson *et al.* (1988). Table 6.1 compares the present resonance parameters in the region E_p = 0.7 - 2.0 MeV with previous assignments.

In the energy region E_p = 2.0 - 3.4 MeV, 64 resonances were observed. Almost none of these resonances had been reported in the literature. A comparison of the results of the present experiment to previous studies will follow in the next section.

This experiment sought to confirm the presence of a $J^{\pi} = 6^-$ state at approximately E_p = 3.08 MeV. Figure 6.3 shows the data and fit obtained in the current experiment for the region E_p = 3.05 - 3.15 MeV at θ_{lab}= 90° and 165°. A resonance with $J^{\pi} = 6^-$ was observed at E_p = 3.083 MeV, along with a smaller $J^{\pi} = 4^+$ resonance at E_p = 3.099 MeV. A large resonance was also found at a slightly lower energy than the 6^- state. The presence of this state greatly complicated the data fitting process, but the best fit was found to be with the assignment of $J^{\pi} = 2^+$ at E_p = 3.071 MeV.

Table 6.1

Comparison of Present Resonance Parameters with

Previous Results for E_p = 0.7 - 2.0 MeV

	Adams (1983)			Current Analysis			Endt (1986)	
E_p (MeV)	J^π	l	Γ_p (eV)	J^π	l	Γ_p (eV)	$J^\pi;T$	$S(p,\gamma)$ (eV)
1.273				6^-	3	15	$6^-;0$	0.104
1.339	$(0\text{-}5)^+$	2	10	4^+	2	10	$4^+(3^+);0$	1.03
1.484				$2^-(1^-)$	1	65		
1.580	$4(3)^-$	1	930	4^-	1,3	855	$4^-;0$	1.13
1.588	3^+	2	160	4^+	2	50	$4^+;0$	8.210
1.774	$5(3,4)^-$	3	140	5^-	3	80	$5^-;1$	2.48
1.833	$(5,6)^-$	3	200	5^-	3	125	$5^-;1$	2.37

Figure 6.3 Differential cross sections for the $^{25}Mg(p,p_0)^{25}Mg$ reaction at $\theta_{lab} = 165°$ and $90°$ from $E_p = 3.05$ to 3.15 MeV. The solid curve is an *R*-matrix fit. The tall resonance at 3.083 MeV is the stretched state with spin and parity 6^-. The bump to the left of the 6^- state is an underlying state with positive parity, probably $J^\pi = 2^+$, which greatly complicates the data fitting process for this region.

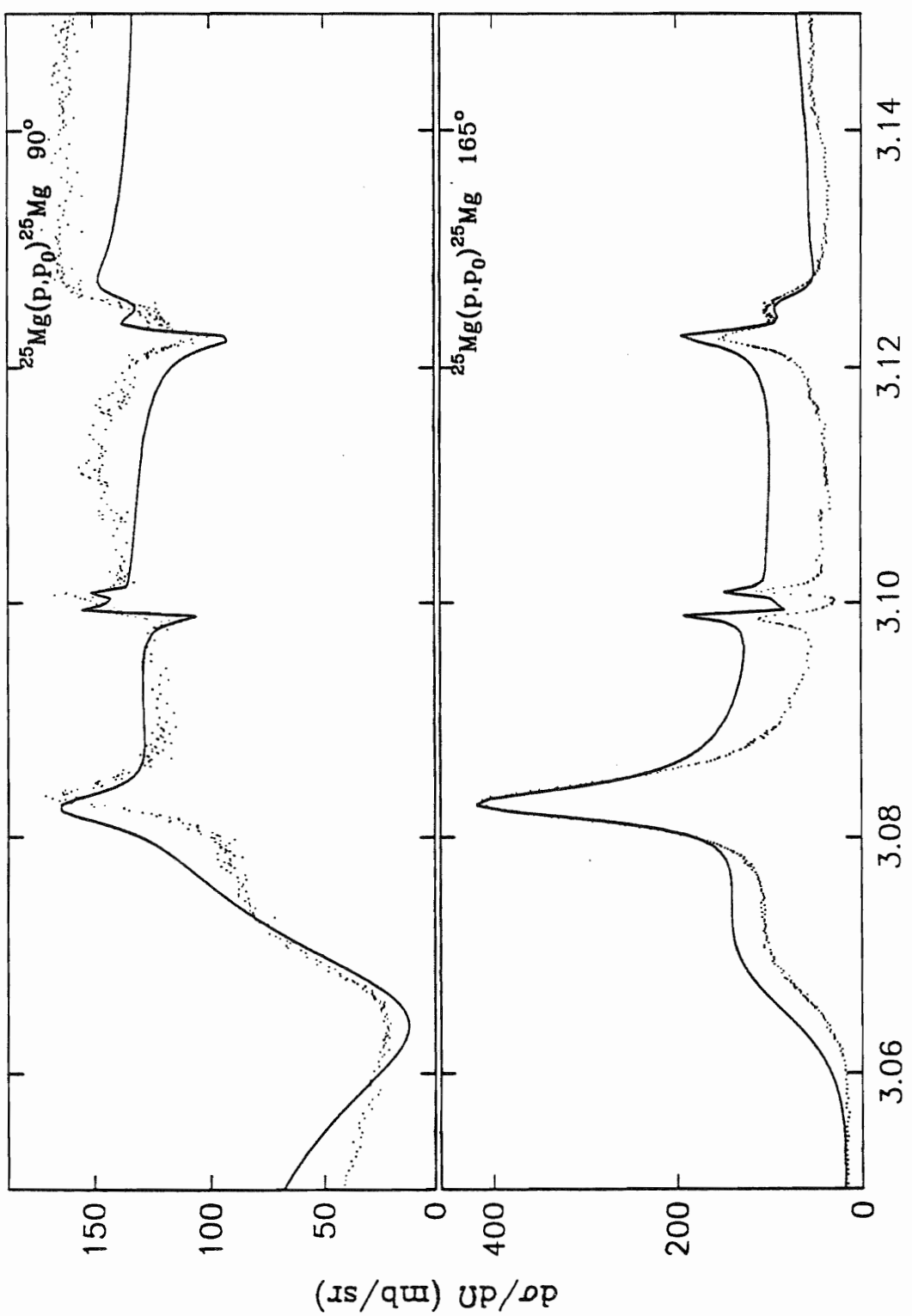
^{25}Mg(p,p$_0$)^{25}Mg 90°
^{25}Mg(p,p$_0$)^{25}Mg 165°
dσ/dΩ (mb/sr)
E_p (MeV)
150
100
50
0
400
200
0
3.06
3.08
3.10
3.12
3.14

A. Spectroscopic Factors

The probability of a nucleus in an excited state decaying via a particular exit channel is dependent on both the strength of the given channel in the intermediate state and the Coulomb-angular momentum barrier penetrability. In order to compare the relative widths ("strengths") of excited states at different excitation energies, or of states formed via different reactions, the kinematic effects inherent in the partial widths Γ_c of equation 2.3 ("laboratory widths") must be removed. The reduced width is therefore defined as a function of the laboratory width:

$$\gamma^2_{\alpha sl} = \frac{\Gamma_{\alpha sl}}{2P_l(E)} \tag{6.1}$$

where $P_l(E)$ is the Coulomb penetrability given in equation 2.34 and contains the kinematic effects due to the centrifugal term and the Coulomb term in the nuclear potential.

It is conventional (Bilpuch *et al.*, 1976) to define the single-particle reduced width as:

$$\gamma^2_{\text{sp}} = \frac{\hbar^2}{2m_c a_c^2} \tag{6.1}$$

where $m_c = m$ for a single nucleon incident on a target nucleus, and a_c is the radius of the given channel. For the present projectile and target nucleus the value for the single particle reduced width is 860 keV. The spectroscopic factor is therefore defined as:

$$S_\alpha = \frac{\gamma^2_\alpha}{\gamma^2_{\text{sp}}} \quad . \tag{6.3}$$

Table 6.2 compares the spectroscopic factors of the high spin states found in the current study with spectroscopic factors of states with the same spin and parity

Table 6.2

Comparison of Spectroscopic Factors for Stretched States in the Region $E_p = 0.7$ - 3.4 MeV

Current Experiment				Previous Results			
E_p (MeV)	E_x (MeV)	$J^\pi;T$ [a]	S(p,p)	E_x [b] (MeV)	$S(^3He,d)$[b]	$S(\alpha,t)$[c]	S_{calc} [b]
1.27	7.53	$6^-;0$	0.10	7.52	0.11	0.15	0.10
1.77	8.01	$5^-;(0)$	0.07	8.01	0.10	0.14	
1.83	8.07	$5^-;(1)$	0.09	8.06	0.18	0.19	0.12
2.03	8.26	6^-	0.03				
3.08	9.27	$6^-;1$	0.13	9.26	0.17	0.20	0.21

[a]The spins and parities are from the present experiment and the isospin values are from R. J. Peterson *et al.*, Phys. Rev. C38, 1130 (1988).

[b]R. J. Peterson *et al.*, Phys. Rev. C38, 1130 (1988).

[c]R. J. Peterson *et al.*, Phys. Rev. C33, 31 (1986).

reported in the literature. The excitation energies listed under the header "Current Experiment" are calculated from the laboratory energies of the incident proton beam in the present experiment. The three columns of spectroscopic factors under the header "Previous Results" were reported by Peterson *et al.* (1986, 1988). The first two of these columns lists spectroscopic factors for the $^{25}Mg(^{3}He,d)^{26}Al$ reaction and the $^{25}Mg(\alpha,t)^{26}Al$ reaction. These spectroscopic factors were extracted from proton stripping cross sections using distorted-wave Born approximation (DWBA) reaction models. The last column of Table 6.2 lists deformed shell model or Nilsson calculations for an empty $f_{7/2}$ shell.

C. Resonance Strengths

In interpreting resonance strength data, it is necessary to remove the kinematic effects due to Coulomb and centrifugal forces. It is useful to consider reduced widths (equation 2.42) of sequences of resonances of the same spin and parity. In figures 6.4 through 6.6, the reduced widths for the elastically scattered protons, the cumulative reduced widths, and the number of resonances for a given spin and parity are displayed as a function of proton energy. Since the channel spin assignments were often ambiguous, each plot includes resonances of both channel spins. Each figure contains information on one "level sequence" of the same spin, parity, and orbital angular momentum. The reduced width plots display the magnitudes of the individual widths most clearly, so that large single or slightly fragmented states are easily seen. Highly fragmented states, as well as large individual states, are apparent in the width sum plots. The resonance position plots most clearly show level density trends since the small states are not obscured.

Figure 6.4 Proton reduced widths versus energy for $J^{\pi} = 2^{-}$ p-wave resonances, 2^{+} s-wave resonances, and 2^{+} d-wave resonances.

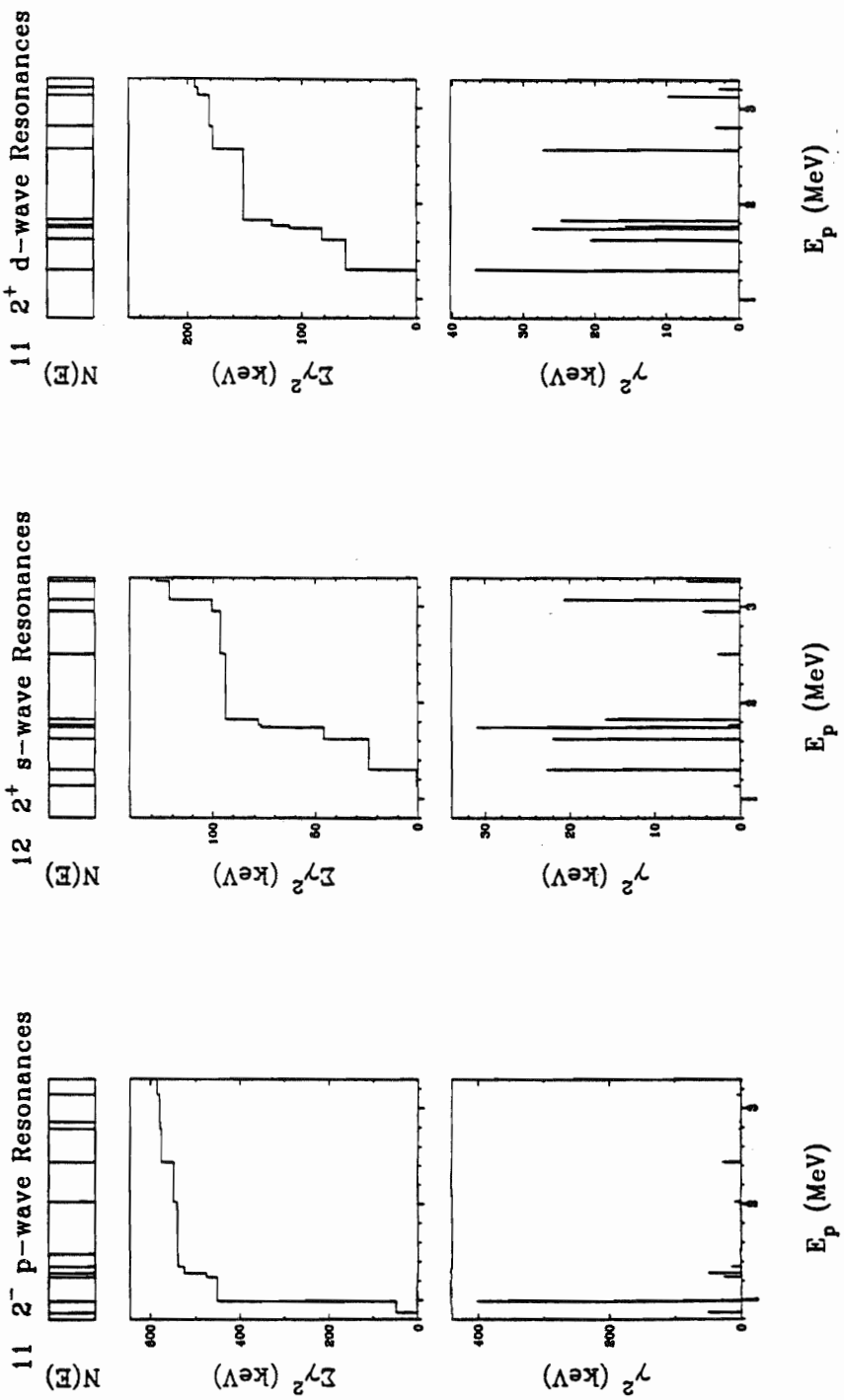
11 2⁻ p-wave Resonances
12 2⁺ s-wave Resonances
11 2⁺ d-wave Resonances
N(E)
Σγ² (keV)
γ² (keV)
E_p (MeV)

Figure 6.5 Proton reduced widths versus energy for $J^{\pi} = 3^{-}$ p-wave resonances, 3^{+} s-wave resonances, and 3^{+} d-wave resonances.

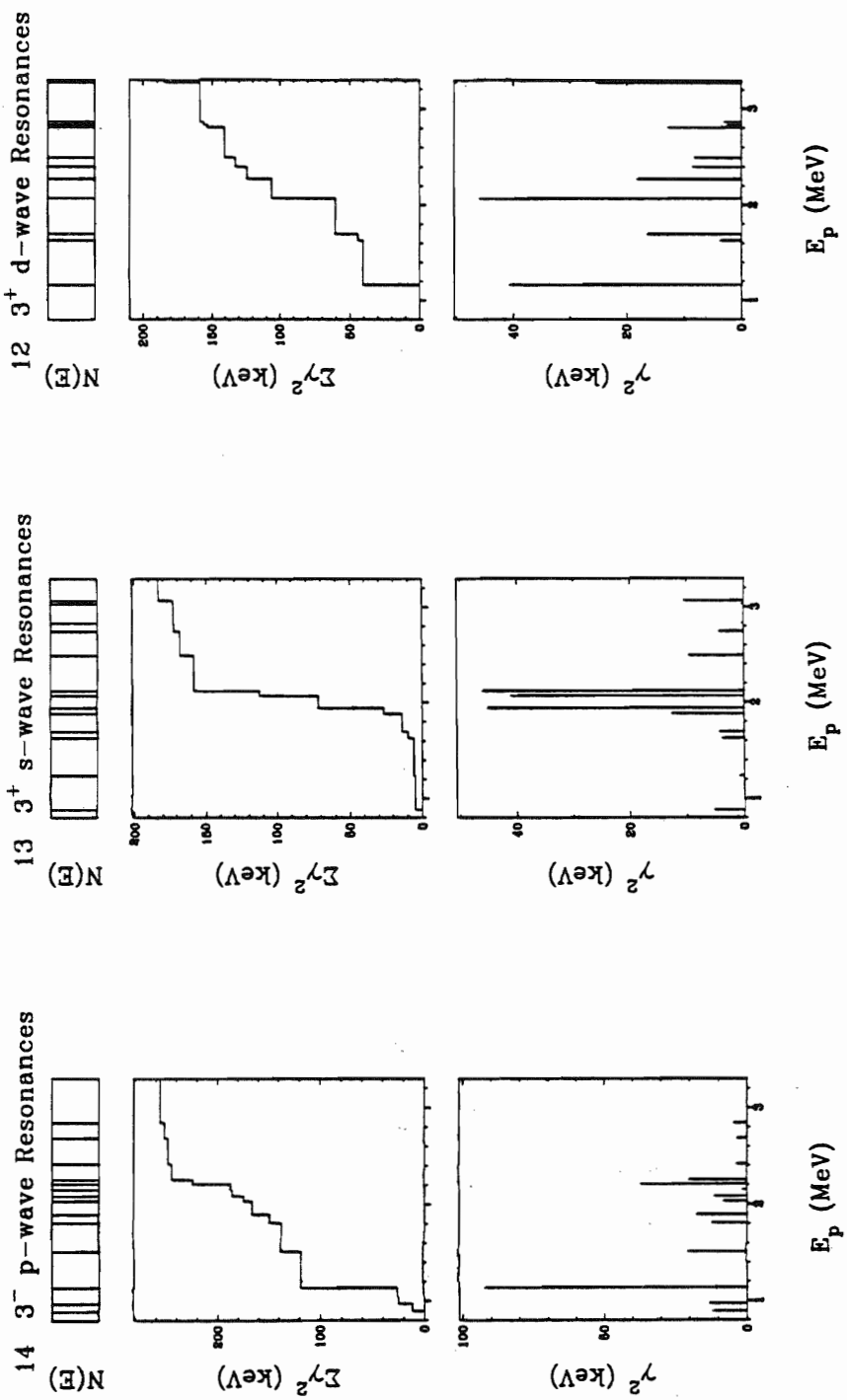
12 3+ d-wave Resonances
13 3+ s-wave Resonances
14 3- p-wave Resonances
N(E)
Σγ² (keV)
γ² (keV)
Ep (MeV)

Figure 6.6 Proton reduced widths versus energy for $J^{\pi} = 4^{-}$ p-wave resonances, 4^{+} d-wave resonances, and 6^{-} f-wave resonances.

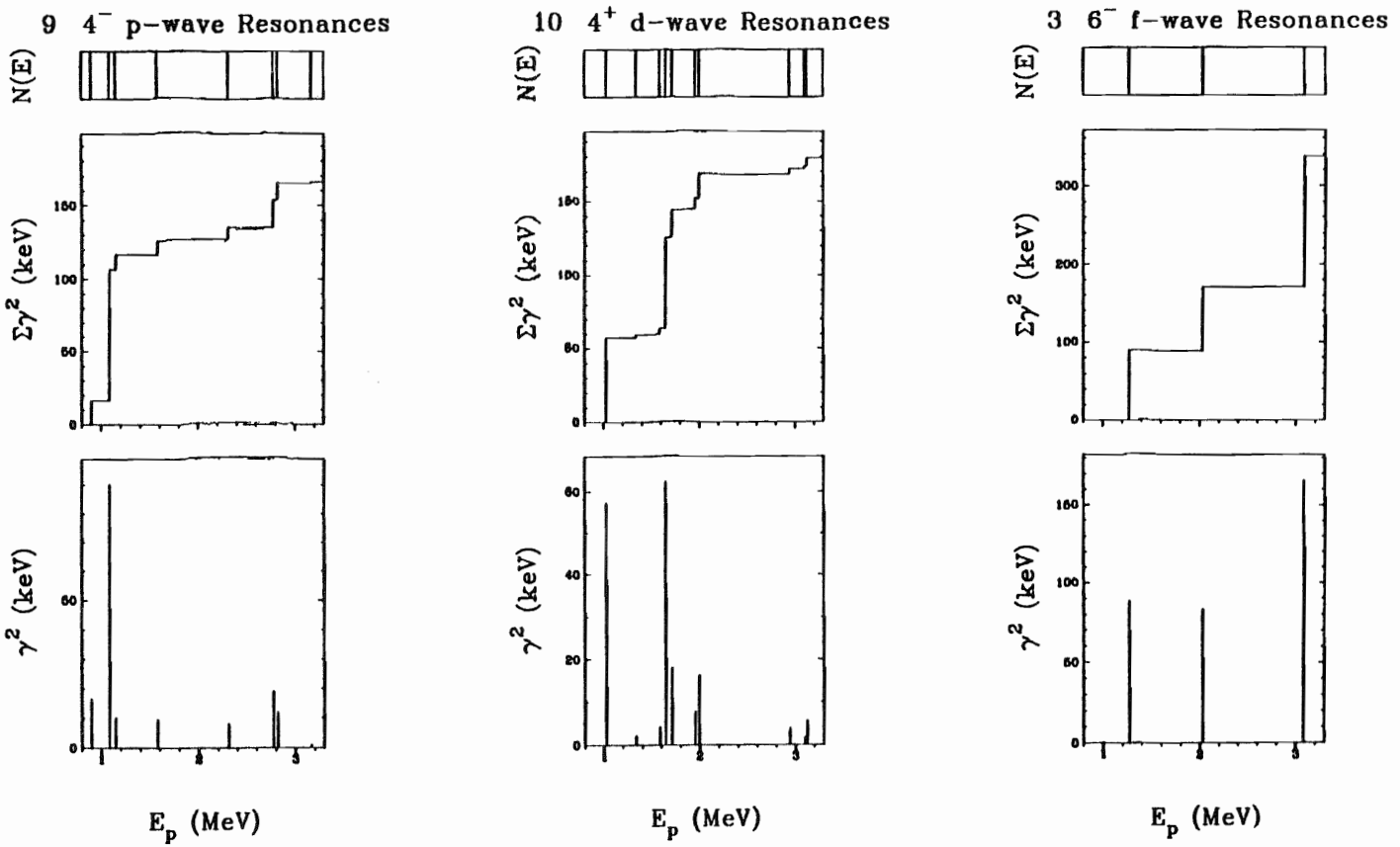
9 4⁻ p-wave Resonances
10 4⁺ d-wave Resonances
3 6⁻ f-wave Resonances
N(E)
Σγ² (keV)
γ² (keV)
E_p (MeV)

The strengths of highly excited levels of nuclei follow statistical distributions. The Porter-Thomas distribution (Porter *et al.*, 1956), a chi-squared distribution with one degree of freedom, describes the distribution of reduced widths for a single channel:

$$P(y) = \frac{1}{\sqrt{2\pi y}} \exp\left(-\frac{y}{2}\right), \qquad y = \frac{\gamma^2}{\langle \gamma^2 \rangle}. \tag{6.3}$$

If the amplitude distribution is Gaussian, then the distribution for the (normalized) γ^2 is a Porter-Thomas distribution. The Gaussian assumption is a cornerstone of random matrix theory, which is now thought to describe complex nuclear systems.

Because of the large number of open channels in this experiment, most of the level sequences contain a small number of resonances. In figures 6.7 through 6.9, sequences which contained a statistically significant number of levels were compared to the Porter-Thomas distribution. In spite of the small number of resonances comprising a given sequence, the data follow the Porter-Thomas prediction rather well. This leads to the conclusion that few levels were missed in the present analysis.

D. Conclusions

Resonance parameters were extracted for proton scattering in the energy range from E_p = 0.7 to 3.4 MeV. A comparison of level sequences for the reaction $^{25}Mg(p,p_0)^{25}Mg$ with the Porter-Thomas distribution produced good agreement, indicating that the sequences are fairly complete. Two new resonances were found in the data obtained previously (E_p = 0.7 to 2.0 MeV). A total of 64 resonances were found in the region E_p = 2.0 - 3.4 MeV.

Figure 6.7 Porter-Thomas distributions for $J^{\pi} = 1^-$ p-wave resonances, 1^+ d-wave resonances, and 2^- p-wave resonances.

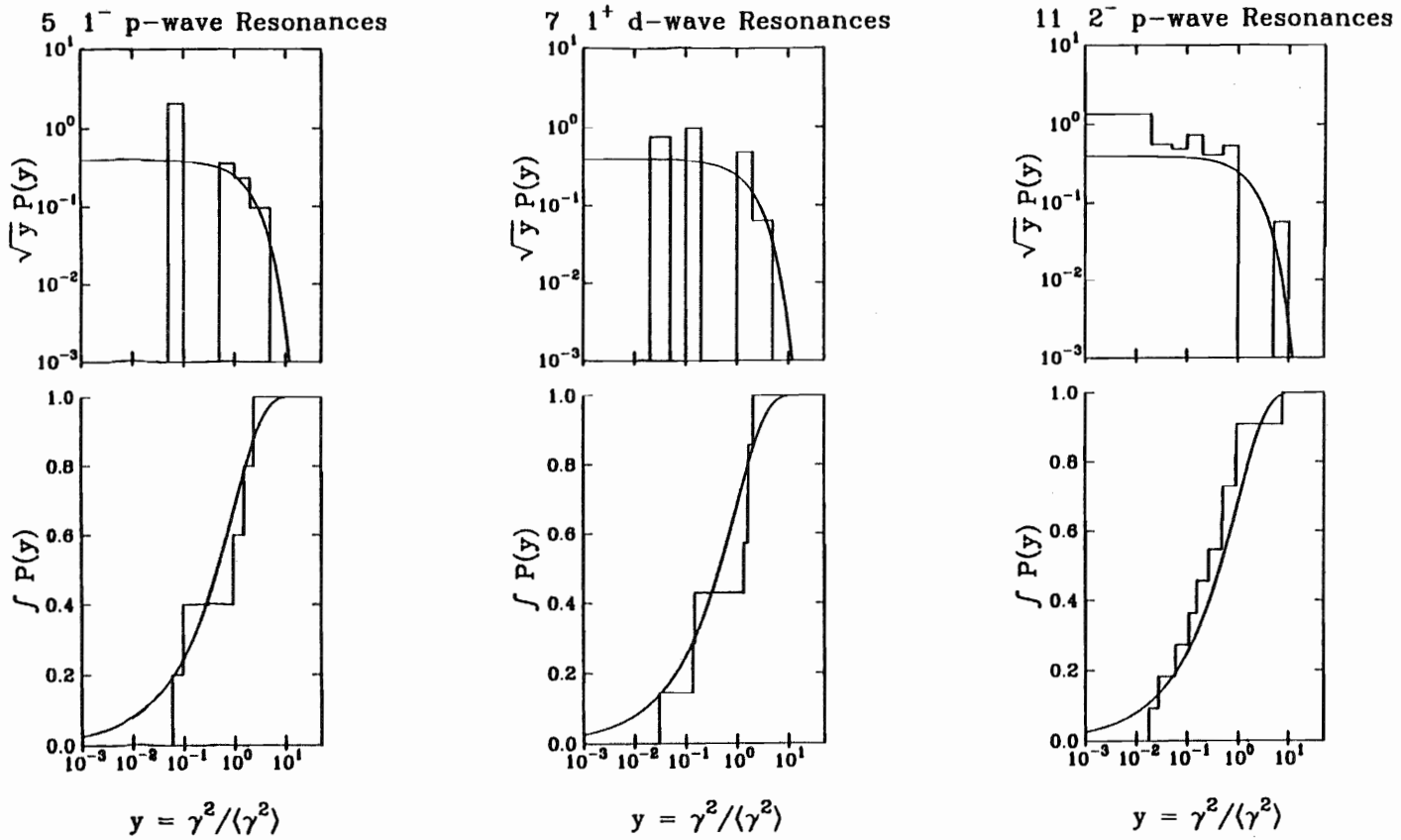
5 1⁻ p-wave Resonances
7 1⁺ d-wave Resonances
11 2⁻ p-wave Resonances
√y P(y)
∫ P(y)
y = γ²/⟨γ²⟩

Figure 6.8 Porter-Thomas distributions for $J^{\pi} = 2^{+}$ s-wave resonances, 3^{-} p-wave resonances, and 3^{+} s-wave resonances.

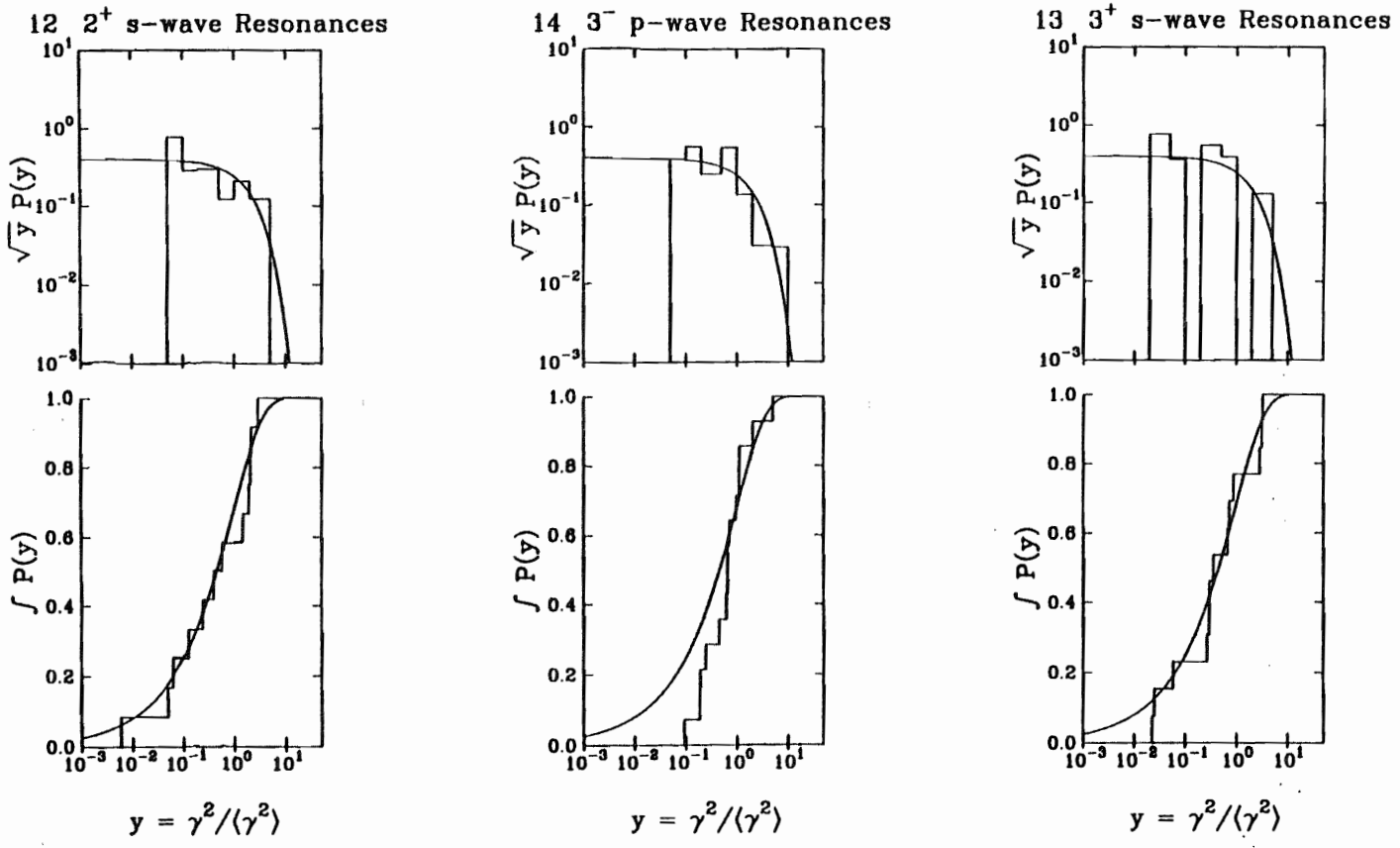
12 2+ s-wave Resonances
14 3- p-wave Resonances
13 3+ s-wave Resonances
√y P(y)
∫ P(y)
y = γ²/⟨γ²⟩

Figure 6.9 Porter-Thomas distributions for $J^{\pi} = 3^{+}$ d-wave resonances, 4^{-} p-wave resonances, and 4^{+} d-wave resonances.

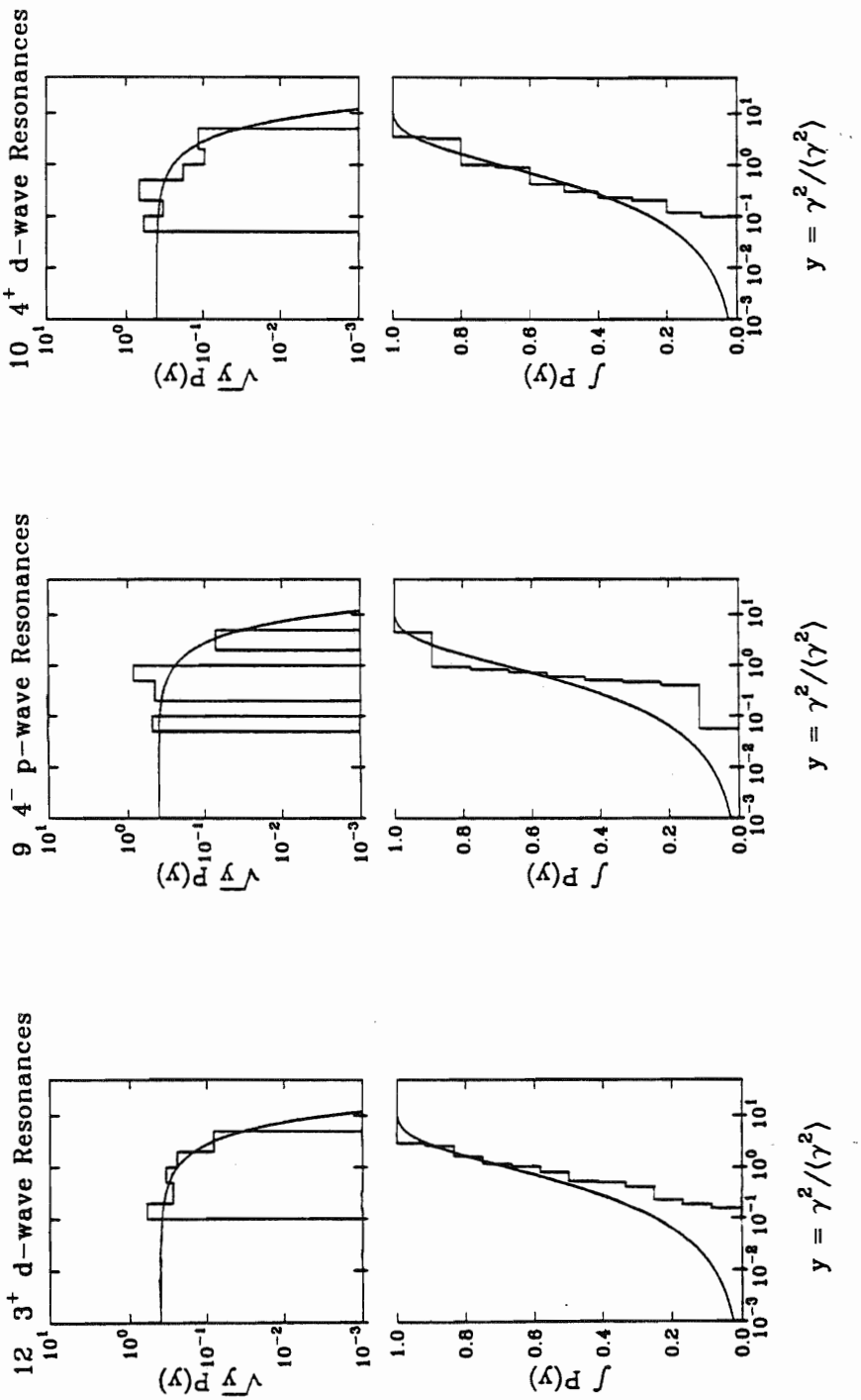
10 4+ d-wave Resonances
9 4− p-wave Resonances
12 3+ d-wave Resonances
√y P(y)
∫ P(y)
y = γ²/⟨γ²⟩

The existence of four stretched states were confirmed, and spectroscopic factors were extracted using a model-independent *R*-matrix code. In addition, another possible stretched state was found at E_p = 2.03 MeV. The present spectroscopic factors agree qualitatively with the values obtained by Peterson *et al.* using a DWBA analysis of proton stripping reaction data. With the possible exception of one weak l = 3 state which may have $J^\pi = 6^-$, there is no evidence of additional fragmentation of the 6^- stretched state. It would be very interesting to examine this question of fragmentation for the 6^- stretched states which lie a few MeV higher in ^{26}Al, where the level density is much greater.

CHAPTER VII

SUMMARY

Excitation functions for proton elastic and inelastic scattering on ^{25}Mg were measured with the KN Van de Graaff accelerator and associated high resolution system at Triangle Universities Nuclear Laboratory. Differential cross sections for ^{25}Mg(p,p_0) through (p,p_3) were obtained for the energy range of E_p = 1.94 to 3.43 MeV. The data were measured at laboratory angles θ = 90°, 108°, 135°, 150°, and 165°, with an overall energy resolution of ~400 eV.

Resonance spins, parities, partial widths, and channel spin and orbital angular momentum mixing ratios were extracted with a multilevel, multichannel *R*-matrix based computer program. Resonance parameters were extracted for approximately 64 levels between the excitation energies of 8.23 MeV and 9.61 MeV in the compound nucleus ^{26}Al. The data were found to follow a Porter-Thomas distribution for level sequences with a statistically significant number of resonances, indicating a low number of missed levels.

The present results complement our earlier data on states in the compound nucleus ^{26}Al at excitation energies from 6.98 to 8.23 MeV. These previous data were reanalyzed, and several resonance parameter assignments were changed. Two resonances were found which previously had been unobserved. A weak 6^- stretched state was identified at E_p = 1.27 MeV, in agreement with with a 6^- T = 0 state observed in proton transfer reactions.

The primary motivation for this measurement was to study the proposed l = 3,

$J^{\pi} = 6^{-}$ stretched state at $E_x = 9.26$ MeV and to determine whether this state is fragmented. The present results confirm the existence of a 6^{-} state at $E_p = 3.08$ MeV ($E_x = 9.27$ MeV). There is no evidence for additional fragmentation of this stretched state.

The existence of four stretched states were confirmed, and spectroscopic factors were extracted using a model-independent R-matrix code. The present spectroscopic factors agree qualitatively with the values obtained from the proton transfer reactions. Another resonance at $E_p = 2.03$ MeV was tentatively assigned a spin and parity of 6^{-}.

BIBLIOGRAPHY

Adams, G., "Proton Resonance Spectroscopy in ^{26}Al." M.S. thesis, North Carolina State University, 1983.

Bethe, H. A., Rev. Mod. Phys. 9, 69 (1937).

Biedenharn, L. C. and Rose, M. E., Rev. Mod. Phys. 25, 729 (1953).

Bilpuch, E. G., Lane, A. M., Mitchell, G. E., and Moses, J. D., Phys. Reports 28C, 147 (1976).

Blatt, J. M. and Biedenharn, L. C., Rev. Mod. Phys. 24, 258 (1952).

Bohr, N., Nature (London) 137, 344 (1936).

Boyd, M. A., Gould, C. R., and Roberson, N. R., XSYS Reference Manual 4th ed. (Triangle Universities Nuclear Laboratory Technical Report, 1984).

Bull, J. S., "Entrance Channel Correlations in ^{40}Ca." Ph.D. dissertation, Duke University, 1989.

Clausen, B. L., Peterson, R. J., and Lindgren, R. A., Phys. Rev. C38, 589 (1988).

Clausen, B. L., Peterson, R. J., and Lindgren, R. A., *to be published* (1990).

Condon, E. U. and Shortley, G. H. The Theory of Atomic Spectra. Cambridge: Cambridge University Press, 1951.

Endt, P. M., de Wit, P., and Alderliesten, C., Nucl. Phys. A459, 61 (1986).

Endt, P. M., de Wit, P., and Alderliesten, C., Nucl. Phys. A476, 333 (1988).

Endt, P. M., de Wit, P., Alderliesten, C., and Wildenthal, B. H., Nucl. Phys. A487, 221 (1988).

Ferguson, A. J., Angular Correlation Methods in Gamma-Ray Spectroscopy. Amsterdam: North Holland, 1965.

Fernbach, S., Serber, R. and Taylor, T. B., Phys. Rev. 75, 1352 (1949).

Feshbach, H., Porter, C. E. and Weisskopf, V. F., Phys. Rev. 96, 448 (1954).

Heagney, J. M., Nucl. Instrum. and Methods 102, 451 (1972).

Gould, C. R., Holzweig, L. G., King, S. E., Lau, T. C., Poore, R. V., Roberson, N. R., and Wender, S. A., IEEE Trans. Nucl. Sci. NS-28, 3708 (1981).

Jaffe, R. L., Phys. Scr., vol. 20, 235 (1979).

Keyworth, G. A., "A High Resolution Study of Isobaric Analog States in ^{41}K and ^{23}Na." Ph.D. dissertation, Duke University, 1968.

King, S. E., Lau, Y. C., and Gould, C. R., IEEE Trans. Nucl. Sci. NS-28, 3822 (1981).

Kraushaar, J. J. *et al.*, Phys. Rev. C34, 1530 (1986).

Lane, A. M. and Thomas, R. G., Rev. Mod. Phys. 30, 257 (1958).

Lebo, C. *et al.*, Phys. Rev. C38, 1099 (1988).

Lindgren, R. A. and Petrovich, F., in Spin Excitations in Nuclei, edited by F. Petrovich *et al.* (Plenum, New York, 1984), p. 323.

Lomon, E. L., AIP Conference Proceedings, no. 97, 78 (1982).

Love, W. G., Franey, M. A. and Petrovich, F., in Spin Excitations in Nuclei, edited by F. Petrovich *et al.* (Plenum, New York, 1984), p. 205.

Marion, J. B., Rev. Mod. Phys. 38, 660 (1966).

McCarthy, I. E., Introduction to Nuclear Theory, (J. Wiley and Sons, New York, 1968).

Moffa, P. J. and Walker, G. E., Nucl. Phys. A222, 140 (1974).

Nelson, R. O., Bilpuch, E. G., and Mitchell, G. E., Nucl. Instrum. and Methods A236, 128 (1985).

Parks, P. B., Newson, H. W., and Williamson, R. M., Rev. Sci. Instrum. 29, 834 (1958).

Peterson, R. J. *et al.*, Phys. Rev. C33, 31 (1986).

Peterson, R. J. *et al.*, Phys. Rev. C38, 1130 (1988).

Peterson, R. J. *et al.*, Phys. Rev. C38, 1130 (1988).

Racah, G., Phys. Rev. 84, 910 (1951).

Schiff, L. I., Quantum Mechanics (McGraw-Hill Book Company, Inc., New York, 1968).

Seibel, F. T., Roberson, N. R., Bilpuch, E. G., and Newson, H. W., Nucl. Instrum. and Methods 47, 244 (1966).

Sellin, D. L., "Excited States in ^{19}F." Ph.D. dissertation, Duke University, 1969.

Szalay, A. and Somorjai, E., Nucl. Instrum. and Methods 49, 355 (1967).

Takayanagi, S., Katsuta, M., Katori, K., Chiba, R., Nucl. Instrum. and Methods 45, 345 (1966).

Teller, E., in Spin Excitations in Nuclei, edited by F. Petrovich *et al.* (Plenum, New York, 1984), p. 1.

Thomas, G. E., Nucl. Instrum. and Methods 200, 27 (1982).

Vogt, E., Rev. Mod. Phys. 34, 723 (1962).

Warthen, B. J., "Proton Resonance Spectroscopy in ^{40}Ca." Ph.D. dissertation, Duke University, 1987.

Westerfeldt, C. R., Nelson, R. O., Bilpuch, E. G., and Mitchell, G. E., The TUNL High Resolution Laboratory System and Operating Procedures (Triangle Universities Nuclear Laboratory Technical Report, 1986).

Westerfeldt, C. R., Nelson, R. O., Bilpuch, E. G., and Mitchell, G. E., Nucl. Instrum. and Methods A270, 467 (1988).

Wigner, E. P. and Eisenbud, L., Phys. Rev. 72, 29 (1947).

BIOGRAPHY

Kara Jayne Keeter

Personal: Born August 28, 1962 Dalton, Georgia

Education:
B.S. Physics, Tennessee Technological University, 1984
M.A. Physics, Duke University, 1986

Positions:
Laboratory Instructor, Tennessee Technological University, 1982-1984
Research Assistant, Duke University, 1984
Teaching Assistant, Duke University, 1984-1985
Research Assistant, Duke University, 1985-present

Abstracts: "High Resolution Proton Spectroscopy of ^{26}Al", Kara Keeter, E. G. Bilpuch, C. R. Westerfeldt, G. E. Mitchell, Bull. Am. Phys. Soc. 33, 2194 (1988).

Memberships:
American Physical Society
Sigma Pi Sigma
Mu Phi Epsilon